Development of an in-situ effective electron lifetime measurement device

Mateusz Poplawski

INSTITUT POLYTECHNIQUE DE PARIS

NNT : 2023IPPAX097

Thèse de doctorat

Development of an *in-situ* effective electron lifetime measurement device

Thése de doctorat de l'Institut Polytechnique de Paris
préparée à l'Ecole Polytechnique

École doctorale n°626 Polytechnique de Paris (ED IP Paris)
Spécialité du doctorat : Physique

Thèse présentée et soutenue à Palaiseau, le 17 Novembre 2023, par

Mateusz Poplawski

Composition du Jury

Philip Schulz Research Director IPVF/CNRS	Président
Adriana Creatore Full Professor, Plasma and Materials Processing - TUe	Rapporteuse
Martin Schubert Head of Department Quality Assurance, Characterization and Simulation, Fraunhofer ISE	Rapporteur
Christophe de la Taille Directeur laboratoire PCC, Ecole Polytechnique - CNRS/IN2P3	Examinateur
Delfina Munoz Strategic project manager and senior researcher, CEA/INES	Examinatrice
Pere Roca i Cabarrocas Directeur Scientifique & Directeur de recherche, IPVF, École Polytechnique – CNRS/LPICM	Directeur de thèse
François Silva Ingénieur R&D, Diamond Foundry	Co-Directeur de thèse
Jean-Charles Vanel CNRS Engineer, École Polytechnique – CNRS/LPICM	Invité

Cette thèse présente une avancée révolutionnaire dans la technologie in-situ, portant son développement au Niveau de Préparation Technologique (TRL) 4, englobant à la fois des cadres théoriques et des innovations matérielles. Précédemment développé au TRL 2/3, ce travail marque un bond significatif, mettant en évidence des applications potentielles dans la recherche future et fournissant des solutions robustes pour une utilisation industrielle.

Chapitre 2 : Intégration du Système Optique et Rénovation du Réacteur PECVD

Un système optique novateur est conçu, intégrant des optiques laser et de collecte pour des mesures efficaces de photoluminescence (PL) et de photoluminescence modulée (MPL) dans des environnements industriels. Le système facilite l'intégration et s'adapte à différentes distances dans les lignes de processus industriels. Parallèlement, un réacteur de Dépôt Chimique en Phase Vapeur Assisté par Plasma (PECVD) est amélioré pour des opérations automatisées, améliorant le contrôle et la reproductibilité, cruciaux pour les normes industrielles.

Chapitre 3 : Avancées des Techniques de Mesure

Ce chapitre introduit deux avancées significatives : une réduction du temps de mesure MPL et une nouvelle méthode pour des mesures directes de la durée de vie effective (τeff). Un passage d'une onde stationnaire à une méthode de balayage en fréquence réduit considérablement le temps de mesure MPL de 40 secondes à 2 secondes. De plus, une technique simplifiée de mesure directe de la durée de vie est développée, marquant une amélioration substantielle par rapport aux méthodes indirectes existantes. Ces deux avancées ont conduit à des demandes de brevets, soulignant leur nature innovante.

Chapitre 4 : Application dans la Fabrication d'Oxyde d'Aluminium

Les techniques de mesure améliorées sont appliquées pour observer des phénomènes rapides dans l'oxyde d'aluminium, un matériau clé dans les architectures de cellules solaires PERC et TOPCon. Ce chapitre fournit des aperçus pour optimiser τeff dans diverses expériences au sein d'un réacteur PECVD utilisant des tranches de silicium en Oxyde d'Aluminium (ALD-AlOx). Il démontre l'efficacité du τeff in-situ pour des traitements de recuit optimaux, comparant différents profils thermiques et leur efficacité. Le chapitre explore également les implications de la diffusion de l'hydrogène lors de l'exposition à la lumière VUV et l'importance de maintenir un budget thermique constant pendant les processus plasma.

Pertinence et Impact Industriels

Cette thèse souligne la nécessité critique de combler le fossé entre le monde académique et l'industrie. En se concentrant sur des applications pratiques et une adaptabilité dans des contextes industriels, elle répond à la demande urgente de technologies pouvant être intégrées de manière transparente dans les processus industriels existants. Les avancées dans les techniques de mesure et la rénovation des réacteurs ne renforcent pas seulement les capacités de recherche, mais offrent également des avantages tangibles pour l'industrie, tels qu'une efficacité, un contrôle et une adaptabilité améliorés dans les processus de fabrication. Ceci s'aligne avec l'accent croissant mis sur la recherche et le développement dans l'industrie du design, comme souligné dans la littérature actuelle.

Conclusion

Ce travail établit une nouvelle norme dans le domaine de la technologie in-situ, prouvant que la recherche académique peut être étroitement alignée avec les besoins industriels. Les avancées réalisées dans cette thèse ne sont pas seulement significatives sur le plan académique, mais sont également prêtes à avoir un impact considérable dans le monde industriel, en particulier dans les secteurs de la conception et de la fabrication.

"Jack of all trades, master of none but often times better than a master of one."

Robert Greene, 'Groats-Worth of Wit', 1592 [1]

To everyone who has been a pillar of support throughout this journey, I extend my heartfelt thanks. Lila, your extraordinary kindness has been a beacon during this period, creating memories that will forever be cherished. Celine and Gibez, your combined warmth and camaraderie during and after confinement have made this time truly unforgettable. Your presence has been a constant source of comfort and joy. Pere, your unwavering support and guidance, even through my ups and downs, has been a cornerstone of my journey. I've always been able to rely on you to keep me grounded and offer a listening ear.

Francois, Jean-Charles, and Cyril, the depth of your expertise, the resources you've provided, and our endless, fascinating conversations have greatly enriched both my knowledge and experience. Our discussions, without boundaries, will always hold a special place in my heart. Pavel, the samples you supplied were indispensable to my work, and your suggestion to read '1984' was an enriching addition. Mark and Jonathan, having BEER next to my lab brought an enjoyable and educational aspect to my day-to-day life. Your building tips and tricks, particularly in MIG welding, and the bird and egg 3D prints, were exemplary. Roch, Isabelle, Grégory, and Florian, your willingness to share the management side of IPVF has been instrumental for my future projects. To the broader teams at LPICM, IPVF, and others who have been part of my journey, your support has been fundamental. To all my friends, the coffee breaks and shared snacks made this journey more pleasant and memorable.

Finally, a heartfelt thank you to Monoprix for being a reliable source of sustenance; I am truly grateful for your service and sacrifice.

What a lonely experience.

Institut Polytechnique de Paris
Palaiseau, France

ALD	Atomic Layer Deposition
AlOx	Aluminium Oxide
AOI	Angle Of Incidence
CPC	Compound Parabolic Concentrator
CVD	Chemical Vapor Deposition
EMF	Electromotive Force
GHGs	Green House Gases
ITRPV	The International Technology Roadmap for Photovoltaic
kHz	Kilo Hertz
LPCVD	Low Pressure Chemical Vapour Deposition
MgF2	Magnesium Fluoride
MHz	Mega Hertz
MPL	Modulated Photoluminescence
NA	Numerical Aperture
NREL	National Renewable Energy Laboratory
PCD	Photoconductance Decay
PECVD	Plasma-Enhanced Chemical Vapour Deposition
PERC	Passivated Emitter Rear Cell
PL	Photoluminescence
PLM	Programable Logic Controller
PV	Photovoltaics
PVD	Physical Vapor Deposition
RF	Radio Frequency
RTP	Rapid Thermal Processing
SiOx	Silicon Oxide
S-Q	Shockley-Queisser
SRH	Shockley-Read-Hall
SSI	Steady State Intensity
STFT	Short Term Fourier Transform
TOPCon	Tunnel Oxide Passivated Contact
TRL	Technology Readiness Level
UV	Ultravoilet
VUV	Vacuum Ultra-Violet
τ_{eff}	Effective Electron Lifetime
τ_m	Modulated Effective Electron Lifetime

1 INTRODUCTION TO SOLAR PANELS

The climate crisis, a complex and multifaceted global phenomenon, has emerged as one of the most pressing challenges of the 21st century, driven by the anthropogenic increase of greenhouse gases (GHGs) in the Earth's atmosphere. This accumulation of GHGs, leads to the enhanced greenhouse effect, causing the Earth's average temperature to rise, a process known as global warming [2], [3]. Solar energy stands at the forefront of renewable solutions that are vital in addressing the climate crisis. The sun provides an abundant, inexhaustible source of energy that can be harnessed through photovoltaic (PV) technology to generate electricity. It is an integral part of the solution to the climate crisis, but it also presents opportunities for sustainable development and energy stability (Figure 1-1) [4], [5].

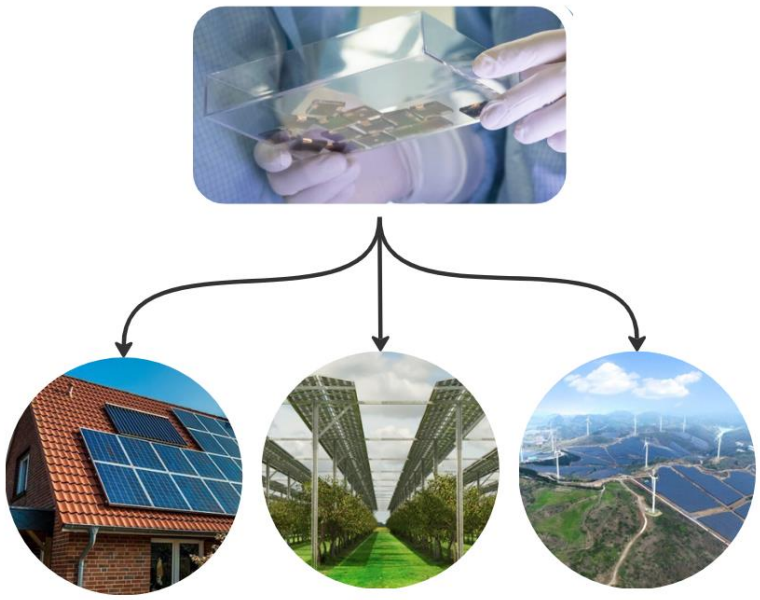

Figure 1-1: Applications interlinked with solar cell research

Solar panels are devices designed to convert sunlight into electricity. They consist of numerous solar cells made from semiconductor materials, such as silicon, to generate power. Solar panels have become increasingly popular as a renewable and clean energy source, reducing our reliance on fossil fuels and minimizing our carbon footprint [6]. Currently used in various applications, from residential rooftop installations to large-scale solar farms (Figure 1-1). They can be installed on homes, industrial roofs, and public

buildings, providing an environmentally friendly and cost-effective solution for meeting energy needs. Solar energy systems can be grid-connected or off-grid, allowing for various levels of energy independence and self-sufficiency. Advancements have improved the efficiency, durability, and aesthetics of solar panels, making them a more attractive option for consumers. They are an essential component of the global shift towards sustainable energy, helping to mitigate the effects of climate change and promote energy security.

1.1 GLOBAL ENERGY TRANSITION

During the year after Russia's invasion of Ukraine, the global energy landscape went through a dramatic transformation. Soaring energy prices significantly impacted consumers worldwide, total per capita household energy costs increased by a range of 62.6% to 112.9% at the global level highlighting the critical importance of energy security within the geopolitical context [7]. This created calls for an expedited energy transition, advocating for a shift from heavily polluting fuels supplied by a few major producers to low-carbon energy sources like renewables and nuclear power [8].

1.1.1 Energy Generation Trends

Despite the global energy crisis, world electricity demand proved resilient, increasing by nearly 2%, a slight decrease from the 2.4% average growth between 2015-2019 [9]. Many events have arisen: i) The surge in electric vehicle sales and use of heat pumps accelerated the electrification of transport and heating sectors. However, the recovery efforts from Covid-19 impacts were hindered by record-high energy prices. ii) Elevated costs of energy commodities like natural gas and coal led to increased power generation expenses, triggering rapid inflation. All this resulted in renewables and nuclear energy being projected to account for over 90% of the global growth of electricity supply in the next three years (Figure 1-2). China leads the growth in renewable generation with 45%, followed by the EU at 15%. The expansion of renewables will necessitate enhanced investments in grids and flexibility for successful integration. The rise in nuclear energy is due to recovering French nuclear plants and new facilities primarily in Asia, while global power generation from natural gas and coal is anticipated to remain

stable from 2022 to 2025 [9].

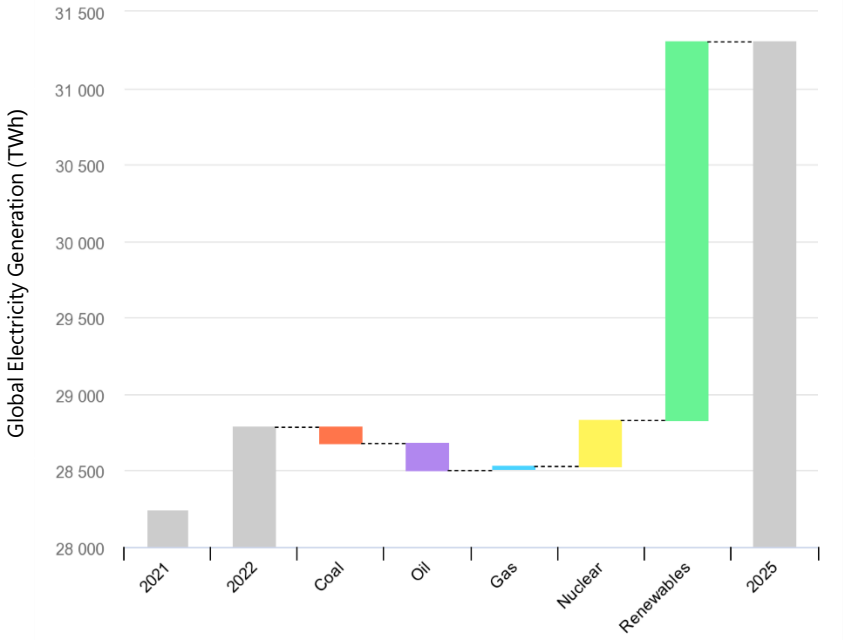

Figure 1-2: Projected 2021-2025 changes in global electricity generation [10]

Presently, only a limited number of countries generate all their electricity from renewable energy sources (Figure 1-3). Notable examples include Iceland, known for its vast geothermal power resources, which supply about 85% of its electricity, with the remainder coming from hydropower and wind power. Costa Rica generates over 98% of its electricity from renewable sources, primarily hydropower and geothermal power, complemented by wind and solar energy. Paraguay and Norway both rely heavily on hydropower for about 95% and 98% of their electricity, respectively, with additional contributions from wind and solar power. New Zealand derives about 80% of its electricity from a combination of hydropower, geothermal power, and wind power.

Other countries are making significant strides towards increasing the proportion of their electricity generated from renewable energy sources. Some have set ambitious targets to achieve 100% renewable energy generation by specific future dates, with goals ranging from 2030 to 2070 [11].

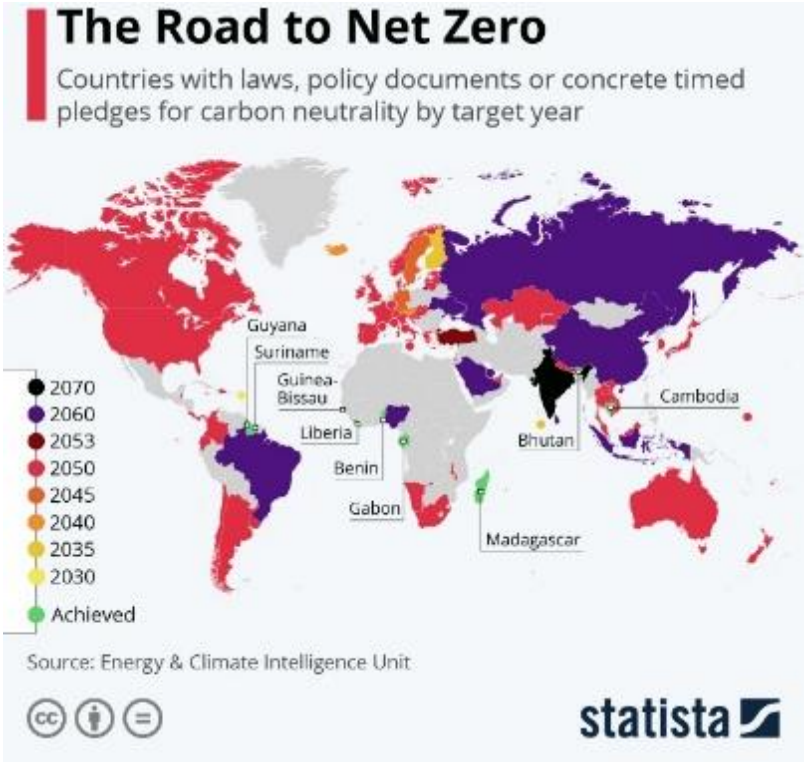

Figure 1-3: World map showing the year each country has set for achieving 100% green energy production [11]

Viewing the historical annual regional demand of electricity and the amount provided by solar (Figure 1-4) of the periods 2010, 2021, and 2050 (modelled), PV could provide a large portion of electricity demand around the world. Previous projections underestimated PV, however now the focus is based upon the maximum industry growth rates and supply chain limitations to reach the news goals [12].

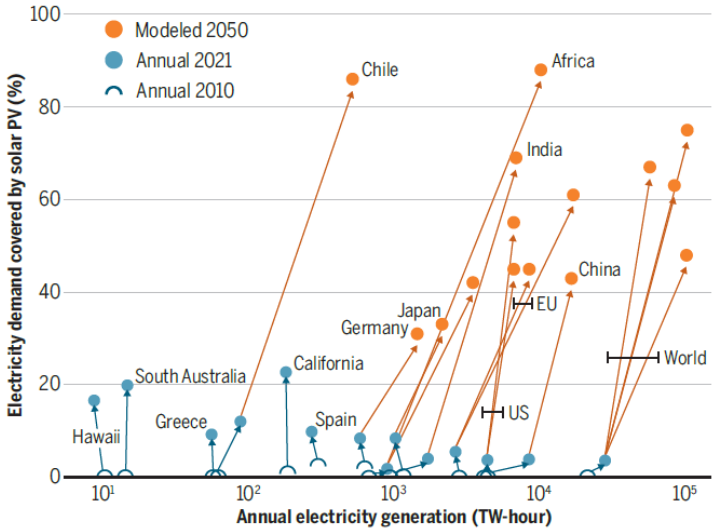

Figure 1-4: Regional electricity demand supplied by solar PV and projected demand [12]

1.2 SOLAR INTEGRATION

Looking at the latest of renewable energy integration, a few standout fields to pay attention to are residential solar, agrivoltaics, solar fields, and combined wind-solar fields. These innovative approaches show the integration of solar energy generation with residential, agricultural, and land use practices. A brief overview of their implementation sheds light on the potential for sustainable energy solutions that minimize environmental impact and promote resource efficiency, while simultaneously addressing our ever-growing energy demands.

1.2.1 Residential Solar

Solar energy for residential applications represents a promising avenue for fostering energy independence, reducing greenhouse gas emissions, and promoting sustainable housing development [13], [14]. Home-based solar systems, primarily consisting of rooftop photovoltaic (PV) installations, enable households to generate electricity from sunlight, contributing to a decentralized energy landscape. As solar panel efficiency and energy storage technologies continue to advance, residential solar adoption plays a vital role in the global transition towards a low-carbon energy future. Residential solar systems encompass grid-connected and off-grid configurations, allowing homeowners to tailor their level of energy self-sufficiency based on individual needs and grid access. Grid-connected systems enabling consumers to offset their electricity costs by feeding excess solar-generated electricity back into

the grid. Meanwhile, off-grid systems can provide essential energy services to remote or underserved communities.

1.2.2 Agrivoltaics

Agrivoltaics, which combines agricultural practices with PV, has emerged as a promising solution for addressing the dual challenges of food security and sustainable energy production [15]. By integrating solar panel installations within agricultural landscapes, agrivoltaics aims to optimize land use, minimize resource competition, and create synergies between food and energy systems. This interdisciplinary field of research encompasses the design, implementation, and evaluation of co-located solar and agricultural systems to achieve efficient, resilient, and environmentally responsible outcomes. The system capitalizes on the complementary nature of solar energy generation and agricultural processes [16].

Figure 1-5: Example of double land usage for Agrivoltaics in Amance, France [12].

The solar panels provide shade and reduce evapotranspiration, potentially leading to water savings and improved microclimatic conditions for crop growth enabling the underlying land to maintain its agricultural productivity, thus preserving valuable arable land. Furthermore, the co-location of solar and agricultural infrastructure can enhance biodiversity, reduce soil erosion, and create additional revenue streams for farmers [17].

1.2.3 Solar Farms

Solar power plants which consist of vast arrays of PV modules represent a large-scale approach to harnessing the sun's energy for electricity

generation. Their development and operation involve the systematic evaluation of factors such as geographic location, land use, and grid connectivity. Optimal site selection is essential to maximize energy yield, minimize environmental footprint, and ensure the financial viability of solar farm projects. Advanced modelling techniques, such as geographic information systems and remote sensing, are often employed in this process to assess solar irradiance, terrain characteristics, and other relevant parameters [18]. Emerging trends in solar farm development include the integration of energy storage systems to address the intermittency of solar power generation. Additionally, they are subject to various socio-economic and regulatory factors, such as public acceptance, land acquisition, permitting processes, and access to financing [19].

1.2.3.1 Solar Wind Integration

Solar power generation is primarily influenced by weather conditions, with peak production occurring during daylight hours when sunlight is abundant [20]. In contrast, wind power generation is less predictable but often demonstrates higher output during nighttime and transitional periods, such as dawn and dusk. Furthermore, seasonal variations in wind and solar resources can offset each other, with solar power typically peaking in the summer months, while wind power tends to be stronger in winter [21].

1.3 SOLAR LIMITATIONS

Panel degradation is a critical challenge in the operation and maintenance as it directly affects the long-term performance, reliability, and economic viability. Degradation occurs due to a range of factors, such as ultraviolet (UV) radiation exposure, temperature fluctuations, mechanical stress, potential-induced degradation, and moisture ingress. These factors contribute to a gradual decline in power output, which can range from 0.7% to 2% per year, depending on the panel type and environmental conditions [22].

The Shockley-Queisser (S-Q) limit is a theoretical limit to the efficiency of a single-junction silicon solar cell, which states that the maximum efficiency of a solar cell is approximately 31% for a solar cell made of silicon. [23]. The limit is based on physical limitations of only being able to convert a certain portion of the energy from the sun into electricity as the rest is lost as heat. The S-Q limit is determined by the bandgap of the semiconductor material used in the solar cell, with a narrower bandgap allowing for greater absorption of photons, but also greater loss of energy as heat.

This limit is the result of a trade-off between the absorption of photons and the resulting thermalization which energy is not converted into electrical energy. As the bandgap increases, the number of thermalized photons decreases, and the overall efficiency increases. However, this is coupled with the decrease in the number of absorbed photons leading to a decrease in efficiency. To overcome this limit, strategies are being developed to improve the efficiency of solar cells. One strategy is to use multi-junction solar cells, which consist of multiple cells of semiconductor materials stacked on top of each other. Each layer is designed to absorb a specific range of wavelengths of light, allowing for increased efficiency compared to a single-layer solar cell.

According to the National Renewable Energy Laboratory (NREL), the current highest reported efficiencies (lab grade) for silicon and perovskite solar cells are 26.8% and 26% (note that these are for different cell sizes), while the highest reported efficiency for a tandem solar cell (using perovskite and silicon) is 33.7%.

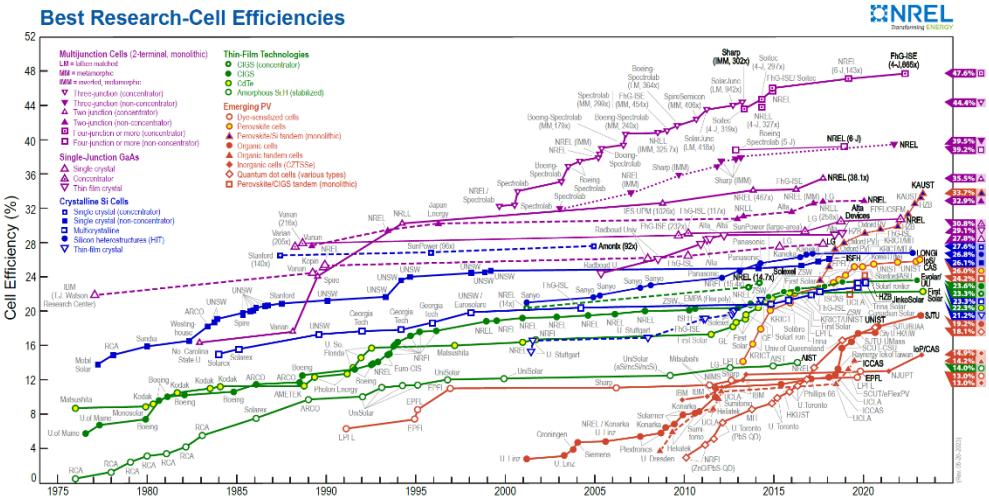

Figure 1-6: NREL Best Research-Cell Efficiency Chart showing the progress of solar cell efficiency over time for various types of solar cells. The chart illustrates the maximum efficiency achieved for each technology [24].

There is currently no set date for when these technologies will be widely available on the market, only projections. Perovskite solar cells have shown great promise but are still in the initial stages of development and commercialization, and there is ongoing research to improve their efficiency and stability. Some companies (GCL, Utmolight) have announced plans to start production of perovskite solar cells, but it is still uncertain when they will be widely available, potentially end of 2023. However, it is also in pilot stages of development and is not yet widely adopted yet due to stability

issues.

1.4 PHOTOVOLTAICS ROADMAP

The efficiency of conventional solar cells, passivated emitter rear cell (PERC), has seen an annual improvement of 0.5 to 0.6%. As their efficiency approaches 23%, most recombination loss are attributed to metal contact, making contact passivation a significant area of investigation for the last several decades. Among various approaches and materials studied, the Tunnel Oxide Passivated Contact (TOPCon) design has garnered the most interest in the industry [25]. The proposed industrial TOPCon process pathways consist of steps that are either fully or partially transferable from the cutting-edge PERC cell, supplemented with a few extra steps essential for boosting conversion efficiency. The benefit of this evolutionary approach is the ability to upgrade existing PERC production lines for TOPCon processing with a minimal addition of process steps, assuming sufficient space is available in the PERC facility.

The 'International Technology Roadmap for Photovoltaics' provides a general overview of the current technological trends within the crystalline silicon PV industry based on inputs from leading international producers, manufacturers, suppliers, research institutes, and consultants [26]. While covering the entire process chain, the general trends for upcoming cell technologies (Figure 1-7) give insight into where industry is going, and research needs to help.

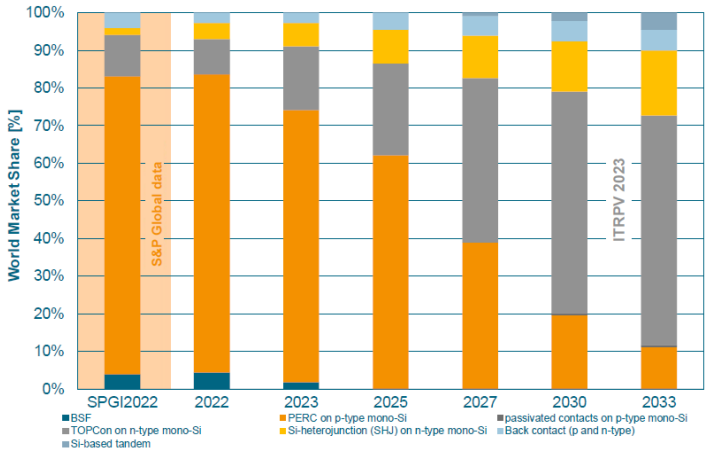

Figure 1-7: Market shares for different cell technologies [26]

The TOPCon design has generated the highest level of interest in industry due to it is potential with a projected 60% market share in 2033 up from 10%

in 2022. With creating fully new manufacturing pathways not being a viable route, the appeal lies within the ability to fully or partially adapt current state-of-the-art PERC methodologies with a few modifications [25]. The significant reduction in cost in contrast to creating everything from scratch is the main driving factor, and with laboratory scale conversion efficiencies reaching over 26% [27].

Currently, TOPCon production is primarily based on low pressure chemical vapour deposition (LPCVD) (Figure 1-8) however, plasma-enhanced chemical vapour deposition (PECVD) has an advantage due to simplifying the cell processing. Industrial viable architectures have been suggested for following these routes for optimal reduction in the overall cost of manufacturing [25].

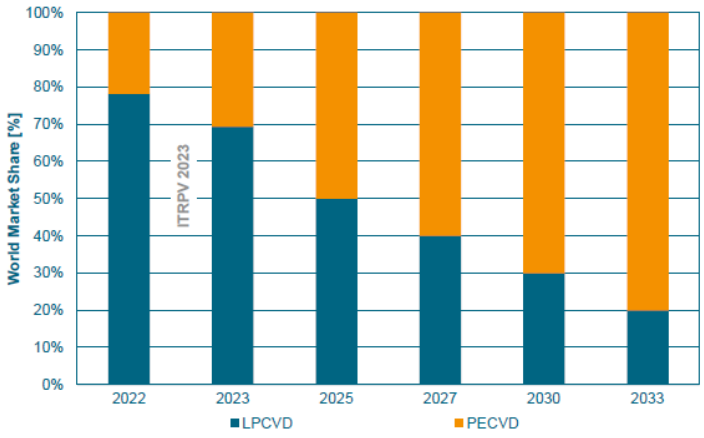

Figure 1-8: Expected trend of forming the polysilicon layer of TOPCon contacts [26]

While Tandem cells are projected to begin production in ~2027 (Figure 1-7) the secondary cell to silicon is still being researched. While there are many different types being developed (Figure 1-9) comparing the record efficiencies reached, number of papers reached, and timespan, Perovskites show promise with a meteoric rise to equal efficiencies of silicon and CIGSe within a 10-year timespan.

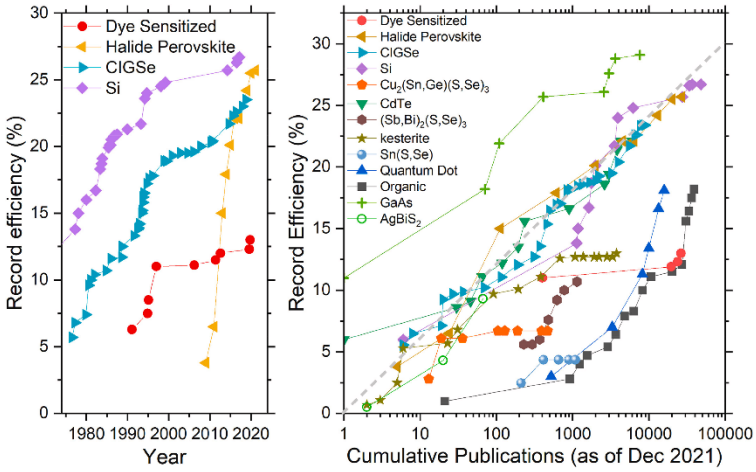

Figure 1-9: Left) Record certified efficiency vs. time for four selected single-junction PV technologies Right) Record efficiencies for a larger set of technologies as a function of cumulative publications since the first working solar cell was announced.

1.5 How A Solar Cell Works

The concept of capturing sunlight or light radiation and transforming it into electricity has been around since the 19th century. In 1839, Edmond Becquerel observed the photovoltaic effect when he illuminated silver chloride within an acidic solution, leading to the generation of voltage and current. Subsequent advancements and optimizations occurred over time, culminating in the development of a more efficient prototype by Bell Labs in 1954.

The photovoltaic effect's underlying mechanism is simple and has remained consistent since introduction. A solar cell consists of a junction formed by p- and n-doped semiconductor materials (Figure 1-10). The p-type dopant lowers the Fermi level, bringing it closer to the valence band, while the n-type dopant raises the Fermi level, moving it closer to the conduction band, where electrons become free to move.

When a photon with sufficient energy is absorbed by the semiconductor material, it generates an electron-hole pair, freeing the electron and promoting it to the conduction band (E_C). The depletion region's electric field then sweeps the freed electron away into the n-type side cathode. Simultaneously, the electric field pushes the resulting free hole in the opposite direction, towards the p-type side anode. This process generates an electromotive force (EMF) that creates a potential difference between the

anode and the cathode.

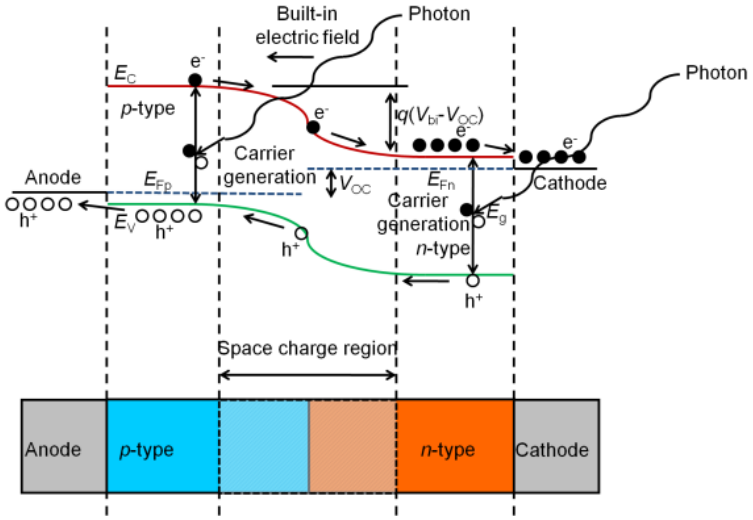

Figure 1-10: Band diagram of a solar cell showing the energy levels of the electron-hole pairs and the potential difference generated by the cell during photon absorption [28]

1.6 Measurement Location

Ex-situ, in-line, and in-situ measurements are different approaches to acquiring data in various experimental and industrial manufacturing processes (Figure 1-11). These measurement techniques differ in terms of when and where the data are collected and the level of interaction with the sample or process under investigation.

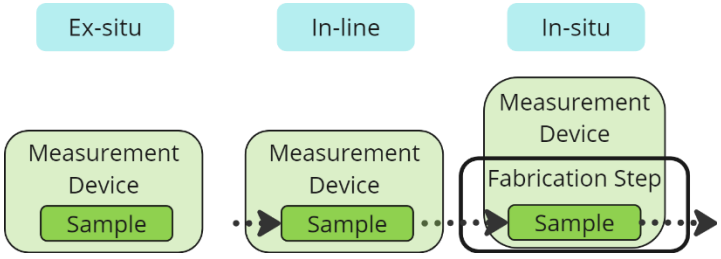

Figure 1-11: Depiction of 3 different types of measurement locations, ex-situ, in-situ, in-line

Ex-situ measurements refer to the analysis or characterization of a sample or system outside its native or operational environment. A sample is typically removed from the process, and measurements are performed under controlled conditions. This approach enables precise control over the

measurement conditions and often provides high-resolution data.

In-line measurements are performed between processes without interrupting the flow. These measurements are taken directly within production lines for real-time monitoring They are advantageous because of the continuous data that helps identify trends, optimize the process, and ensure product quality. In-situ measurements involve the characterization of a sample without removal from the system. It aims to capture the sample's properties or system parameters during the process, providing a more accurate representation of the conditions. It is particularly useful for understanding dynamic processes. Indeed, in-situ measurements offer several significant benefits compared to other in-line and ex-situ, however, developing an in-situ measurement system that can be easily transferred between different systems poses several challenges due to the unique requirements constraints of each system. Some of the main difficulties associated with the development of a versatile in-situ system are hardware compatibility and high measurements rates [29]–[36].

1.7 TECHNOLOGY READINESS LEVEL

Technology Readiness Level (TRL) is a widely used method for assessing the maturity of a technology, from its inception to its eventual implementation. Originally developed by NASA in the 1970s, TRLs are now used by various organizations, including government agencies, research institutions, and private companies, to gauge the readiness of a technology for practical use. TRLs are generally divided into nine stages (Figure 1-12), ranging from the lowest level of maturity (TRL 1) to the highest level (TRL 9). Here is a brief overview of each TRL level:

1. Observation of basic principles.
2. Formulation of technology concept/application.
3. Analytical & experimental proof of concept.
4. Lab based component validation.
5. Relevant environnent component validation.
6. System/subsystem prototype in relevant environment.
7. System prototype in operational environment.
8. Completed system with test & demonstration.
9. Successful operations prove system.

Each TRL represents a specific milestone in the development process, allowing ease of understanding for the status of a technology and to determine the next steps needed for advancement.

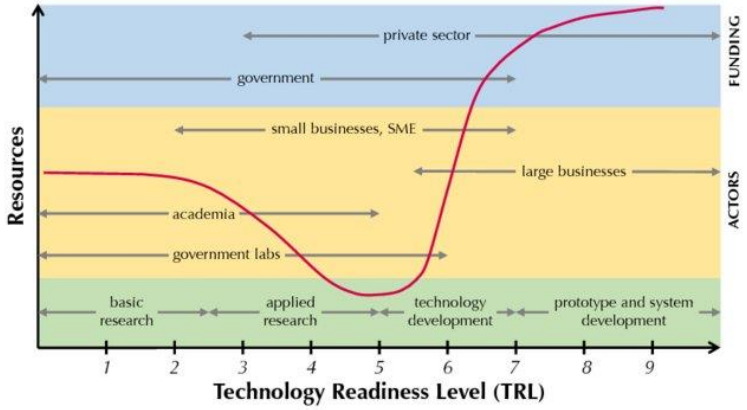

Figure 1-12: The accessibility of resources for the development of new products at different Technology Readiness Levels [37]

A crucial point is the innovation gap or, "Valley of Death", (Figure 1-12 red line) which represents a critical phase in a technology's lifecycle, where it has advanced beyond basic research but has not yet demonstrated its full potential or commercial viability. This gap can stall the technology's progress, as it struggles to attract resources necessary for further development, thus careful planning is required.

1.8 THESIS OBJECTIVE

The primary objective of this thesis is to advance the development of an in-situ technique to the end of TRL4, encompassing both hardware and theory which has thus far been developed to TRL2/3 [34]. Additionally, the study aims to demonstrate the potential use cases of this technique for future research endeavours, while also enabling ex-situ and in-line characterization capabilities for use within an industrial setting.

Chapter 2 covers the construction of a suitable optical system for simple integration between systems and minimal effort building and the retrofitting of a PECVD reactor.

Chapter 3 focuses on the theory of the measurement technique itself, initially improving what was previously developed then creating a new simpler theory to perform direct measurements instead of indirect.

Chapter 4 applies the improved theory to view various fast phenomenon for aluminium oxide which can occur during fabrication as it is a crucial material in current PERC and TOPCon architectures.

2 HARDWARE

In this chapter, we will delve into the construction of hardware, which will be divided into two sections. The first one will concentrate on improving the in-situ device to ensure seamless compatibility with industry-standard components. The second section will cover the retrofitting of a Plasma-Enhanced Chemical Vapor Deposition (PECVD) reactor:

2.1 IN-SITU HARDWARE DESIGN

The basis of the in-situ measurement device technique involves illuminating the back of a silicon sample (Figure 2-1) within a PECVD reactor, using above band gap energy photons to create photoluminescence emission which is then collected. This allows for a simpler implementation for in-situ monitoring (τ_{eff}, PL) rather than analysis from the front due to electron diffusion. The technique itself is explained in section 3.4.

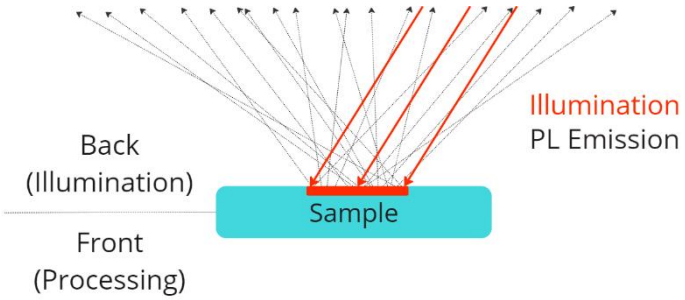

Figure 2-1: Basic working principle for in-situ τ_{eff} and PL measurement techniques in [34].

2.1.1 Plasma-Enhanced Chemical Vapour Deposition

PECVD is a Chemical Vapor Deposition technique in which a material is deposited on a substrate in the form of a thin film with the aid of a plasma [38]. The process typically involves the introduction of a gas mixture of precursor compounds into a chamber that is maintained at a reduced pressure. The gas mixture is then activated by a plasma, which is created by applying an RF power source to the chamber.

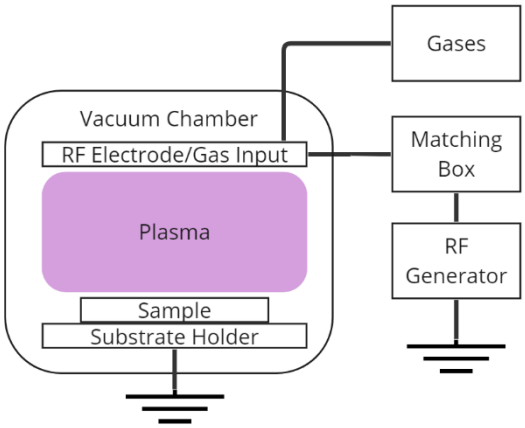

Figure 2-2: Schematic of a PECVD system consisting of a vacuum chamber, a gas input for providing the reactant gases, a matching box, and a radio frequency (RF) power source for generating the plasma.

Gas molecules are ionized in PECVD through a process called electron impact ionization [39]. The ionization process begins when an RF power source is applied to the chamber, creating an oscillating electric field. This field causes free electrons in the medium to be accelerated, gaining kinetic energy. Some of these accelerated electrons will collide with gas molecules, transferring their kinetic energy and causing the latter to become ionized. This creates positively charged ions and free electrons in the chamber, which form a plasma.

In the production of various types of solar cells, PECVD plays a crucial role as a deposition technique. Its versatility allows for even application on wide surface areas, such as solar panels or flat panel display. This method enables a high degree of process control by modifying the plasma composition to finely tune the refractive index of the optical coatings. This is particularly important in the production of solar cells, which efficiency depends on the uniformity and quality of the various layers that make the cell. It can be used to deposit a variety of thin films that are important in solar cell manufacturing, including a-Si:H as a passivation layer, silicon nitride as an anti-reflective coating, silicon oxide and aluminium oxide films as passivating layers [40], [41].

2.1.2 Substrate Holder

The substrate holder of the PECVD reactor can be opened to load and unload the samples (Figure 2-3). A sample is placed onto a heated platform capable of 450°C achieved with a clamped heating element, using a high temperature

thermal paste, between two halves including two thermocouples for temperature measurement, supported on two pillars. This is mounted on an ISO-K flange on which there is a window port and a laser input port. In the middle of the substrate holder there is a hole allowing for illumination of the back of the sample (Figure 2-1) and for the emitted photoluminescence to be collected through the window port.

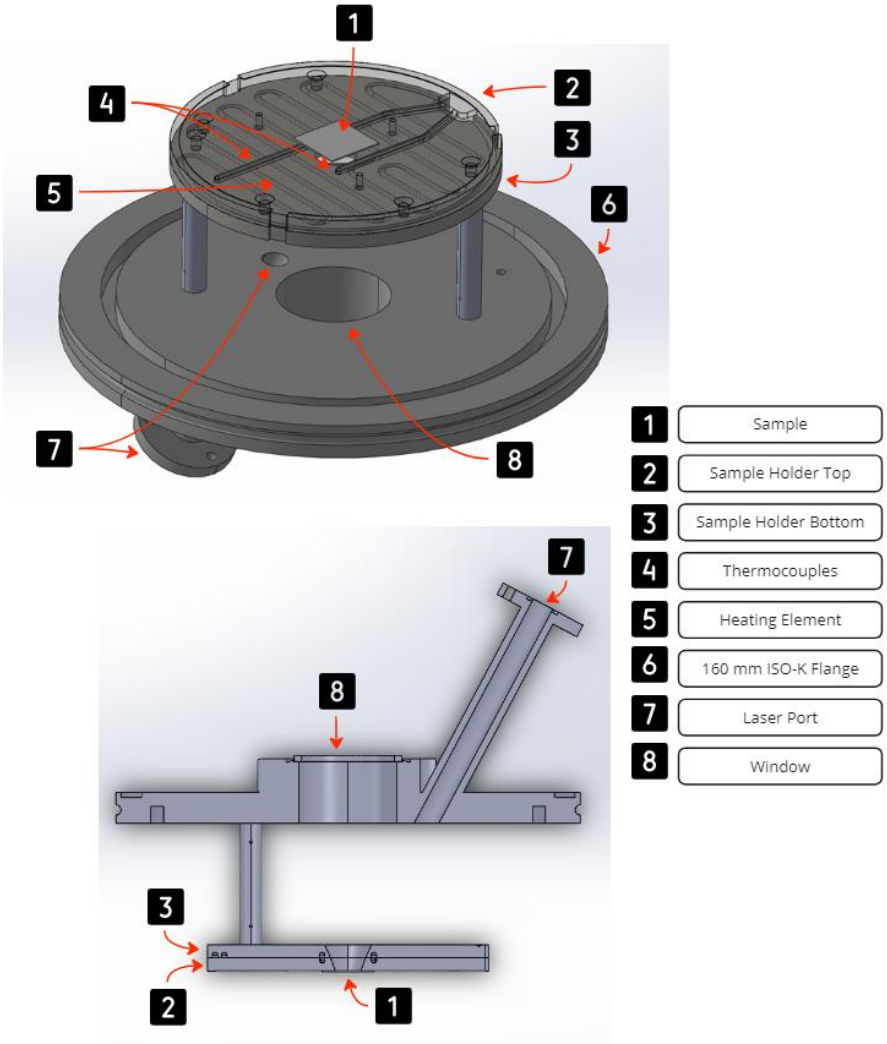

Figure 2-3: Substrate holder design showing a sample placed on top of the heated substrate centered over a hole with various elements labelled.

2.1.3 Optical Collection Systems

For the collection of luminescence emitted from the sample two optical collection and excitation systems are available (Figure 2-4). The previous optical system, highlighted by two red boxes one for the laser input and

other for collecting the PL emissions, which was upgraded to include PL and MPL at the same time and placed onto a motorized linear rail, and the new system, green box, which was developed for modularity and ease of transfer to meet the increasing TRL requirements and industry-standard component compatibility.

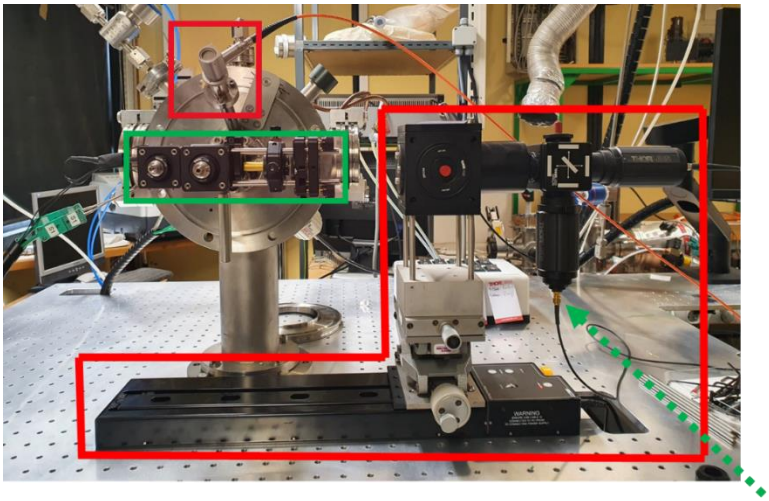

Figure 2-4: Both previous and new in-situ optics systems mounted onto the PECVD reactor.

A full explanation of the laser system, and previous optics can be found in *[34]*. Whilst the optics were upgraded the laser system was not. A full diagram of the system can be seen in *Figure 3-41*.

2.1.3.1 Precious Optics

Most of the previous optics system (Figure 2-5) was developed involving the collection of PL emissions for performing either τ_{eff} or PL measurements [34]. The base design principle involves an 8 mm diameter beam being shone onto the sample at an angle of ~30 degrees through the laser input port with the resulting PL emission being collected through the window port behind the sample. An off axis parabolic mirror is used for collecting the light from the sample for further collimation and focusing onto either an InGaAs photodiode for MPL or a fibre optic cable for PL. The design was further upgraded with the addition of a dichroic beam splitter and a secondary focusing lens, allowing for simultaneous τ_{eff} and PL. It is worth noting that a secondary system was also previously built that attached onto one section of a cluster tool [34].

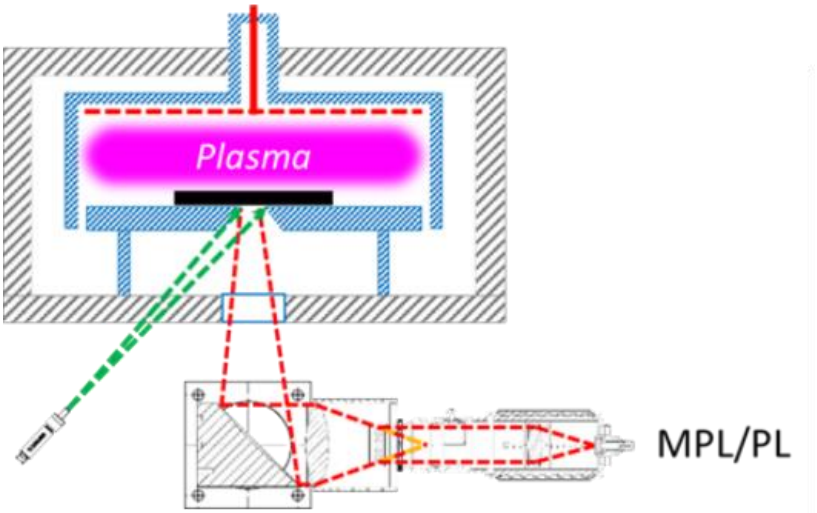

Figure 2-5: Schematic of the previous optical system.

When considering modularity and simplicity of integration into another system, the main design pain points focus on collection and illumination. This design requires two separate ports, one for the laser and a second for collection and a linear rail system which is not easily transferable between systems. For collection, gaussian optics was used, however, the area of contention is the amount of light being lost due how the light is collected from the sample using the off axis parabolic mirror (Figure 2-6) or any optics which focuses to a point when collecting from an area. Partially the angled illumination as well.

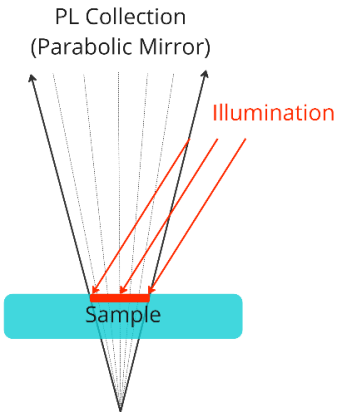

Figure 2-6: Ray diagram of collected PL emission when using gaussian optics and indication of illumination path.

As an 8 mm diameter circle is being illuminated the PL emission area must be considered as an infinite amount of point sources from which the emissions come from (Figure 2-7). This indicates many emitted photons will not travel along the focus lines required for collection and final focusing using the parabolic mirror, a type of gaussian optics.

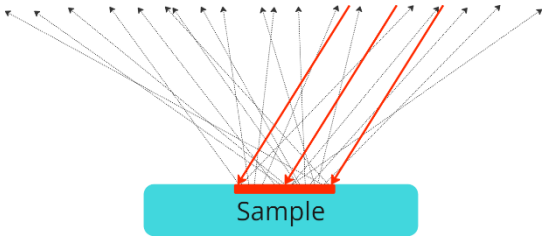

Figure 2-7: Depiction of the PL emission rays from an illuminated area.

To determine the amount of light lost within the system, a simple test regarding the intensity focused onto the photodiode area used for MPL and to a greater area was performed. Using a Thorlabs PM160T light meter (Figure 2-8) the measured power comparing the full sensor area (314 mm^2, Ø10 mm) to that of the InGaAs photodiode sensor (Thorlabs SM05PD4A, 0.8 mm^2, Ø1 mm) size was found to be 4 times as strong. This indicated that when using gaussian optics, there is a lot of light being incorrectly focused within the system, thus, showing room for improvement. This does not account for angled light of any sort; it was just a reading from the display screen.

Figure 2-8: Thorlabs PM160T wireless light meter [42].

2.1.4 Geometrical Optics

Geometrical optics is a branch within optics regarding treating light as a ray. Light is treated as a collection of rays travelling in a straight line which alter course when passing through a change in refractive index or reflect from a surface (Figure 2-9) [43]. The refraction and reflection of light at the interface between different refractive indexes can be described in the framework of

geometrical optics by using the Fresnel formulas.

Ray-based modelling of light propagation was first developed by Plato (428 BC–328 BC) while the wave nature of light was developed in 1690 and is used to describe phenomena such as diffraction and interference, which cannot be explained by the ray-based model of geometrical optics, each field having a large amount of progress since the first ideas arose [44]. Both models have their own strengths and limitations, and they are often used together to provide a comprehensive understanding of the behaviour of light.

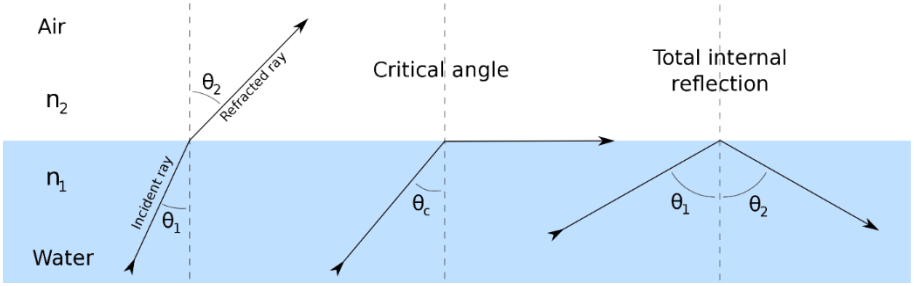

Figure 2-9: Depiction of refraction and internal reflection for light propagation[45]

2.1.4.1 Imaging Optics

Mirrors and lenses are both commonly used for light collection and image formation (Figure 2-10), both have unique advantages and disadvantages, but the most suitable choice will depend on the specific requirements of the end application such as cameras, binoculars, microscopes, or telescopes.

Mirrors are more cost-effective than lenses and easier to manufacture in large sizes, making them a popular choice for applications that require a large field of view or a high level of light collection. Additionally, they do not suffer from chromatic aberrations, which can be a problem with lenses. Lenses, on the other hand, are more versatile and can be designed into compact complex optical designs. They also offer the ability to correct for chromatic aberrations and other optical distortions, making them ideal for applications that require high image quality.

The James Webb Space Telescope is a prime example of a large-scale mirror structure which using lenses would not be possible. At the other end of the spectrum are Smartphone cameras, which designed to be compact and lightweight, so they have small lenses.

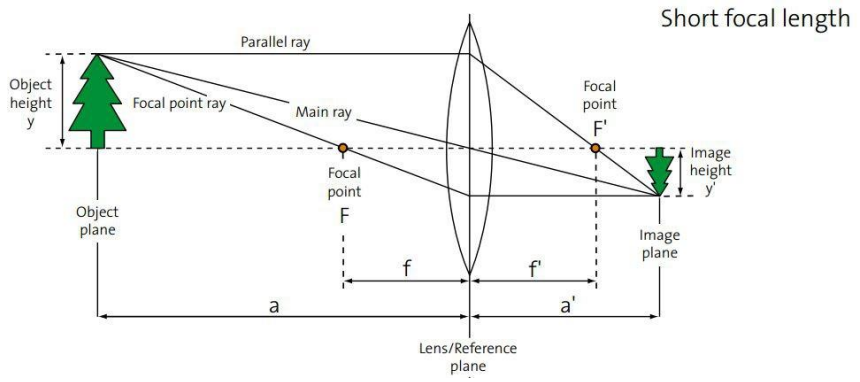

Figure 2-10: Optical image transmission through a bi-convex lens [46].

Typically, the optical material of a lens is a transparent dielectric material such as fused silica, N-BK7, Sapphire, and other materials with a spherical curvature on the front and back surfaces. Based on the material the wavelength transmission percentage will vary, which, when paired with antireflective coatings (hard refractory-oxide coatings), can minimize surface reflections within specific wavelength ranges. Mirrors on the other hand use metal reflective layers such as aluminium, gold, silver, rhodium, or broadband dielectric coatings which have a narrower range of wavelength operation.

2.1.4.1.1 Optical Aberrations

In a perfect world, a perfect lens would form perfect images, and these would be capable of perfectly focusing light to a spot limited in size only by diffraction. Optical aberrations, however, are a part of lenses and reduce the ability to form high-quality images, collimate a beam, or focus perfectly to a point. These can be split into two subgroups, chromatic and monochromatic aberrations, where the aberration either is or isn't dependant on the energy (frequency) which light has during propagation through the medium. Monochromatic aberrations are caused by the inability of spherical surfaces to focus light correctly far from the axis and are common to both mirrors and lenses. One such effects, spherical aberration (Figure 2-11 left), can be seen on point source collimation where lower incident angles are essentially collimated, and higher angles converge. Other effects such as coma and astigmatism can occur, which relate to the off-axis light rays that converge imperfectly, causing point sources to appear as comet-like shapes, and light rays from different planes focus at different points, leading to elongated focusing.

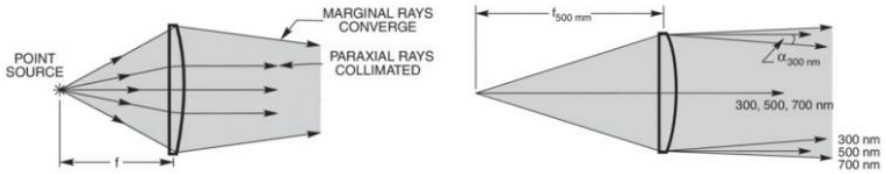

Figure 2-11: Effects of spherical aberration (left) where smaller angles are collimated with large angles converging, and chromatic aberration (right) on collimation when a point source is at the focal point [47].

2.1.5 Non-Imaging Optics

In contrast to imaging optics, non-imaging optics does not attempt to for an image; rather it focuses on the optimal transfer of light between a source and a target. [48] They are used in applications where the primary goal is to manipulate or control light distribution, such as illumination, solar energy collection, or optical signal collection, rather than forming a clear, sharp image [49], [50]. To increase signal-to-noise ratio in measurement equipment, such optics are commonly used increase the amount of light (signal) that is collected and directed towards a photodiode [51]–[53].

2.1.5.1 Compound Parabolic Concentrator

A Compound Parabolic Concentrator (CPC), a type of non-imaging optic, is made via the rotation of an offset and rotated parabolic curve around a central axis (Figure 2-12) [54]. The large input (d_1) collects the divergent light with internal reflections concentrating the light at the small output (d_2) via changing of the lights angle compared to the optical axis. The main defining property of a CPC is the acceptance angle which defines the angular range in which a CPC can collect light. Two of the four main parameters, namely, input diameter (d_1), acceptance angle (θ), length (L), and output diameter (d_2), can be used to design a CPC.

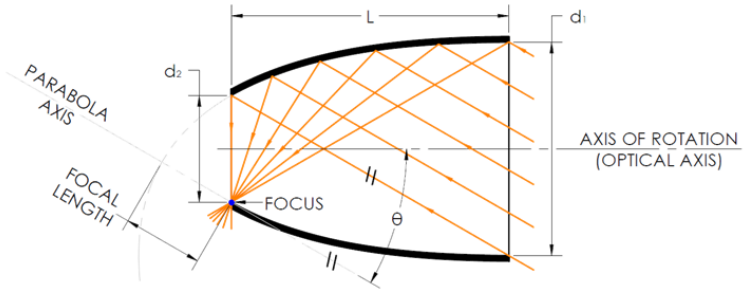

Figure 2-12: Compound Parabolic Concentrator schematic depicting the

rotated off axis parabola and maximum acceptance angle for incoming light rays [50].

Due to the relationships between the four parameters, it can result in a design which is difficult to manufacture or leads to a limitation in physical dimensions. No theoretical upper limit exists for the concentration capacities of a CPC (Figure 2-13), however, as the acceptance angle decreases, the length and input to output ratio increases significantly and as the acceptance angle approaches 0 it effectively becomes a standard parabolic reflector.

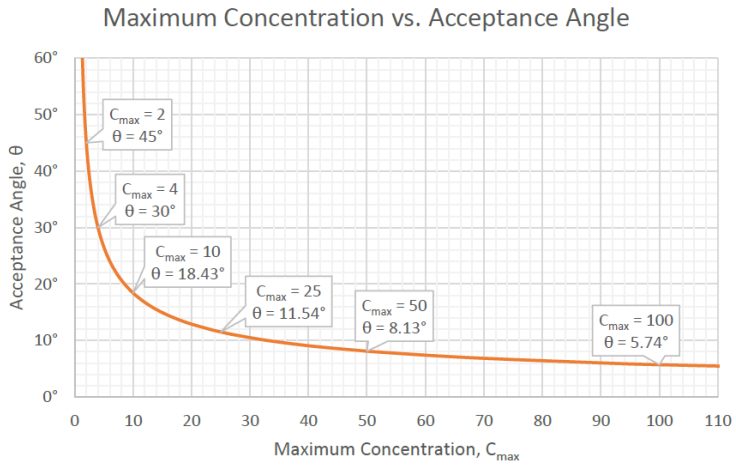

Figure 2-13: Maximum concentration ratio vs acceptance angle for a CPC [50].

The maximum concentration curve (Figure 2-13) represents a boundary condition for CPC concentrators. Any combination of concentration and acceptance angle that exist below the curve is possible to achieve with variations on the design, such as truncation, and could yield a smaller output angle. However, points above the curve are not physically possible for the standard design of CPC [54].

2.1.6 Ray Tracing

Optical ray tracing is a computer simulation method used to model the path of light through an optical system. The basic idea is to trace the path of light rays through the system and calculate how the rays are affected by the different optical elements they encounter. This can be used to predict the behaviour of the modelled system.

A ray tracing simulation begins by specifying the position and direction of one or more light rays at the start of the optical system. A simple test case is

calculating the collimation of light from a point source using a plano-convex lens (Figure 2-14). The simulation then follows each ray as it propagates through the system, calculating how the ray is affected by each optical element it encounters involving reflection and refraction with all the optical aberrations. It's a powerful tool that allows for quick testing of different optical designs and to optimize the performance of a system before it is built. It can be used for a wide range of applications, such as designing camera lenses, telescopes, microscopes, and other imaging systems.

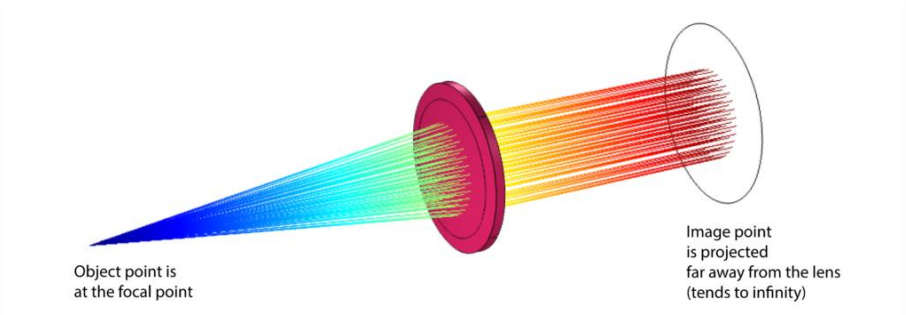

Figure 2-14: Comsol ray tracing simulation of a plano-convex lens [55].

2.1.7 Photodiode Radial Sensitivity

A photodiode is a semiconductor-based optoelectronic device that converts incident light into electrical current through a process called the photoelectric effect. It is a type of photodetector capable of sensing and quantifying the intensity of incoming light, sensitive within a certain wavelength range, typically in the visible, ultraviolet, or infrared spectrum. Photodiodes are used in a wide range of applications, such as optical communications, spectroscopy, imaging, and sensing.

The incident angle of light, angle at which light strikes the photodiode surface, (Figure 2-15) is an important factor to consider when designing or using a photodiode because it can affect the signal intensity. When light strikes the surface of a photodiode at a normal (perpendicular) incidence, most of the light is absorbed. However, when light strikes the surface at an angle, some of the light can be reflected or refracted and not absorbed.

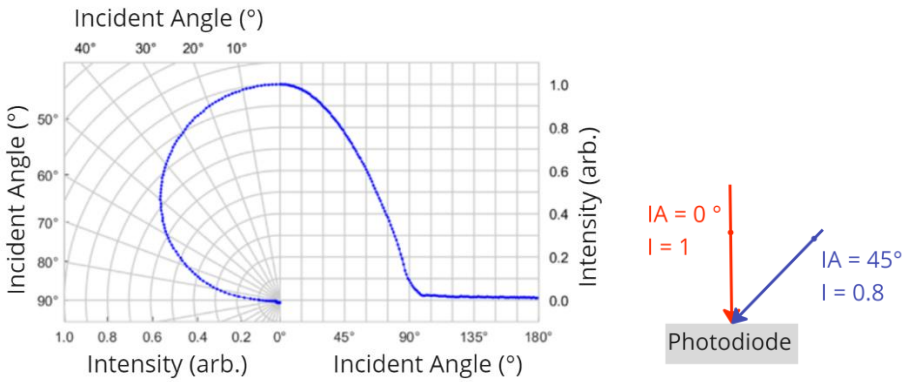

Figure 2-15: Incident angle vs photodiode intensity (silicon).

Indium Gallium Arsenide (InGaAs) and Silicon (Si) are both commonly used materials for photodiodes. Both have their own unique properties and are suitable for different applications. Silicon Photodiodes are the most common type of photodiodes and are well-established in the market. They have a wide range of spectral response, from visible light to near infrared, with peak sensitivity in the visible and near infrared range of about 0.4 - 1 micrometers. They have good responsivity and low noise, making them well suited for general-purpose applications such as light sensing, optical communications, and imaging. They are also relatively low cost, which makes them a popular choice for many applications. In contrast, InGaAs photodiodes while similar have a few differences to Silicon Photodiodes. They have a much broader spectral response range than Silicon Photodiodes, extending from the near visible to the long-wavelength infrared (~1.7 µm) with a higher responsivity in the infrared range, which makes them more suitable for detecting photoluminescence emitted by silicon.

2.1.8 New optical design

Given the loss of light and hardware compatibility requirements, the collection optics must also be capable of surviving the TRL valley of death without the need for heavy redesigning. For this the basic requirements are the illumination and collection light must pass through the same port, the collected light must be focused with minimal losses, and mounting the device should be simple.

2.1.8.1 Compound Parabolic Concentrator with a Monte Carlo simulation

To reduce the amount of light lost within the collection optics the approach to collect light from an area rather than a point source required switching from Gaussian to non-imaging optics. This is also to remove the need for

focusing or requiring distance to be considered when mounting the device to a certain extent.

A Monte Carlo ray tracing simulation was built in MATLAB for a CPC (8-degree acceptance angle with a Ø2 mm output) with an 8 mm diameter source (Figure 2-16) at 100 mm from the input. The specifications of the CPC were chosen as rough dimensions for what was easily purchasable at the time, and the set distance being approximately the current distance between the collection window and back of the sample (Figure 2-3).

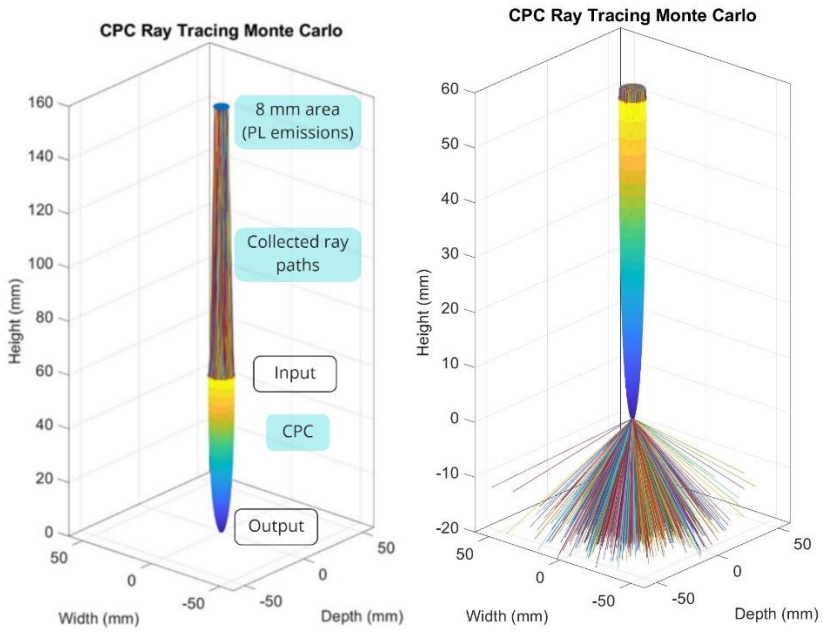

Figure 2-16: Left) A Monte Carlo ray tracing simulation of light emission from a circular source collected with a CPC Right) Zoomed into the CPC showing the output as well.

Performing the stochastic simulation, the PL emission was modelled with 4,000 rays (Figure 2-16). All the collected light rays which entered the CPC input were concentrated into the output without any loss of light for the given collection area. The trade-off for being able to collect light in such a way is a change in the angle of light, within the CPC during compression, due to constant reflection on the CPC surface. This results in the angle with relation to the axis of rotation increasing when exiting the CPC, unless it passed directly through the input and output without reflection in which case it's maximum angle will be the acceptance angle.

As coupling to an InGaAs photodiode was required and the response intensity becomes lower at larger angles an initial arbitrary plane with distance of 1 mm from the output was chosen with a circle of Ø1.5 mm for the evaluation of the collected light rays (Figure 2-17). 60% of the rays go within the Ø1.5 mm circle with a mean AOI of ~30 degrees (Figure 2-17). Higher angle of incidence (AOI) are in the border regions showing these will be many of the rays to be lost when changing distances.

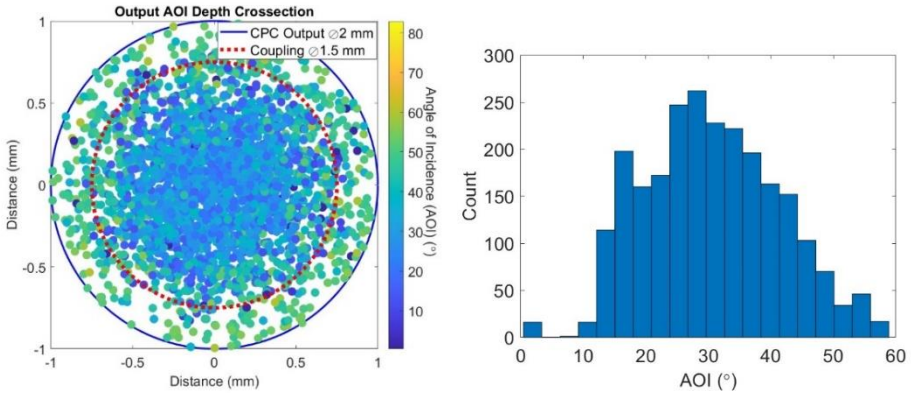

Figure 2-17: Left) Angle of incident for incoming photons onto a plane 1 mm from the CPC output. Right) Histogram showing the spread.

Given the radial sensitivity of a Si photodiode reaches 0.5 intensity at 70 degrees, for an InGaAs photodiode, a large majority of the light should be collected. A more thorough investigation could be performed via measuring the angular response curve of the InGaAs photodiode used. Varying the distance from the CPC output while imposing a maximum AOI for the Ø1.5 mm coupling region shows the % of rays collected tends to lower % collected regardless of an AOI restriction, however the maximum % collection peak also moves (Figure 2-18). This is performed for 20 – 35 degrees in 5-degree steps to compare. For practical use, placing a photodiode directly at the end of a CPC will result in the highest signal possible given the % of output light

collected decreases so significantly with distance.

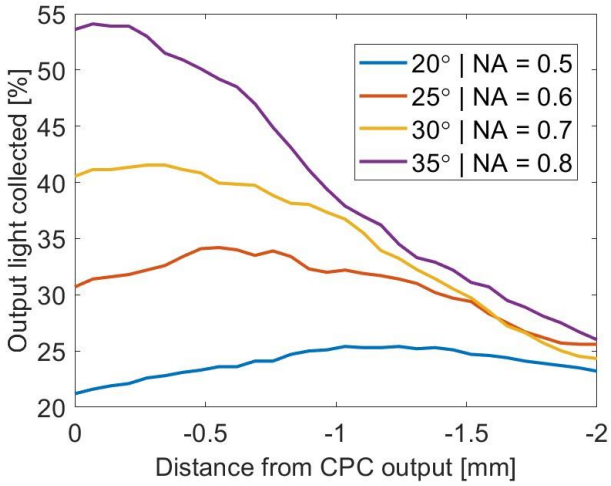

Figure 2-18: Percentage of output light collected with a maximum AOI into the collection area shown in Figure 2-17 based on distance from the output and NA values calculated for FP1500URT fibre cable.

When attempting to collect to an optical fibre, clear limitations come into play based on the need for rays to enter a material. The limiting factor will be the numerical aperture (NA) of the optical fibre.

Modelled using a Thorlabs FP1500URT 0.50 NA, Ø1500 µm Core Multimode Fiber the refractive indexes of the core and cladding were used to simulate the percentage of light collected based on different NA values required (Figure 2-18). Due to the NA limit of the fibre optic in contrast to the photodiode, only a maximum of 25% light collection at NA 0.5 is possible. To overcome this, a metamaterial lens (superlens) designed for collimating light from a semi sphere input could be used for coupling most of the collected light removing the need to consider what the NA value is [56].

2.1.8.2 Collimated Light Collection

Given the design principle of simple compatibility being followed, and a CPC not being a viable option for fibre collimation and a spectrometer being a very useful scientific tool, the usual point to point method for PL collection had to be examined. Switching to using a collimator (Figure 2-19) removes the needs to account for distance. To test how well such a setup would work, a 1064 nm Air-Spaced Doublet Collimator (Thorlabs F810SMA-1064) with an Ø8 mm collimation was used to compare the PL emissions from 5 cm and 20 cm, which is less and more than the sample distance within the PECVD

reactor.

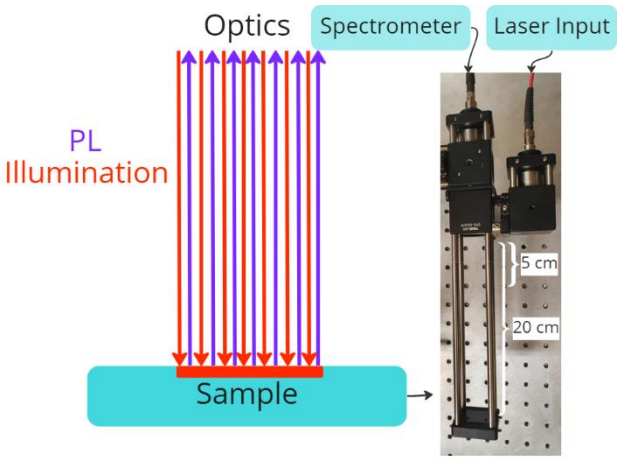

Figure 2-19: PL emission collection via a collimated lens

Using an Ocean Optics NIRQUEST+ 1.7 spectrometer the silicon PL emission peaks at 1000 – 1200 nm of the two distances are compared (Figure 2-20). The acquired spectrums indicate there should be no problem for larger distances.

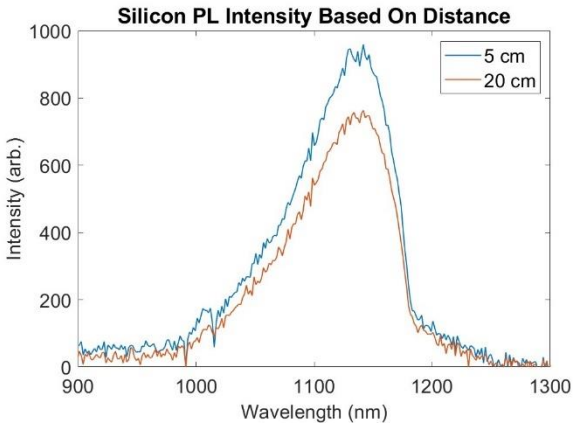

Figure 2-20: Comparison of PL intensity using a collimator setup as indicated in Figure 2-19.

2.1.8.3 New design

Combining the CPC and collimated optics componentry, a new optical system was built for simple mounting onto an industry standard CF flange window port via the THORLABS cage system, which are off the shelf components. The optical system (Figure 2-21) consists of a laser beam passing through a top hat beam profiler reflecting off a right-angled mirror

and dichroic filter before illuminating the sample. The dichroic filter reflects light above a threshold energy and passes that which is below. The resulting PL emission passes through the dichroic filter and is split into two paths of equal intensity via a polka dot beam splitter for collection using the CPC and collimator. A polka dot beam splitter is an array of reflective silver squares which covers 50% of the area.

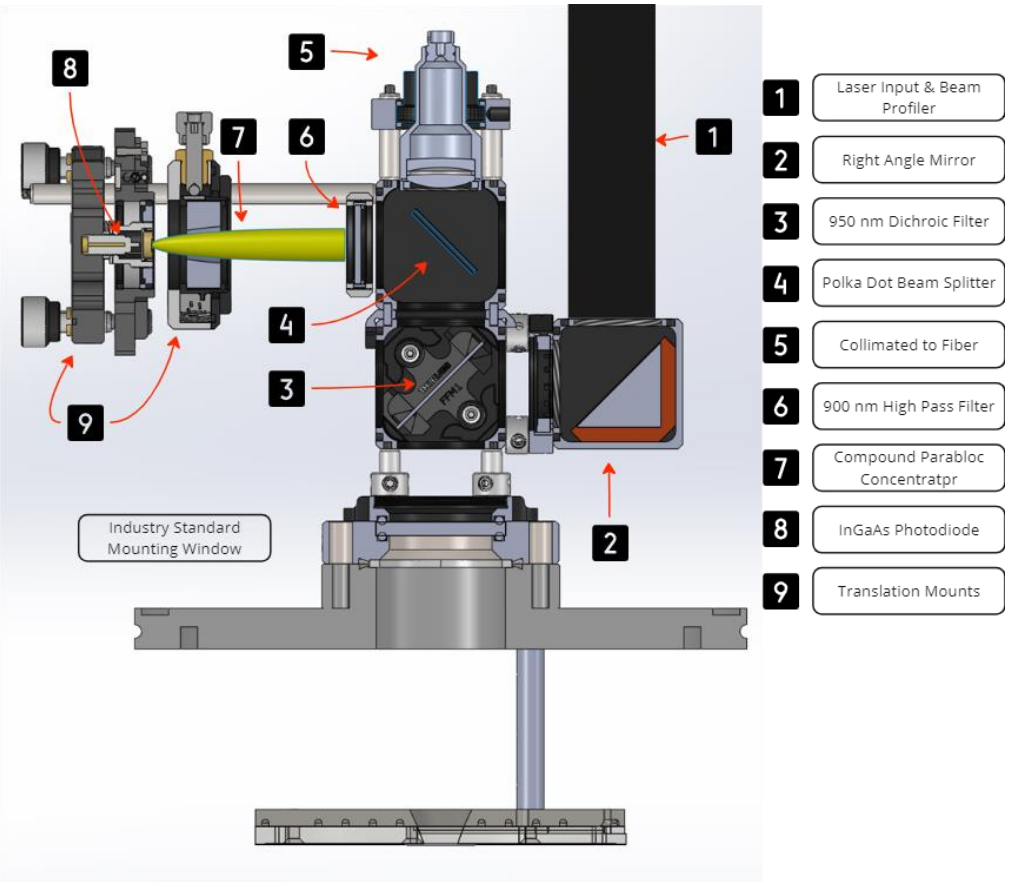

Figure 2-21: Schematic layout of the new optical design using non-imaging optics for τ_{eff} and PL.

Illuminating the sample through the same optical port also allows for the improvement of the illumination beam being perpendicular (Figure 2-22) to the sample rather than on an angle as with the previous design. A top hat beam profiler (Asphericon a|TopShape) was used which is designed to change an input gaussian beam profile to a top hat profile with a 1m sustainability improving on the previous design of using a single mode fibre coupled to a multimodal then a collimator to create a top hat profile. This also reduces the need to account for any form of angular reflection of the beam with the sample.

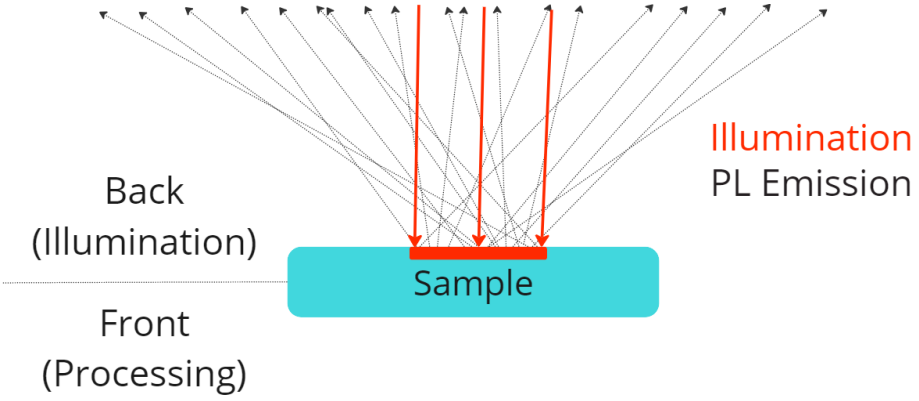

Figure 2-22: Illumination pathway using the new optical setup.

The fully built version of the new optics design (Figure 2-23). It is placed within a box made from non reflective material and copper plating on the outside. A mirror is placed under the sample to improve signal collection.

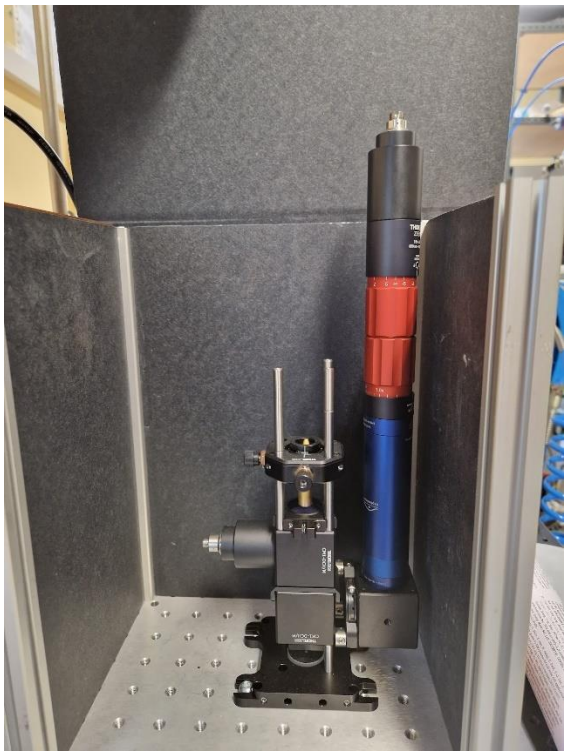

Figure 2-23: New optical design within a black box and faraday cage (copper plating on the external faces of the black box)

2.1.8.4 Direct Optical Comparison

A comparison between collection capabilities of the CPC and off axis parabolic mirror using the original laser input port and placing the collection

aperture of the CPC at the same location as the offset parabolic mirror was performed. A signal strength to collection area ratio of 20:1 was found when comparing equal collection areas calculated from 19.79 cm^2 and 0.5 cm^2 aperture sizes used for the test. It should be noted that this value will change based on the CPC design and location, the comparison is to show a much smaller collection aperture can be used to achieve the same signal strength which is capable of being built into a simple device.

2.2 PECVD Reactor Retrofitting

The PECVD reactor being used (Figure 2-24) has been around for a while (~ 30 years), with minor upgrades being performed throughout the years however nothing extensive. Given the need for efficiency, an upgrade was needed so it was rebuilt. The reactor setup consisted of the three tables indicated accordingly: 1) PECVD reactor & MPL, 2) InGaAs & Si monochromator, 3) valve control system.

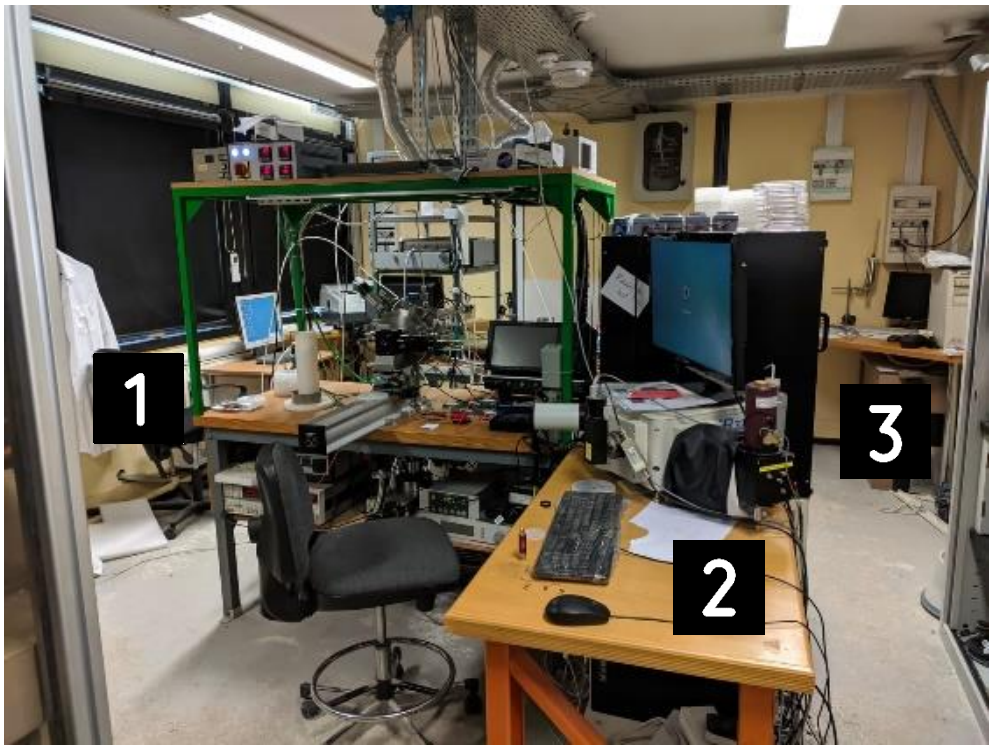

Figure 2-24: PECVD reactor used at the start of the PhD with the MPL setup attached.

2.2.1 Componentry

The core component of a PECVD reactor are no doubt the plasma generation

system however, one must not neglect the remaining components such as the pumps, valves, and sensors (Figure 2-25). An automated system with a simple user interface increases the speed, efficiency, and reproducibility of the deposition process. The specific components and design of the system may vary depending on the application and materials being used. For a full understanding of what each vacuum component does, viewing the description documents provided by manufacturers such as Pfeiffer-vacuum, MKS, and Brooks is most suitable. To control the PECVD reactor an Advantech ADAM 4000 control unit was used, this is a programable logic controller (PLM). MATLAB was used to create the user interface (Figure 5-2) for the reactor employing the app designer and instrument control toolbox.

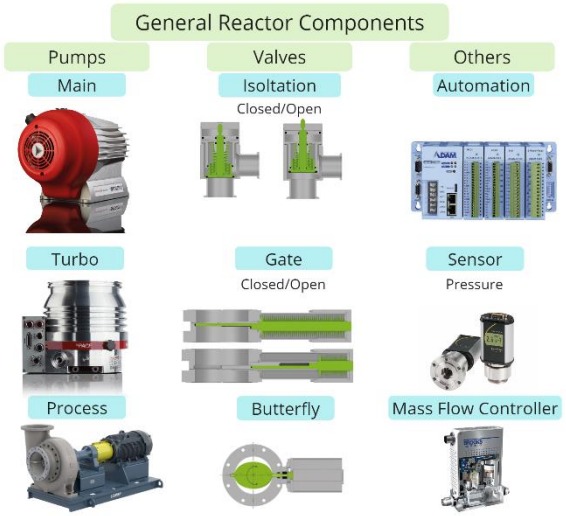

Figure 2-25: Componentry used to build a reactor which requires a vacuum.

2.2.2 Reactor Retrofit

The retrofitted PECVD reactor was built using its core components and integrated on the left part of a workstation using a custom-made tabletop (Figure 2-26). The initial reactor was stripped to its main chamber, pumps, and plasma generation system, and retrofitted to be fully automated. New gate valves, pneumatic valves & controllers, pressure gauge, gas control, and software were included in the design. The mass flow controllers were mounted in a separate area and only the electrical componentry was modified to interface with the PLM. The left side of the workstation was dedicated to the PECVD reactor while the right side was for the control system and an anti vibration table to place the laser system and electronics.

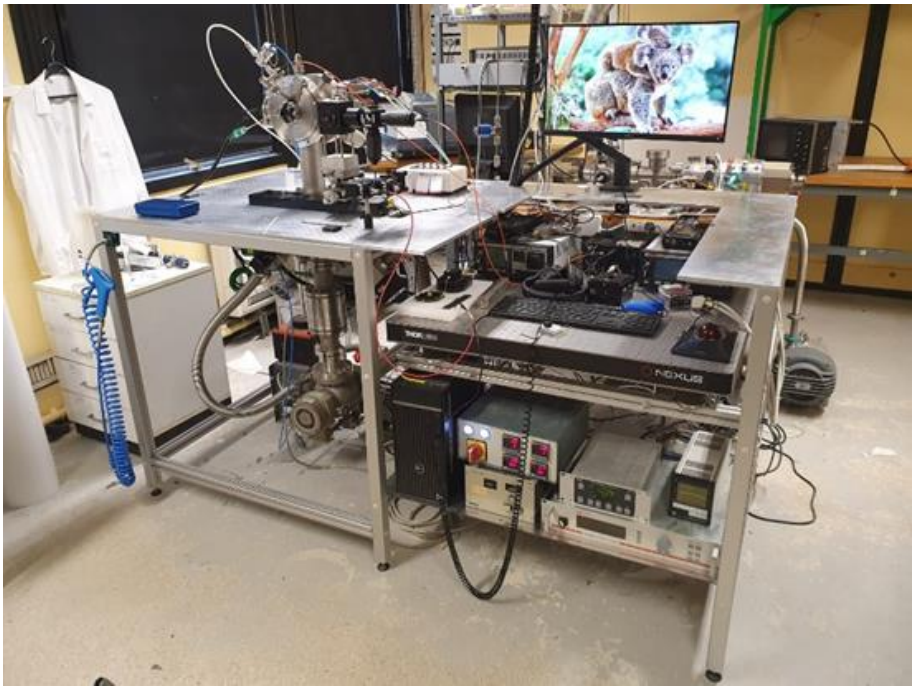

Figure 2-26: Retrofitted PECVD Reactor (left) with in-situ MPL & PL workstation (right).

The main change in reactor design was the addition of a butterfly valve before the turbo pump (Figure 2-27). This allows for low pressure depositions to be performed in the future. Certain deposition processes create particles which are in general not suitable for a turbo pump, however, if nitrogen is introduced into the turbo pump bearings this can offset the damage occurred from particles travelling through the turbo pump and allow longer use.

The new design given is one based on the previous and is by no means a standard given the long history and variation of reactor designs. It should be considered a design of best practice for the desired application of this PECVD reactor.

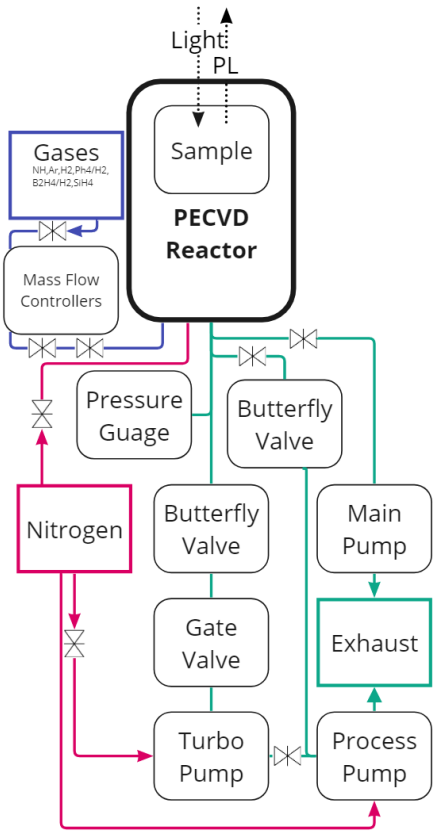

Figure 2-27: Retrofitted PECVD reactor design.

2.3 CHAPTER REVIEW

- A new optical system was designed combining the laser and collection optics into one system, for one optical window, using non-imaging optics (CPC) for photoluminescence collection and a top hat beam profiler for illumination allowing up to a 1-meter distance from the sample. This is particularly useful for implementing the system on any industrial process line, with varying distances between the samples to be examined and the PL and MPL set-ups.
- The PECVD reactor was retrofitted from manual to automatic model, allowing for a better control and reproducibility of the processes.

3 MINORITY CARRIER LIFETIME

Lifetime measurements, capturing the duration over which certain states or events persist, are instrumental across an array of scientific fields. They are integral to understanding the behaviour and optimizing the functionality of systems ranging from semiconductors in physics, fluorophores in biophysics and biochemistry, reactive intermediates in chemistry, phosphorescent materials in materials science, radioactive isotopes in nuclear physics, drug metabolites in pharmaceuticals, to stars in astronomy.

Minority carrier lifetime is a fundamental property in semiconductors that plays a crucial role in determining the potential efficiency and performance of a solar cell during the fabrication process. It is defined as the average time that a carrier (electron or hole), injected into a region where it is a minority, spends before recombining (Figure 3-1), based on the dominant recombination type.

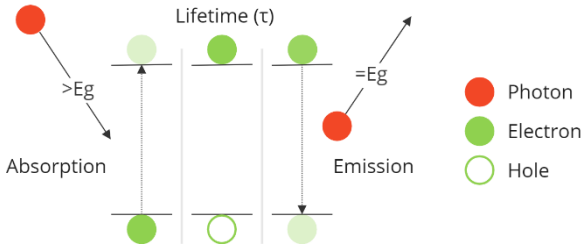

Figure 3-1: Process of an electron absorbing the energy from a photon, generating an electron-hole pair which lasts for a period of time (lifetime), and the recombination of the electron emission of a photon.

The intensity of light will determine the excess carrier density and dominant recombination type, resulting in a lifetime (Figure 3-2).

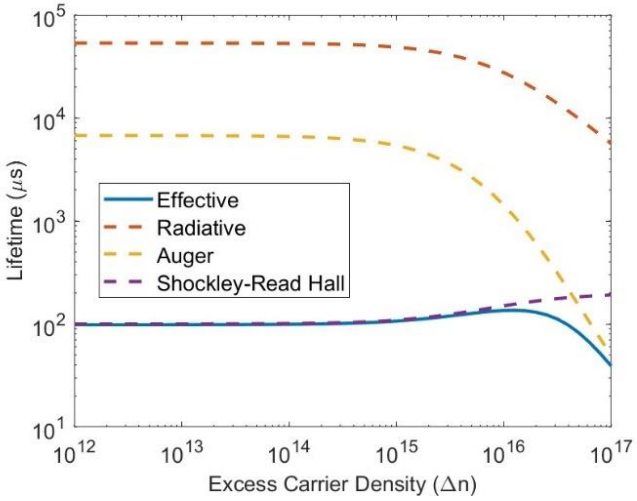

Figure 3-2 : Effective minority carrier lifetime as a function of the excess carrier density and its decomposition into the respective 3 recombination processes: radiative, Auger, and Shockley-Read-Hall . Figure obtained from simulation at pvlighthouse.com.au with settings in (Figure 6-4).

3.1 RECOMBINATION TYPES

One of 3 processes (Figure 3-3) occurs during an electrons lifetime (τ_{eff}). Radiative losses involving the emission of a photon, Shockley-Read Hall (non-radiative) recombination is trap assisted, and Auger recombination from the transferring of energy. In indirect semiconductors, recombinative losses are mostly associated with phonon generation. The dominant recombination process will determine the overall τ_{bulk} measured at the given excess carrier density given by the following equation:

$$\frac{1}{\tau_{bulk}} = \frac{1}{\tau_{Rad}} + \frac{1}{\tau_{Aug}} + \frac{1}{\tau_{SRH}} \qquad \text{Eq 3.1}$$

- Radiative recombination is a process in which an electron in a semiconductor recombines with a hole, resulting in the emission of a photon. It is responsible for the generation of light in optoelectronic devices such as LEDs and lasers.
- Auger recombination is a nonradiative process in semiconductors where an electron recombines with a hole, releasing its excess energy to another carrier (either an electron or a hole) instead of emitting a photon.
- Shockley-Read-Hall (SRH) recombination is a nonradiative recombination mechanism in semiconductors. It occurs when an electron recombines with a hole by interacting with a defect or

impurity in the material.

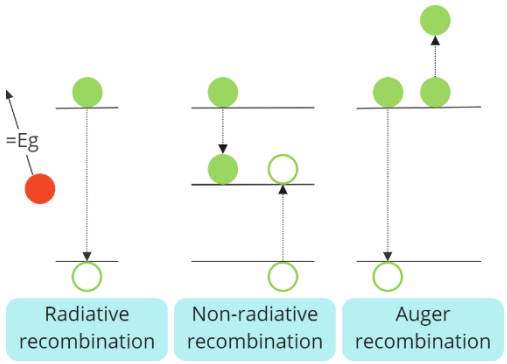

Figure 3-3 : Depiction of Radiative recombination and 2 processes of non radiative recombination

As the surface of a semiconductor has a high density of dangling bonds, the recombination of charge carrier occurs via defect-assisted process. The effective minority carrier lifetime value τ_{eff} is thus heavily dependant on surface quality passivation, relating directly to solar cell performance.

$$\frac{1}{\tau_{eff}} = \frac{1}{\tau_{bulk}} + \frac{1}{\tau_{surf}} \qquad \textit{Eq 3.2}$$

3.2 METHODOLOGIES

There are many ways to measure the effective electron lifetime such as time-resolved photoluminescence, time-resolved microwave conductivity, transient photocurrent, self consistent determination, and modulated photoluminescence (MPL), Figure 3-5, Figure 3-6, Figure 3-7 [57]. However, the choice of measurement technique depends on the specific material or device being studied, and it is important to carefully consider the advantages and limitations of each method.

Photoconductance decay (PCD) is a well-known contactless method for the evaluation of minority carrier lifetime in Si which does not require specific device fabrication [58]. An light pulse creates electron-hole pairs in the semiconductor and increases its conductance. When the light source is shut-off, recombination processes occur and the excess minority carrier density decreases, which is monitored [58]. The exponential microwave decay signal has a characteristic time τ, which is the lifetime of the minority carriers and its value indicates the quality of a layer stack (Figure 3-4). While the technique can work in transient mode for minority carrier lifetime higher than 200µs, another version exists: the quasi-steady-state PCD for lower lifetimes. The technique's strength is the contactless nature and rapid measurement

needing both sides of the sample to be passivated, in order to reduce surface recombination effects and allow extraction of the effective lifetime.

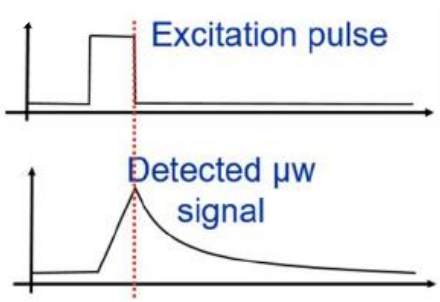

Figure 3-4: Example of a decay curve for lifetime determination after an excitation pulse.

Photoluminescence decay is another method of monitoring the time dependence of excess minority carriers. Similar to PCD, excess carriers are generated by a short light pulse with a photon energy higher than the bandgap. In contrast with PCD, the excess carrier density is monitored through the time-dependence of the photoluminescence emitted from radiative recombination of electron-hole pairs, and not from conductance.

Photoluminescent imaging has also become a widely used technique for characterizing silicon samples throughout the entire photovoltaic value chain [59]. It was first demonstrated on large-area silicon wafers at the University of New South Wales in 2005, and within a few years, it became a standard method for process monitoring in R&D [60]. The main drawback is the PL signal is strongly influenced by the optical properties of the sample, which means that a separate calibration is necessary for each distinct type of sample. Several calibration methods have been presented in the literature, such as correlating PL imaging data with non-spatially resolved data from quasi-steady-state photoconductance (QSSPC) or with self-consistently calibrated quasi-steady-state photoluminescence [57].

The starting method being used for the in-situ measurements, MPL, is explained in Section 3.3.3.

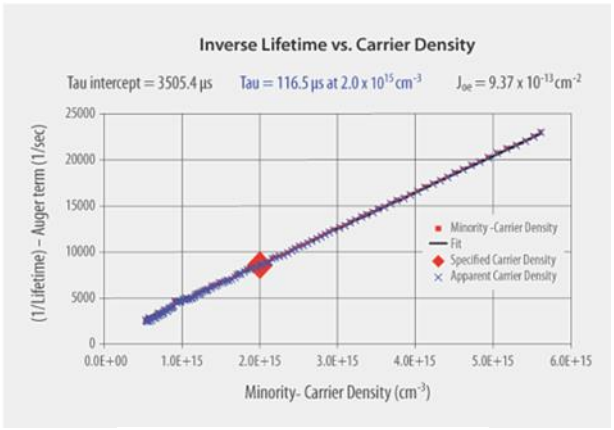

Sinton instruments

Figure 3-5: Example of results output from a WCT-120 manufactured by Sinton instruments using they curve theory

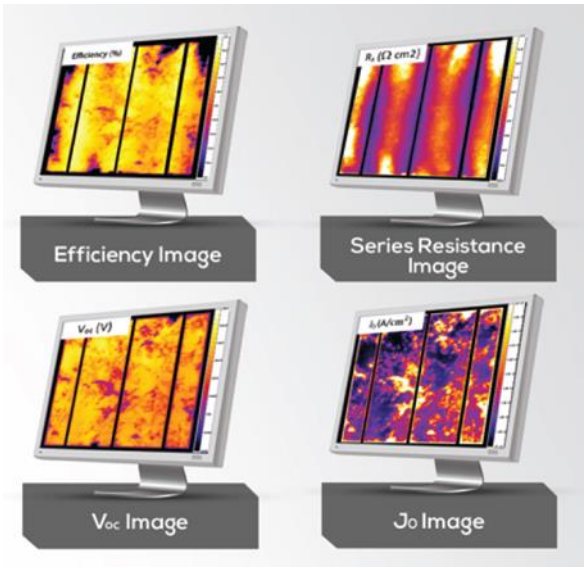

BT imaging

Figure 3-6: Example of results output from a PL imaging device manufactured by BT imaging

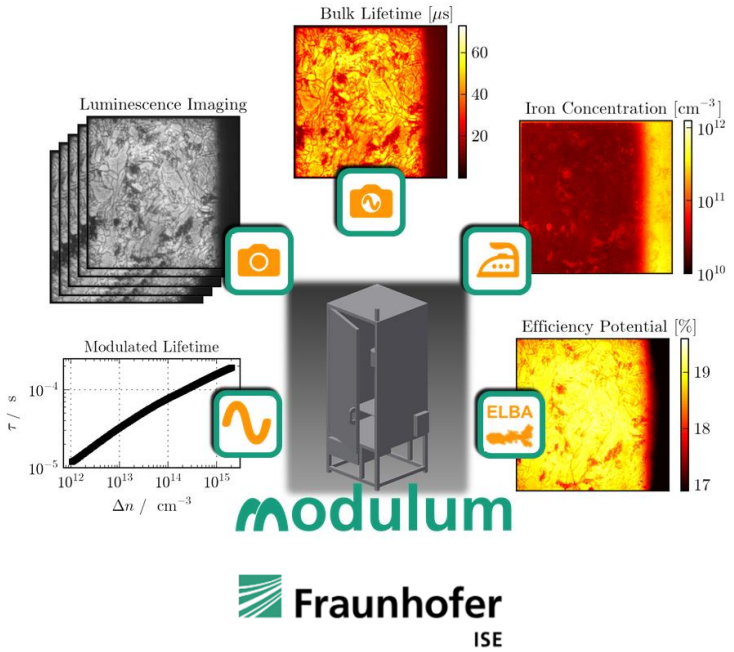

Figure 3-7: Example of results output from a PL imaging device manufactured by Fraunhofer ISE

3.3 WAVELETS

A wavelet transform is a mathematical tool used to analyse data in a localized manner, meaning that it can identify patterns and features in a specific region of a signal or data set [61], [62]. It works by decomposing a signal or data set into a series of wavelets, which are functions that are localized in both time and frequency.

Wavelets are usually constructed by starting with a basic waveform, called the "mother wavelet," and then dilating and translating it to generate a series of wavelets that are scaled and shifted versions of the mother wavelet (Figure 3-8). The wavelet transform decomposes a signal or data set into these wavelets, allowing the analysis of specific frequency ranges or time periods. As the scale (frequency) of the mother wavelet is changed it either decreases the frequency resolution with an increase in time (higher frequency), or increases the frequency resolution and decreases in time (lower frequency).

The wavelet transform has several advantages over other types of signal processing techniques, such as the Fourier transform. It allows for the analysis of data in the time domain, as well as the frequency domain, and can accurately represent data with non-stationary characteristics.

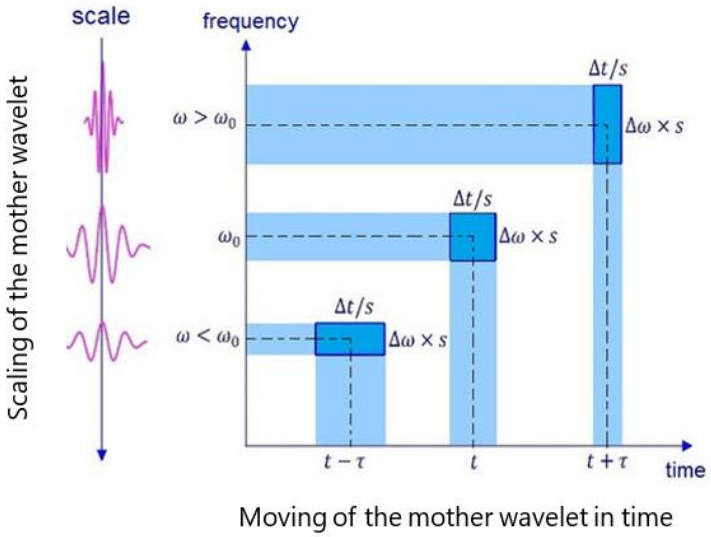

Figure 3-8: Dilated and translated of the mother wavelet with resolution in the frequency/time domain [63].

The differences with mother wavelets are the resolutions within the time and frequency domains for pattern recognition (Figure 3-9). The mother wavelets shown are a small portion of the possible variations, with their real and imaginary parts. The real part corresponds to the oscillatory behavior or variation in the signal. It captures the changes in amplitude and phase of the signal as it evolves in time. It is essential for analyzing and representing the time-domain characteristics of a signal. It provides information about the signal's dominant frequency and how it varies over time. The imaginary part complements the real part by capturing the phase information of the wavelet. It represents how the wavelet oscillations lead or lag behind the real part. In other words, it encodes the temporal shifts or phase differences in the signal's behavior. While the real part tells you about the signal's amplitude and frequency content, the imaginary part tells you how that content is distributed over time.

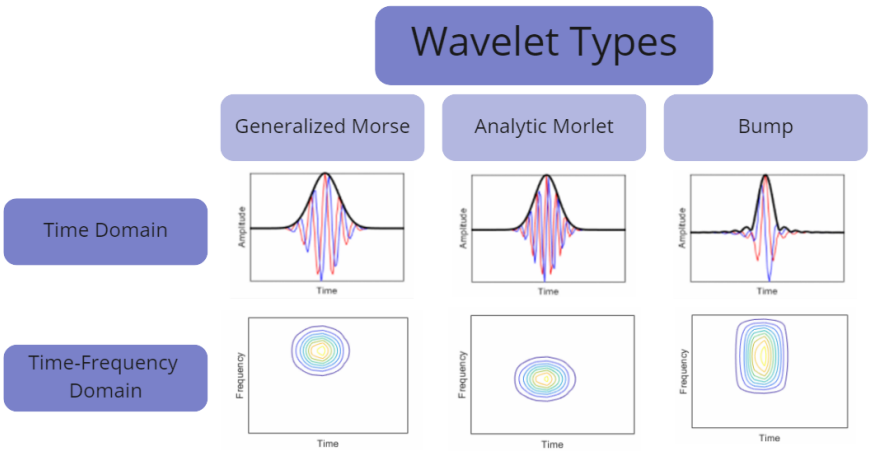

Figure 3-9: Three wavelet variations used with the wcoherence function for phase shifts in MATLAB with pre-set feature in the time qnd frequency domains.

There are several challenges and issues that can arise when working with wavelet transforms: i) The choice of wavelet can significantly affect the performance of the wavelet transform. ii) Different wavelets have different properties, and it is important to choose a wavelet that is well-suited for the signal being analysed. iii) Boundary effects can be introduced at the edges of the signal, which can affect the accuracy of the transform. iv) They can be computationally intensive, especially for large signals. v) This can make them impractical for use in real-time applications or on systems with limited computational resources.

3.3.1.1 Wavelet coherence

Wavelet coherence is a technique/function used to analyse the similarity and phase relationship between two or more signals [64], [65]. It is an extension of the standard wavelet transform, which decomposes a signal into its frequency components. The wavelet coherence transform uses the wavelet transform to decompose both signals into the same set of frequency components and then calculates the correlation between the coefficients at each frequency. The result is a measure of the coherence between the signals at each frequency, which can be used to identify the frequency bands where the signals are most similar (Figure 3-10). This technique is useful for identifying relationships between signals in fields such as signal processing, geophysics, and neuroscience. It can be represented graphically as a coherence function, which is a function of frequency (Figure 3-11) with the yellow patches showing domains of coherency between the signals.

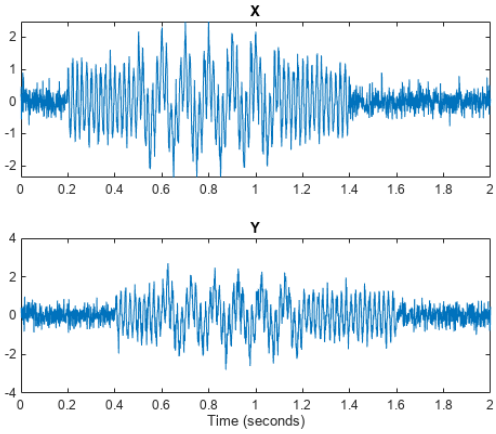

Figure 3-10: Two coherent signals with two distinct frequency regions [66]

The wavelet coherence function is displayed as a two-dimensional plot, with frequency on the y-axis and a coherence colorbar scale. One of the key advantages of the wavelet coherence transform is that it can identify both frequency-specific and time-specific relationships between signals. This is useful in many applications where it is important to understand how different signals are related over time and across different frequency bands. The wavelet coherence is calculated by taking the ratio of the cross-spectrum to the product of the individual spectra, where the cross-spectrum is calculated by convolving the wavelet transform of one signal with the complex conjugate of the wavelet transform of the other signal.

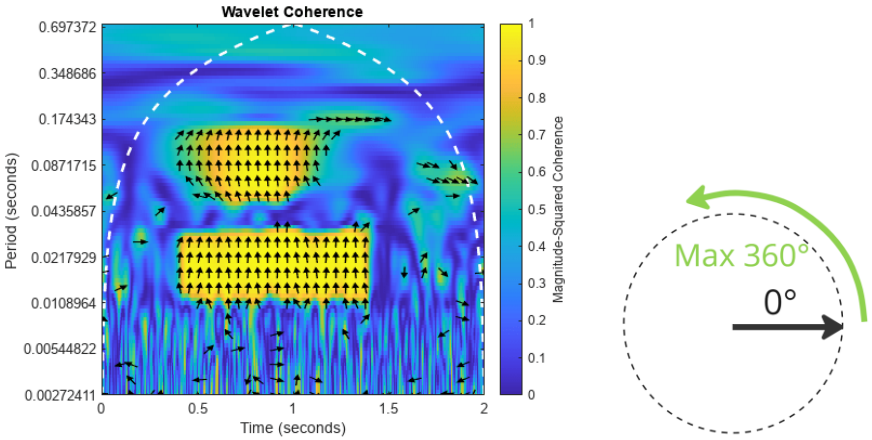

Figure 3-11: Left) Wavelet coherence graph of Figure 3-10 [66] Right) How to read the phase shift between signals.

In addition, wavelet coherence can reveal phase relationships between signals. The phase difference between two signals at a given point in time

can provide important information about the nature of the relationship between them. For example, in some applications, such as speech analysis, the frequency/phase relationship can indicate whether two signals are synchronized or not.

As the wavelet transform uses a wavelet basis function that is localized in both time and frequency, and the frequency resolution of the transform is not constant across all frequencies (Figure 3-8,Figure 3-12d), this can result in the frequency bands appearing to be elongated, especially at lower frequencies where the frequency resolution is lower.

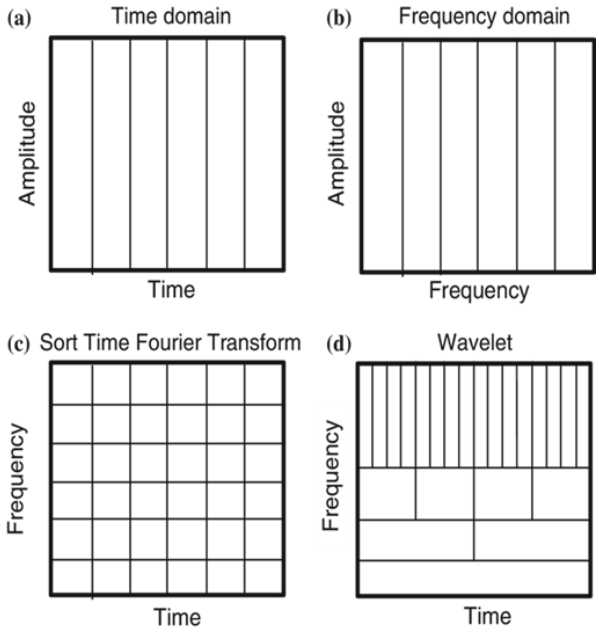

Figure 3-12: Signal analysis of the time, frequency domains. a) Signal/time (Signal measurement) b) Frequency/spectral (Fourier Transform) c) Frequency/time (STFT) d) Time and Frequency (wavelet transform)

3.3.2 Lissajous Curve

A Lissajous curve is a type of curve that is formed by the graphical representation of the relationship between two sinusoidal signals (Figure 3-13). It is named after Jules Antoine Lissajous, who first studied these curves in the 19th century.

Lissajous curves are used in a variety of applications, including oscilloscope calibration, audio engineering, and scientific research. They are also used in the study of mechanical vibrations and in the analysis of electrical signals.

The most famous application of the concept is in the form of fractals, and they are also a feature of the Josephson effect (particularly in the case of iron or some superconductors) and the diffusion of black body radiation.

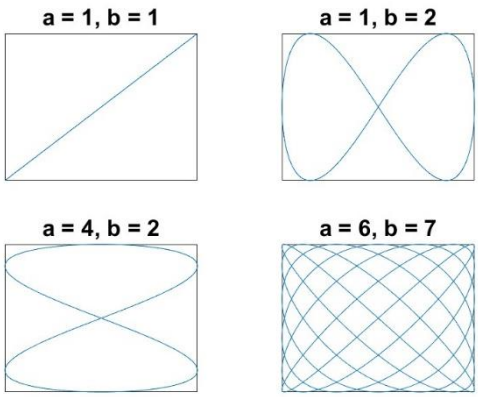

Figure 3-13: Lissajous figure with varying ratios of a/b

A Lissajous curve is typically plotted by using the two sinusoidal signals as the x and y axes of a graph (Eq 3.3). The resulting curve is a closed loop if the frequency ratio of the two signals is a rational number, and an open curve if the frequency ratio is irrational (a/b). The shape of the curve depends on the specific frequencies and phase differences of the two signals. The a/b ratio will determine the scaling ratio shifting from a square to rectangular outline. Adding a phase shift to either equation will act as a rotation of the image produced. The values for A and B are explained in section 0, briefly, one will be large while the other will be small.

$$x = A * sin(at), \;\; y = B * sin(bt) \qquad \text{Eq. 3.3}$$

Modulated Photoluminescence

Modulated photoluminescence is a technique involving the measurement of photoluminescence as a function of an applied excitation waveform. In relation to semiconductor physics, MPL has been widely used for two applications:

1. Determining the lifetime τ_{eff} of electrons via use of the low frequency range (0.1 - 1 kHz) for understanding the passivation qualities of a semiconductor material during fabrication processes. [33], [67]
2. Defects characterization in thin films photovoltaic materials using the high frequency range (up to MHz) [68]–[70]

Overall, MPL measurements are useful for studying the optoelectronic properties of materials, characterizing materials for use in optoelectronic devices, studying the dynamics of electron-hole pairs, and determining the lifetime of electrons.

3.3.3 Working Principle for MPL

MPL was introduced within semiconductor physics to determine the τ_{eff} at a steady state excitation intensity (SSI) (Figure 3-14) [71]. This can be understood by attempting to relate two points in time between two straight lines, one point being in the excitation intensity and the other in the PL emission intensity. For in-situ measurements this is of particular interest as it would be an extremely fast method of lifetime measurement. The issue is it requires the measurement to be done in an immaterialistic manner which has not been done before.

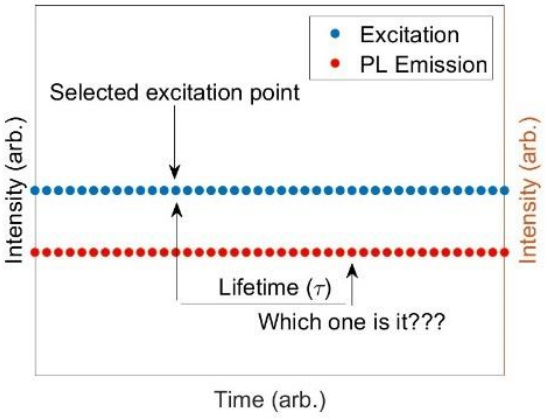

Figure 3-14: Problem statement of lifetime at a steady state intensity

To overcome this, MPL uses a small amplitude sinusoidal wave was applied to the excitation beam to create a quasi-steady state in which the wave is fundamentally equal to a straight line with the addition of having a piece of information related to it, frequency (Figure 3-15).

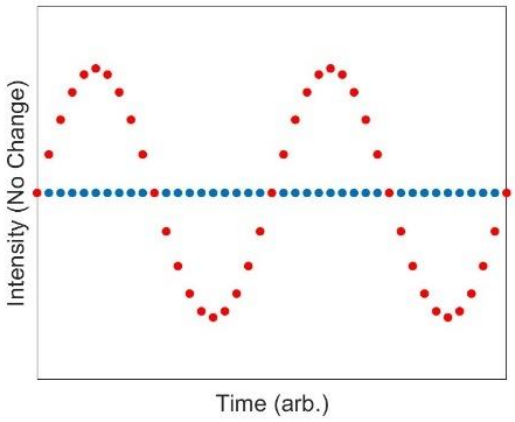

Figure 3-15: A small amplitude wave as a quasi-steady state approximation of a line used for MPL.

Thus, when performing the excitation, the PL emission will be of the same frequency and to maintain the quasi-steady state requirement the phase shift must be equal during the rise and fall of the applied signal (Figure 3-16), i.e. no noticeable hysteresis, and a minimal amplitude.

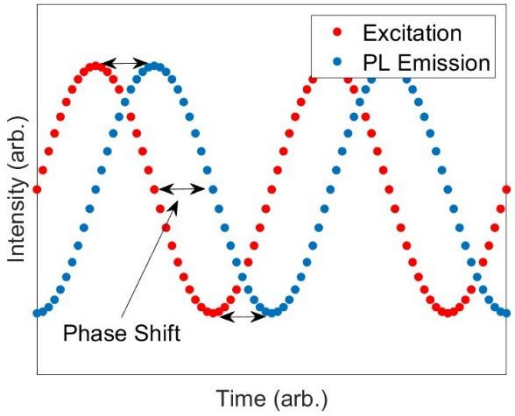

Figure 3-16 : Comparison of the input standing wave to the ouput standing wave with a visible phase shift

The LiTe algorithm developed by a previous PhD candidate (Figure 6-1) describes the full data acquisition process required by a standard MPL system (Figure 3-18) to perform real-time measurements [34]. A modified version including a portion for diffusion was also developed, however based on experimental results this is not required for silicon [72], [73]. To obtain a full effective electron lifetime measurement (Figure 3-2 left) using MPL, the start requires measuring multiple phase shifts, at multiple frequencies, for each desired SSI (Figure 3-17).

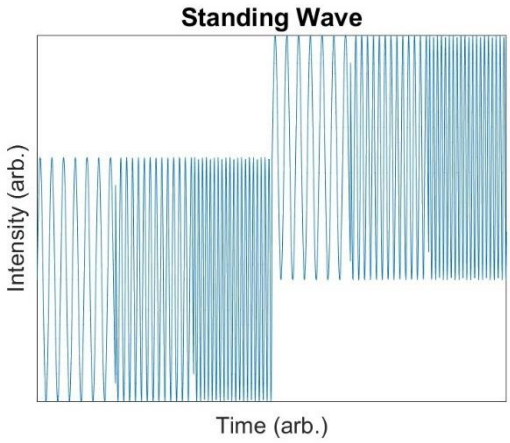

Figure 3-17: Traditional Input signal used within MPL.

At each SSI the measured phase shifts are fitted to Eq.3 to determine a differential lifetime value (τ_m).

$$\emptyset = -tan^{-1}(\omega\tau_m) \qquad \textit{Eq 3.4}$$
$$\tau_m = Modulated\ lifetime$$
$$\phi = Phase\ shift\ based\ on\ frequency$$
$$\omega = Frequency\ (radians)$$

As the differential lifetime is known to have a discrepancy to the actual lifetime a correction needs to be performed [74], [75]. A method for performing this known as d2a lifetime analysis allows the determination of actual carrier lifetime from differential measurements based on an iterative correction method (Eq.4) [76]. This does result in requiring neighbouring measurements of differential lifetimes for the correction to work.

$$\tau_{eff}(G) = \tau_m(G)\left(1 - G\frac{d\tau}{d\Delta n}|_{\Delta n}\right) \qquad \textit{Eq 3.5}$$
$$\tau_{eff} = Corrected\ lifetime$$
$$G = Generation\ rate$$
$$n = carrier\ concentration$$

MPL is comprised of a piece of software which sets the excitation frequency and records the calculated phase shift. The laser system applies an excitation frequency to a SSI after which the PL emission is collected by the collection optics and focused onto an InGaAs photodiode. Both the applied frequency to the laser and the measured signal from the InGaAs photodiode (Figure

3-16) are inputted into the lock-in amplifier which calculates the phase shift.

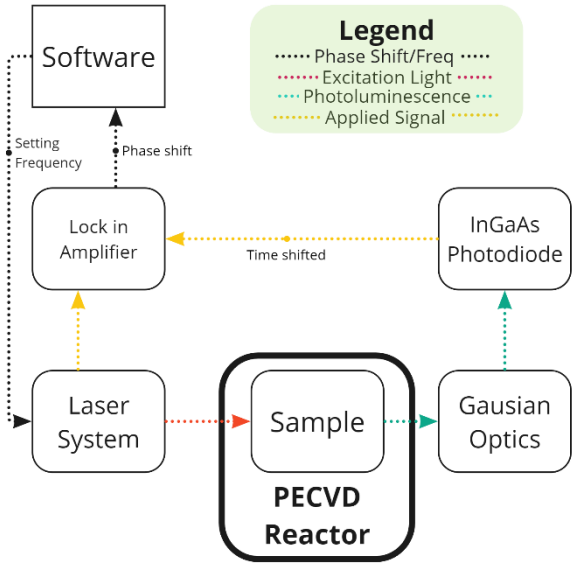

Figure 3-18: Standard MPL electronics design and previously installed on the PLASMAT reactor.

One of the key working principles is that the reference signal provided to the receiver for phase shift calculations is noise free. While not a pure necessity, it increases the accuracy and reduces the required acquisition period.

Given the usefulness of real time (*in-situ*) measurements the base requirement for performing them is, they must be fast. To improve the speed of MPL a change in the phase shift extraction methodology was required, involving improving the following three steps:

1. Multiple frequencies using standing waves (section 3.3.4)
2. Multiple static excitation intensities (3.3.5)
3. Long signal recording to extract a phase shift (section 3.3.6)

3.3.4 Frequency Sweep

When generating a standing wave using a digital to analog conversion device, the number of points per second used to define the wave must be stated. These points will all relate to an instantaneous frequency within the generated wave (Figure 3-19). In digital signal processing, a waveform can be represented as a series of discrete points generated at regular intervals in time.

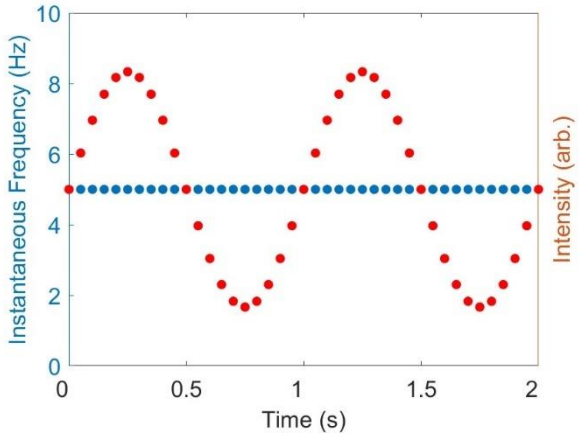

Figure 3-19: Depiction of the instantaneous frequency in relation to its standing wave.

By adjusting the amplitude (intensity) values at each point in time, the instantaneous frequency of the waveform can be modified, allowing for representation of different pieces of information for each point in time. A frequency sweep can thus be implemented by modifying the angular rotation of a standing wave giving a range from a core frequency.

Frequency modulation (FM) is a method of encoding information onto a carrier wave by modulating (varying) the frequency of the carrier wave according to the information being transmitted (Figure 3-20) [77]. In FM, the frequency of the carrier wave is varied in proportion to the magnitude of the information signal. FM is commonly used in radio communication systems, such as FM radio and television, as well as in various other applications, such as in microwave communication systems and in the control of electrical motors.

Frequency modulation and phase modulation are the two complementary principal methods of angle modulation; phase modulation is often used as an intermediate step to achieve frequency modulation. These methods contrast with amplitude modulation, in which the amplitude of the carrier wave varies, while the frequency and phase remain constant.

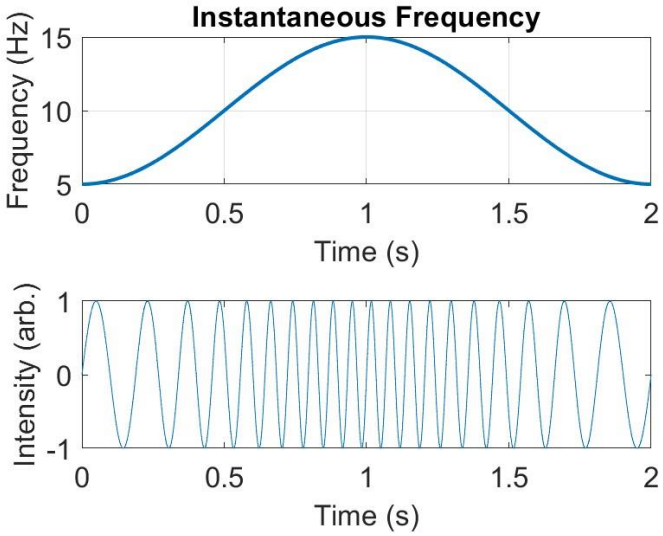

Figure 3-20: Example of a frequency sweep created using Eq.3.6 Top) the instantaneous frequency, Bottom) the waveform.

$$Singal(t) = A * \sin\left(2\pi\left(Ct - \frac{R*sin(2\pi ft)}{2\pi f}\right)\right) \qquad \text{Eq 3.6}$$

$$A = Ampltiude, C = Corefrequency\ (Hz)$$
$$R = Range\ (Hz), f = Sweep\ Frequency\ (Hz)$$

The measured phase shifts (Figure 3-21), using a frequency sweep from 100 to 700 Hz in duration from 2 to 10 s, with 2 s steps, each show the same values with all points being unique from their neighbours. The phase shift was extracted via performing a wavelet coherence transform in MATLAB with the standard settings provided. This solves the first MPL hurdle of slow phase shift measurements at a single excess carrier density. Such concepts have already been applied in impedance spectroscopy [78]. . The frequency range used was that which was previously used in the LiTe method [33].

The limitation of how fast a frequency sweep can be performed is directly related to the maximum acquisition rate capable. To continue reducing the signal period a data logger with a higher acquisition rate would be required.

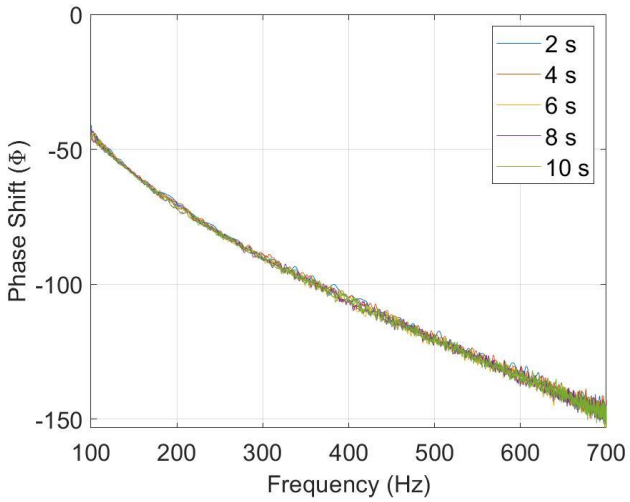

Figure 3-21: Measured phase shift using the signal described in Figure 3-20 showing the dissociation between points in time, for a frequency range of 100 to 700 Hz.

3.3.5 Carrier Density Modulation

The second improvement made was acquiring the phase shift across multiple excess carrier densities quickly. From this comes Dolphin's Wave, (Figure 3-22) where a frequency sweep is superimposed onto a low frequency standing wave. Due to each point in time being unique, phase shifts with a combination of frequencies and excess carrier densities are created. The amplitude units correspond to the laser driver input-modulation port when set at a laser strength of 150mA.

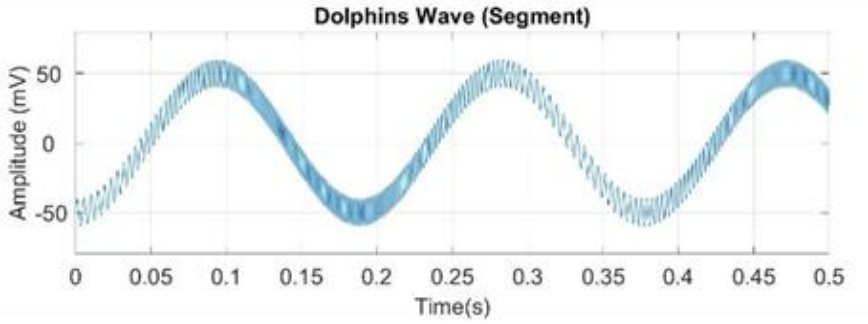

Figure 3-22: Dolphin's Wave constructed using a small amplitude frequency sweep (100 – 700 Hz at 3 Hz) superimposed onto a large amplitude (100 mV) low frequency (5.3 Hz) standing wave.

The principle of superposition states that for a linear system, the response (output) caused by two or more stimuli (inputs) is the sum of the responses

which would have been caused by each stimulus individually. To ensure this does not occur during the phase shift measurement, the base wave which is being used for the excess carrier density must induce no, or extremely minimal, hysterisis. Further testing is required to determine the impact with increasing the base wave frequency on the correction equation used to calculate τ_{eff} from τ_m

3.3.6 Phase Plane Mapping

Performing a wavelet coherence spectrum on Dolphin's wave using a coherence value of 1 (colour bar) shows the two frequency bands relating to the variation in excess carrier densities at 5.3 Hz and that of 100-700 Hz for the MPL phase shift measurement (Figure 3-23). The frequency bands are elongated as expected (Figure 3-12) however the values of coherence are all the same along this elongation thus it can be ignored. Observing the lower frequencies, the phase shift can be seen to be ~0° indicating 5.3 Hz being a low enough frequency when using a wave function for the modulation through excess carrier density states.

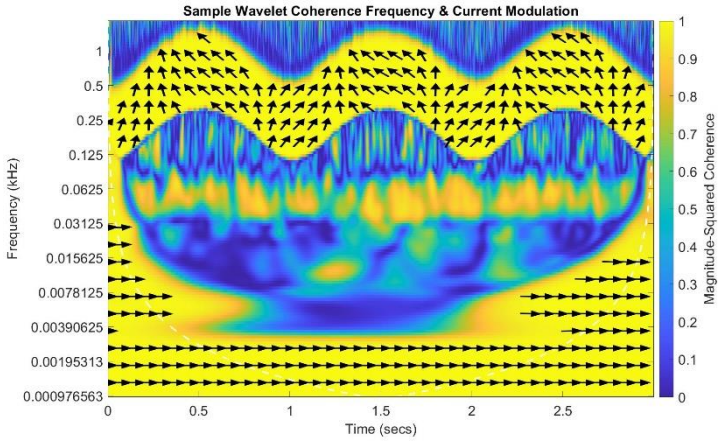

Figure 3-23: Wavelet coherence spectrum showing the phase shift between input and output wave of the system for the MPL frequency and excess carrier density variation.

After extracting the MPL phase shift, it can be lined up with the instantaneous frequency, and laser current input (excess carrier density) used for performing the measurement. Plotting frequency, laser current, and phase shift as their own axis, a plane using the phase shifts can be drawn (Figure 3-24).

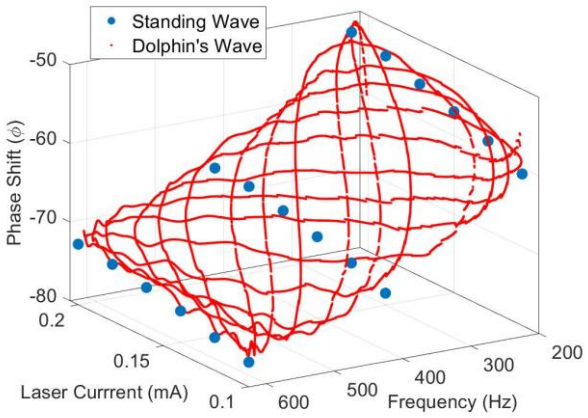

Figure 3-24: Comparison of standing & Dolphin's wave showing 18 phase shifts acquired in 40 s vs 60,000 phase shifts in 2 s

To ensure the methodology is correct, a comparison between a full measurement using the traditional standing waves (Figure 3-17) and Dolphin's Wave was performed (Figure 3-24). The pattern drawn is a Lissajous curve due to the construction of the wave using two rotational components in the frequency and light intensity components. The previous system (based on standing waves) required 40 s for eighteen phase shifts. In comparison, Dolphin's Wave measured 60,000 phase shifts in 2 s, which is based on the 30 kHz acquisition rate.

To apply Eq.4, bins at multiple laser intensities containing all the frequencies are taken (e.g., 0.15 mA ± 0.05). A comparison between the two methods is given in Figure 3-21 where 3 phase shift values (blue points) determined via using a lock-in amplifier (at 0.15 mA, measured in 7 s), to a snapshot of ~5000 phase shifts (red points) measured, at 0.15 ± 0.05 mA. A fitted line further shows that Dolphin's wave can be used to effectively measure the phase shifts using a binning method.

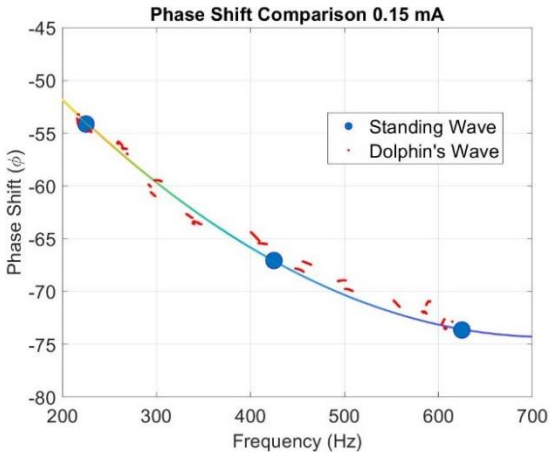

Figure 3-25: Comparison of standing & Dolphin's wave showing 3 phase shifts at 0.15 mA acquired in 7 s & ~ 5000 phase shifts at 0.15 mA ± 0.05.

Given a simplification in the phase extraction methodology a change in the LiTe processing steps is required (Figure 6-2). The intial section describing the signal generation and part of the calculations section is simplified and still compatible for joining the calculations for determining the lifetime based on diffusion within a sample.

3.3.7 Wavelet Comparison

To determine the optimal wavelet to be used for calculating the phase shift from the measured Dolphin's wave signals a comparison between 3 mother wavelets is performed: Morlet, Bump, and Morse (Figure 3-26). The Morlet and Morse wavelet's have a high degree of agreement between extracted phase shifts while Bump has certain areas which do not fully match. The disagreement is due to having a narrower variance in time and the wider frequency resulting in a reduction of noise in the phase shifts while the variance of Bump could be due to an inability to account for a piece of noise as overall there is good agreement.

Further work would involve changing the parameters set in the Generalized Morse Wavelet as the ones used were the standard settings provided by MATLAB, or further variations.

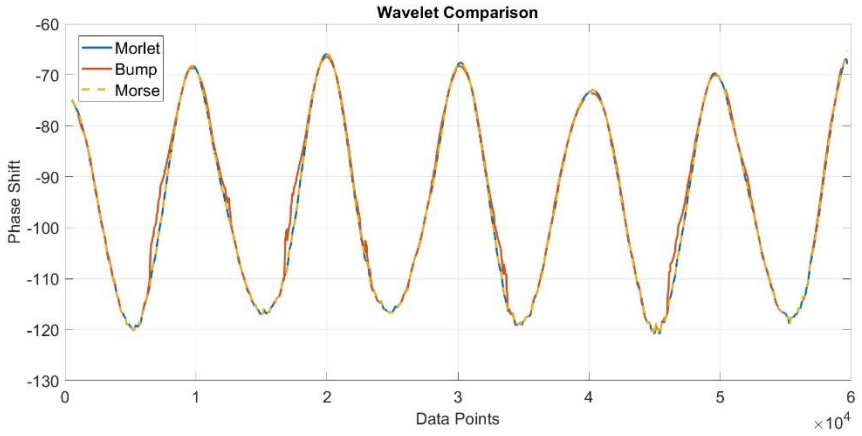

Figure 3-26: Comparison of the extracted phase shift using the wcoherence function within Matlab using three different types of wavelets. Acquisition rate at 30 kHz/s.

Other wavelets such as the Haar and Sym4 (Figure 3-4) wavelets are commonly used, however their characteristics make them unsuitable for this application due to their non sinusoidal shapes. Their uses focus more on compression, edge detection, and denoising.

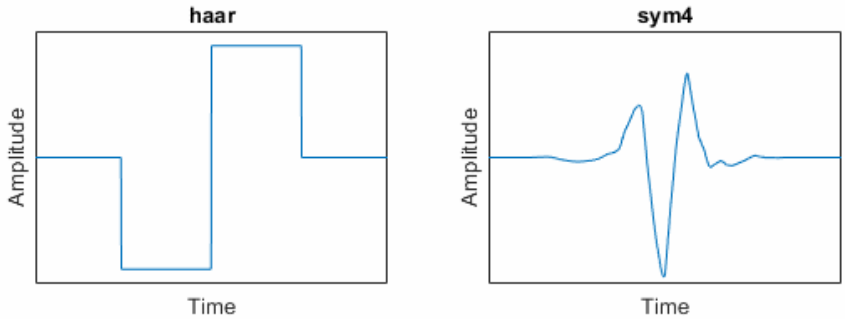

Figure 3-27 : Haar and Sym4 mother wavelets.

3.3.8 Speed & Repeatability

To demonstrate the effectiveness/stability of the newly proposed input wave a light soaking experiment was performed on an AlOx sample (Section 4.4) at room temperature. Figure 3-28 shows the τ_{eff} measured at room temperature on an as-deposited AlO_x sample. Surely during the measurement, the sample was light soaked by the 785 nm laser diode with an average power of 20 mW/cm^2. The continuous τ_{eff} measurement was performed for ~2.5 hours with the lifetime recorded every 2 seconds at an excess carrier density of 10^{15} cm^{-3}. The repeatability of the measurements can be seen due to the slow increase of τ_{eff}, allowing for many measurements to

be taken at a given value of τ_{eff} without significant deviation occurring, demonstrating the repeatability and accuracy of our method. The slight jumps/large bumps throughout the measurement are due to the internal clock for the data logger not starting at the same time for each measurement.

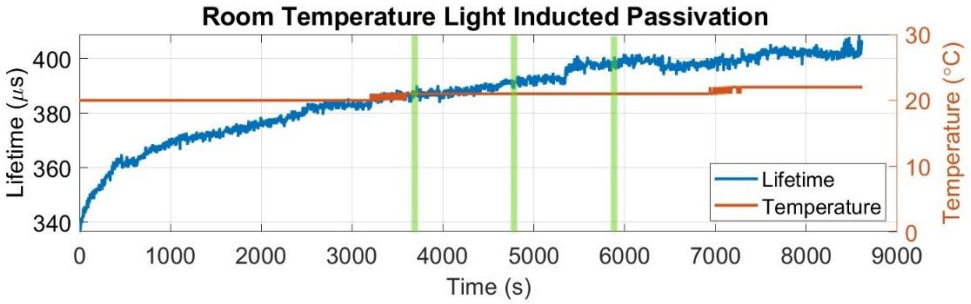

Figure 3-28: Light-soaking of an as deposited AlO_x sample at room temperature over a period of ~2.5 hours showing an increase of 60 µs with measurements every 2s.

A box plot, Figure 9, is used to provide a simple and easily interpretable representation of the central tendency, dispersion, and skewness. Three periods of 40 s intervals were chosen at 3750 s, 4810 s, and 5880 s to compare the reliability of the method. The interquartile range being ~3 µs allows for a clear trend to be determined over a small change in the lifetime value of a sample.

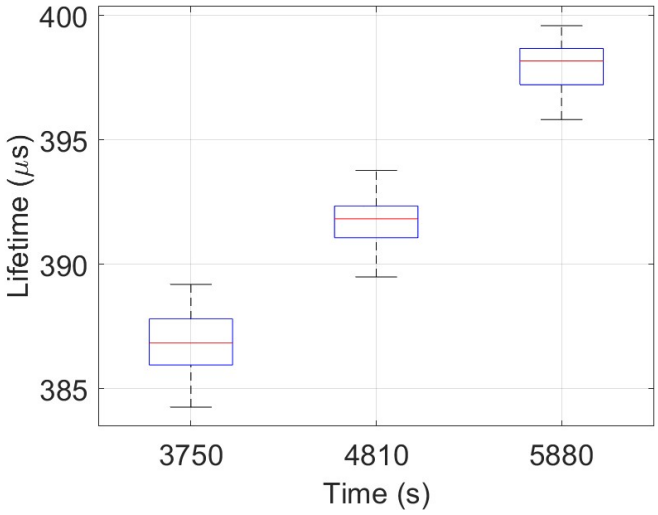

Figure 3-29: Box plots of 3 periods of 40 s highlighted in Figure 8 by yellow boxes.

The same test was performing fifty lifetime measurements on a sample with a steady lifetime (Figure 3-30). Each measured point has a box plot which indicates there is a small variation between measurements with only a few outlier measurements which occurred further showing the repeatability of the method.

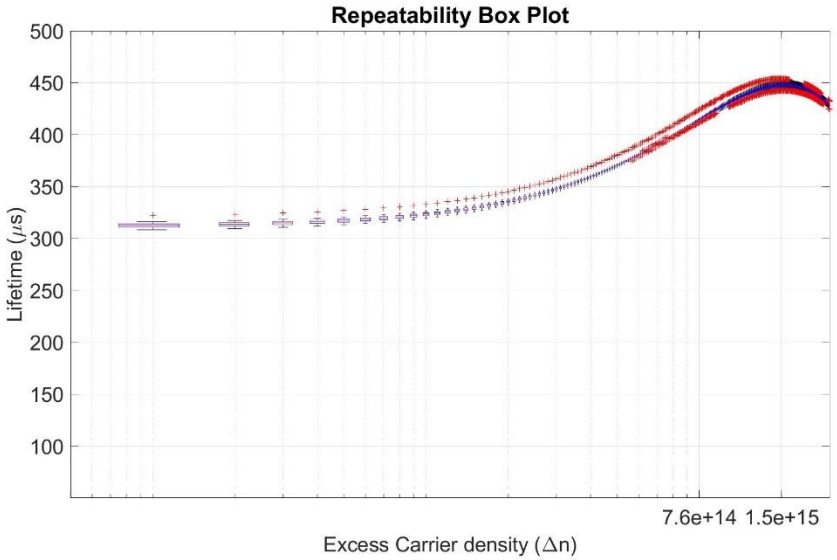

Figure 3-30: Repeatability using a box plot for Lifetime vs Excess Carrier density.

3.4 LIFETIME AT A STEADY SATE

Due to being in-situ, the sample is in a consistent rate of change thus the ideal measurement period would be as fast as possible without more than required, such as that stated in Figure 3-14. For a metric, one consistent light intensity with various known lifetimes has already been very successful in industry [59].

3.4.1 A brief introduction to zero

The concepts of zero and infinity are fundamental to many areas of mathematics and science, and they often appear together, representing the extreme ends of a spectrum of quantities. Understanding the behaviour of how they are applied within mathematical functions and processes as they approach these limits can reveal important insights.

As a seemingly simple and straightforward idea, it has played a pivotal role

in the development of knowledge. "Zero: The Biography of a Dangerous Idea" by Charles Seife explores the history and significance of zero in mathematics, philosophy, and other fields [79]. However, while the book provides a comprehensive account of the historical and philosophical aspects of zero, there is still much to be explored in terms of its scientific applications.

3.4.2 Methodology

The reasoning of MPL is to solve the initial problem statement of (Figure 3-14) determining the lifetime of a SSI, without overlap. When viewed in terms of a frequency this can be treated at 0 Hz.

A wave can be understood from a unit circle by examining the projection of a rotating point onto the vertical axis of a perpendicular plane (Figure 3-31). Consider a unit circle with its centre at the origin of a coordinate system. Imagine that a point is rotating uniformly around the circumference of the circle in a clockwise direction. As the point rotates, it is projected onto the vertical of the perpendicular axis coordinate system and traces out a path that oscillates up and down, creating a wave. It is the changing of this angular rotation which is used for creating a frequency sweep.

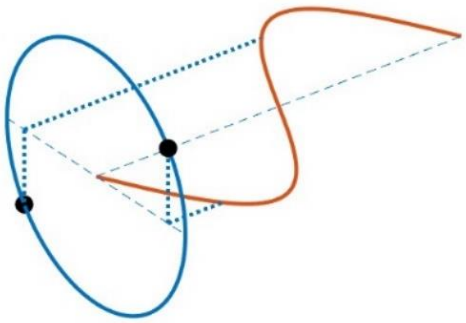

Figure 3-31: Creating a sinewave from the clockwise rotation of a circle.

The direction of rotation of a point on the circle determines the direction of the resulting wave (Figure 3-32). Clockwise considered being positive and counterclockwise negative. However, when there is no angular rotation, and a point is still projected onto the coordinate system a straight line will be traced out representing 0 Hz.

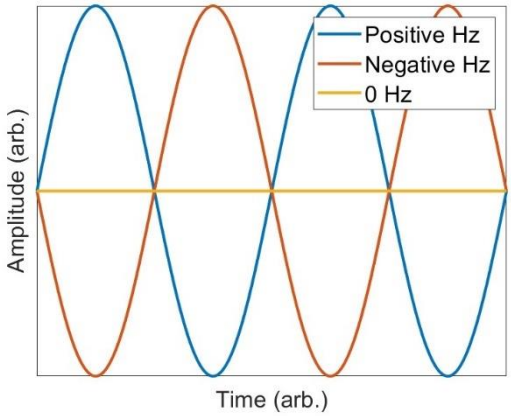

Figure 3-32: Comparing 3 angular velocities of the rotating circle in Figure 3-31, positive, negative, zero.

Eq.3.4 describes the τ_m first must be modified to allow the negative frequency range to result in a negative phase shift with the addition of an absolute function (Figure 3-33). This reveals a point at 0,0 which is where to look.

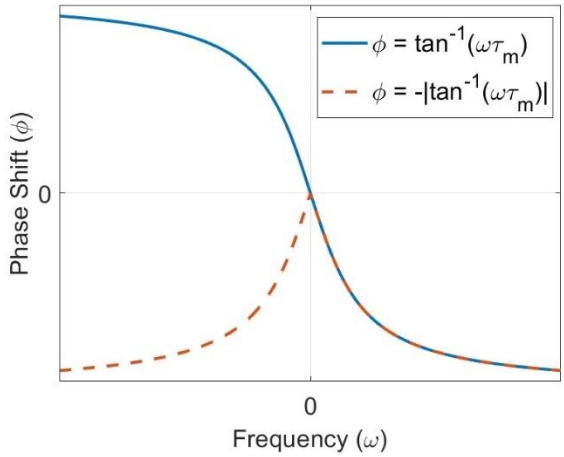

Figure 3-33: Visualisation of the original Eq.2 (blue) and a modification (red).

The equation states that at 0Hz there is no phase shift which means there would be no lifetime (Figure 3-33). Thus, the discrepancy between τ_{dif} and τ_{eff} could be attributed to the initial assumption of the phase shift following a tan function to be an approximation. This creates the point at which there is a difference between the initial goal of lifetime at a SSI (Figure 3-16 left) and what is being used to achieve it (Figure 3-34).

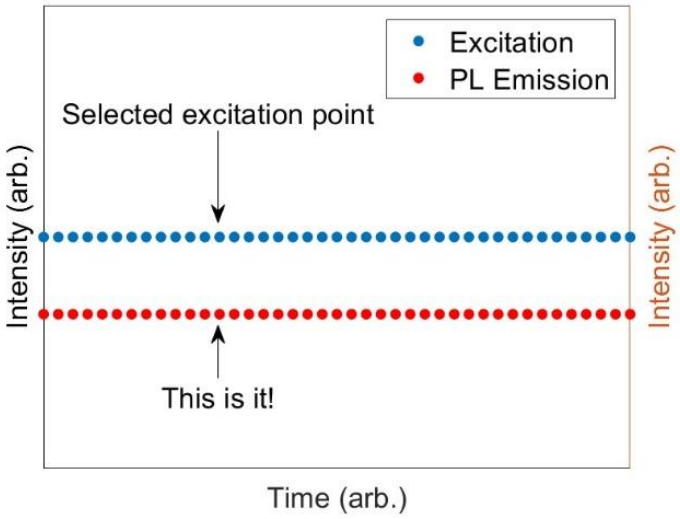

Figure 3-34: The assumption of Eq.2 assumes at 0Hz.

As using a frequency sweep allows for a singular point for each frequency to be measured, a sweep going through 0 Hz is used. This allows for τ_{eff} to be present within the measurement for a singular moment fulfilling the requirement of zero.

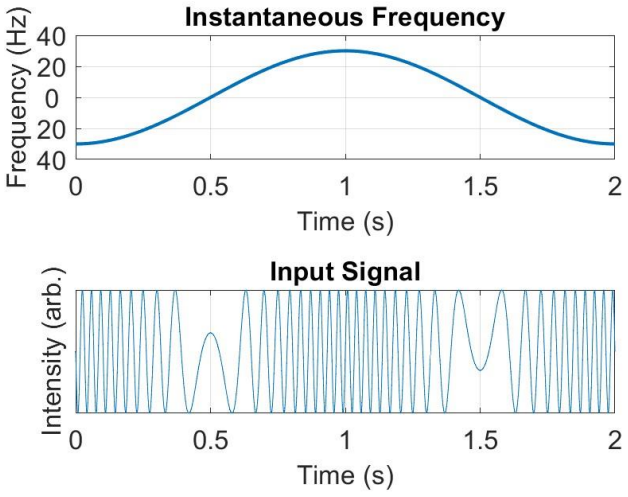

Figure 3-35: Instantaneous frequency of a wave designed to go through 0Hz dynamically.

Using a frequency sweep from 400 Hz to -400 Hz at 4 Hz the resulting wavelet coherence transform shows a repetition of the phase shift after passing through 0Hz dynamically (Figure 3-36) indicating the assumptions made

regarding the direction of rotation is correct. It shows that at 0 Hz there is a piece of information which can be found which relates to a SSI lifetime; however, a methodology which uses frequencies and phase shifts is not suitable. Due to the low temporal resolution of wavelets at low frequencies, it is difficult to extract anything at low frequency. At 0 Hz it is impossible to extract a phase shift simple based on how wavelet theory operates for a phase shift extraction.

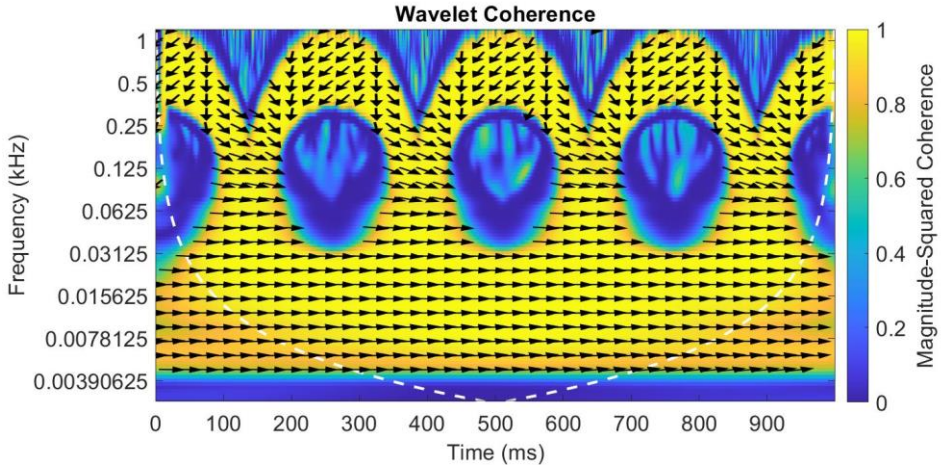

Figure 3-36: Wavelet coherence transform of the signal constructed from Figure 3-35.

To overcome the issue of 0 Hz a Gaussian envelope is used with a focused frequency bandwidth around 0 Hz resulting in a Gaussian as it would be focusing on a flat area. A Gaussian envelope is a localized bundle of waves that can be described by a wave function (Figure 3-37 yellow line). One can be made by multiplying a wave by a Gaussian function which acts as a filter that modulates the amplitude of the wave, creating a region of high amplitude around a central point and gradually decreasing to zero as the distance from that point increases, creating a frequency pulse.

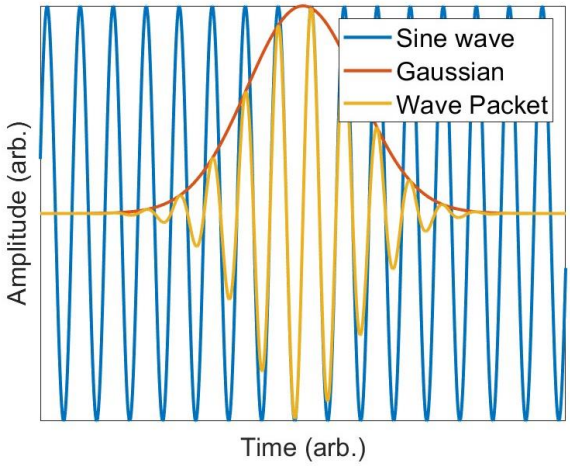

Figure 3-37: A wave packet made by multiplying a wave function with a Gaussian to create a locally defined Gaussian envelope.

Inputting the Gaussian through the system requires it to be exceedingly small to keep within the quasi-steady state regime and ensure no hysteresis. The resulting PL emission is a copy of the input which is a representation of the SSI lifetime (Figure 3-38, left). To calculate τ_{eff}, it requires a horizontal shift in time to overlap the two peaks. To construct a full lifetime spectrum a series of steps with peaks would be required (Figure 3-38 right), indicating the small size of the pulses in comparison to the total signal size. This is the function for the methodology.

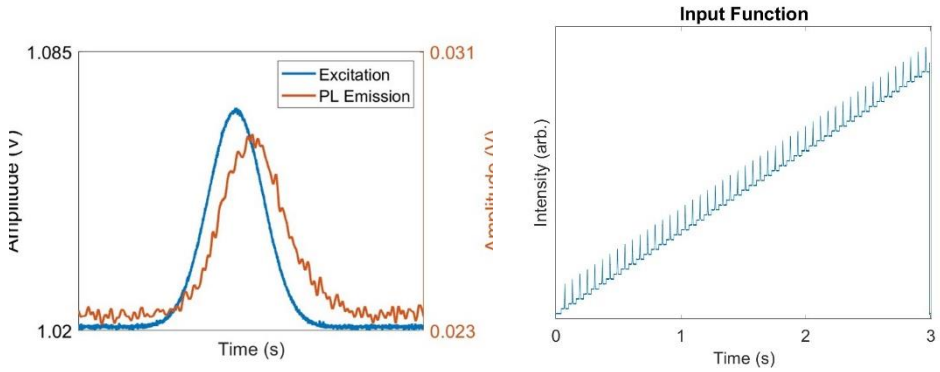

Figure 3-38: Left) Gaussian bump displayed with input (red) and output (blue) signals represented by Gaussian to measure a single lifetime value. Right) A series of fifty pulses used for the measurements in Figure 3-39.

Too ensure the validity of the method a comparison with the WCT-120 Sinton was performed (Figure 3-39). Using an a-Si:H, and AlOx passivated silicon wafers, the results show good agreement between using a Gaussian and a

WCT-120. Due to the physical limitations of the developed device (Figure 3-40), the lower the lifetime becomes the harder it will be to resolve with a higher accuracy. The deviation seen in the AlOx sample is due to the lifetime being small enough the slight difference in starting the simultaneous acquisition of the excitation and PL emission signals within the data logger is noticeable. This can be overcome by increasing the acquisition rate of the data logger being used, as the DT9847 has a 5 µs resolution which is not great when attempting to measure 100 µs.

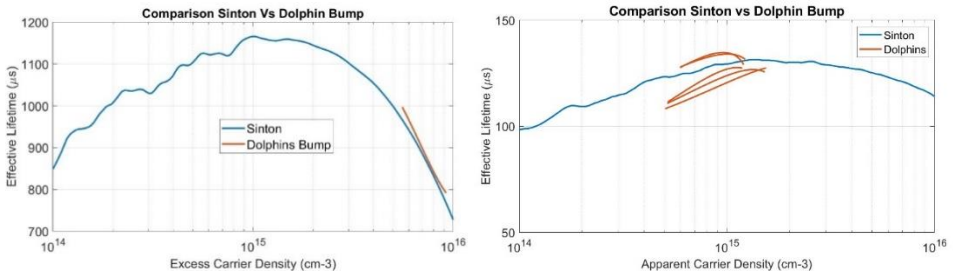

Figure 3-39: Comparison of an electron lifetime measured using a Gaussian bump and a WCT-120 Sinton Left) a-Si:H Right) AlO_x with multiple measurements showing internal clock tolerances of the data logger

Given the previous process diagrams, a further simplification can be performed via replacing excitation function and removing the need for a correction equation (Figure 6-3).

3.5 SCHEMATICS

To be capable of using Dolphin's wave, the lock-in amplifier being previously used was changed for a combined function generator / data logger (Figure
r driver
citation
l signal
r driver
l by the
llowing
of 216

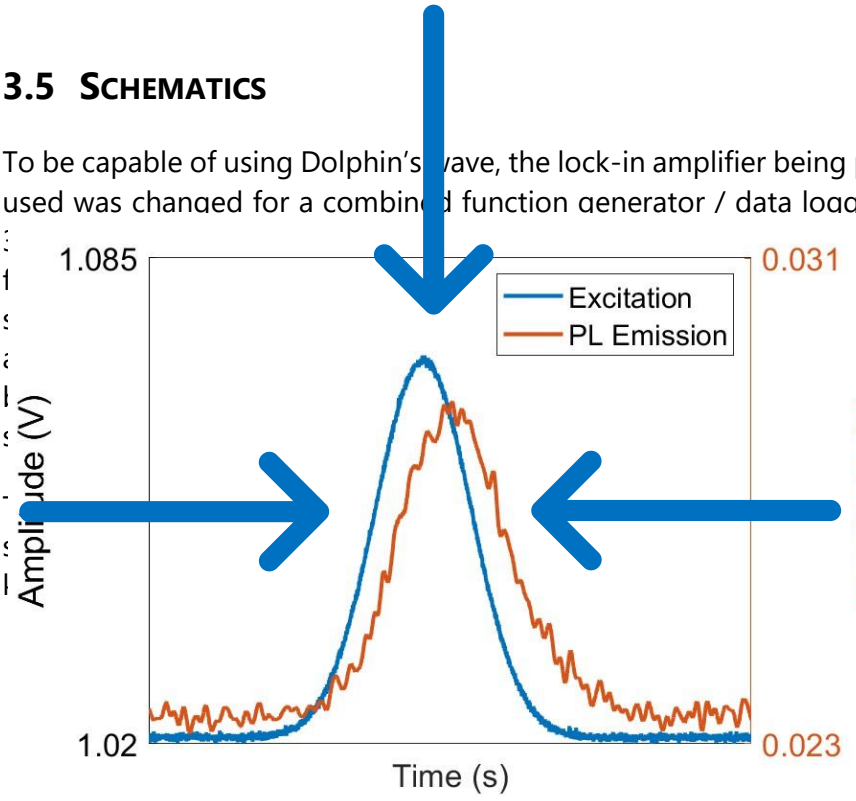

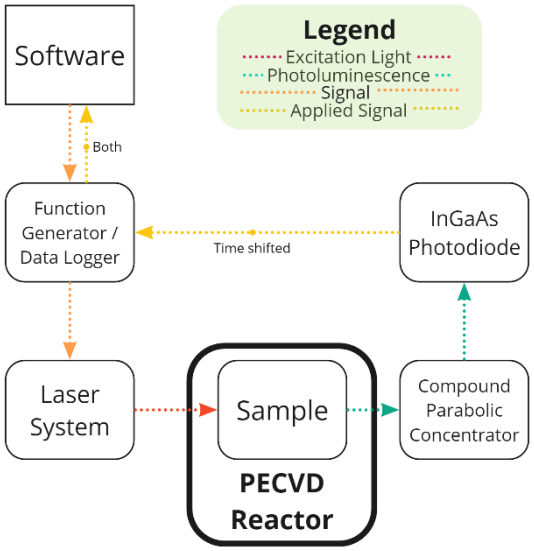

Figure 3-40: Diagram depicting the modulated photoluminescence setup & photoluminescence setup using a portion of the newly developed optics, Figure 2-21.

To perform in-situ τ_{eff} and in-situ PL a spectrometer is added and connected to the software as a standalone addition (Figure 3-41). The optics are seen in Figure 2-21.

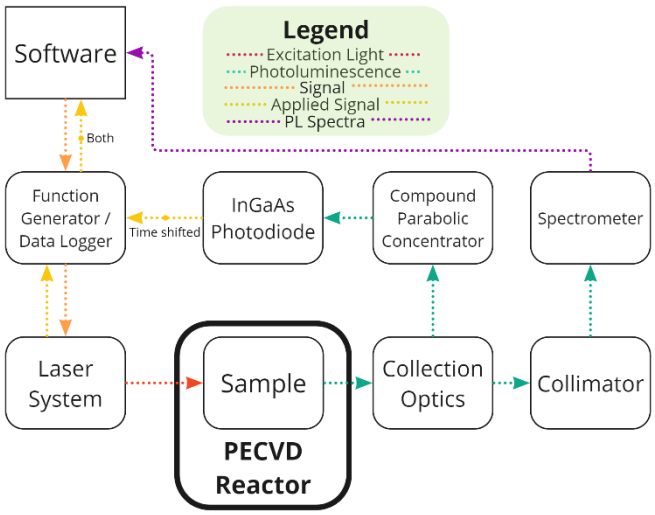

Figure 3-41: Hardware setup used for performing in-situ τ_{eff} and in-situ PL.

3.6 CHAPTER REVIEW

Two main novelties have been introduced in this chapter, the decrease of measurement time required for MPL and the introduction of a new technique to measure τ_{eff}.

- The measurement time for MPL was decreased from 40 s during the PhD of Menkoing Sreng down to 2 s via changing from a standing wave to a frequency sweep superimposed onto a wave changing the excess carrier density. Phase shift extraction was switched from a lock-in amplifier to wavelets which allows for a dynamic phase shift extraction allowing the Dolphins' wave to be used. This resulted in the application of a patent.
- A simplified method for performing a direct lifetime measurement was created involving measuring the period between two Gaussian pulses. This also resulted in the application of a patent.

4 IN-SITU LIFETIME APPLIED TO ALD-ALO$_X$

The purpose of this chapter is to demonstrate the applicability of the improved theory and hardware to study the effects of annealing and plasma processes on the effective carrier's lifetime. The efficiency of a crystalline solar cell is highly dependent on the performance of the surface passivation layers. Our objective is to use in-situ carrier lifetime measurements to gain the understanding on the passivation processes via the measurements of the evolution of the τ_{eff} in silicon wafer during annealing, deposition, and hydrogenation, for which real-time MPL measurements have been shown to be a very effective method [32]–[34], [73]. Figure 4.1 shows a schematic of the simplified structure of the samples studied in this chapter.

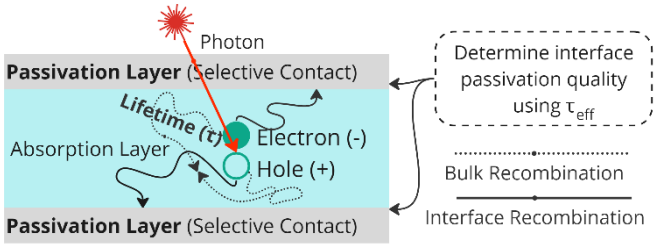

Figure 4-1: Illustration of bulk and interface recombination.

4.1 AMORPHOUS ALUMINIUM OXIDE

Aluminium oxide (AlO_x) is an integral part for the fabrication of current PERC & TOPCon cells. Searching 'ALD-AlOx for Silicon passivation' using google scholar, the number of publications per year can be found (Figure 4-2). Starting from 2006 the number of publications about ALD-AlO_x passivation increased dramatically after Hoex et al [80] showed its excellent ability for reduction of n-type and p-type Si effective surface recombination velocities. It made AlOx a very successful ALD material in silicon photovoltaics [81]. The first study of surface passivation properties using AlO_x on silicon was published in 1989 using atmospheric pressure chemical vapor deposition [82].

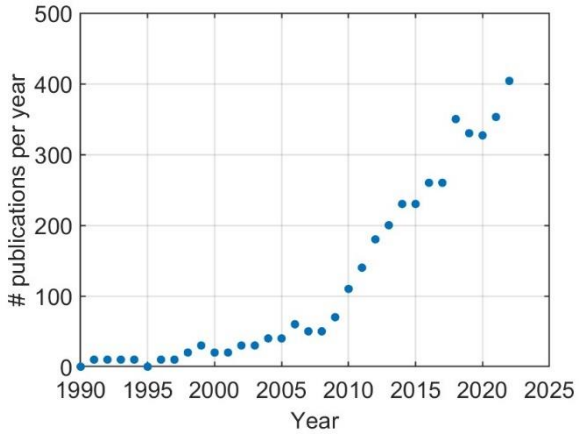

Figure 4-2: Number of publications per year obtained for 'ALD-AlO_x for Silicon passivation' google scholar search request.

Currently ALD-AlO_x deposition systems have the highest throughput of all the available tools used at 10,000 wafer/h (Figure 4-3). PECVD-AlO_x is however improving currently at the same rate creating competition for the ALD alternative and vice-versa. [26]

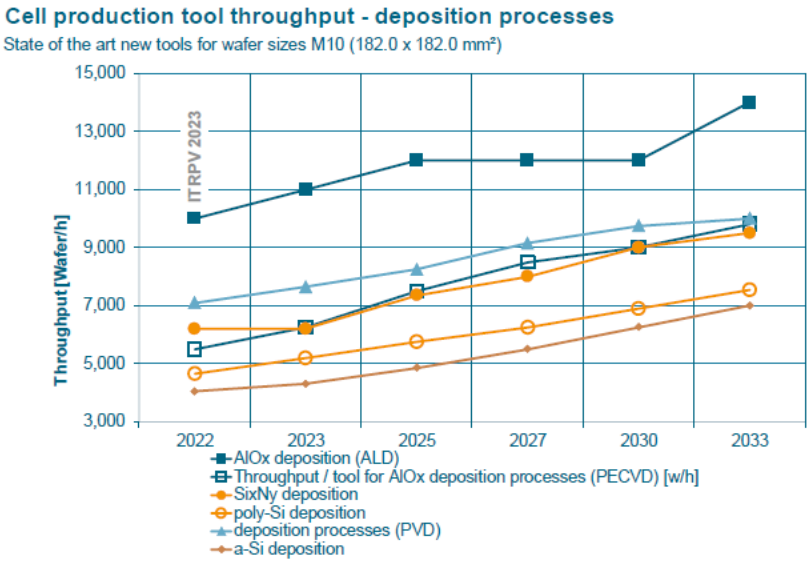

Figure 4-3: Cell production tool throughput – deposition throughput for state-of-the-art M10 wafer sizes [26].

According to The International Technology Roadmap for Photovoltaic (ITRPV), within n-type TOPCon production, direct plasma PECVD will dominate most of the market in 2033 while ALD technologies will be stagnant (Figure 4-4). This would indicate there is a technological breakthrough waiting to occur in either one. Within the current p-type PERC architecture,

ALD and direct plasma PECVD are growing at remote plasma PECVD's expense. [26]

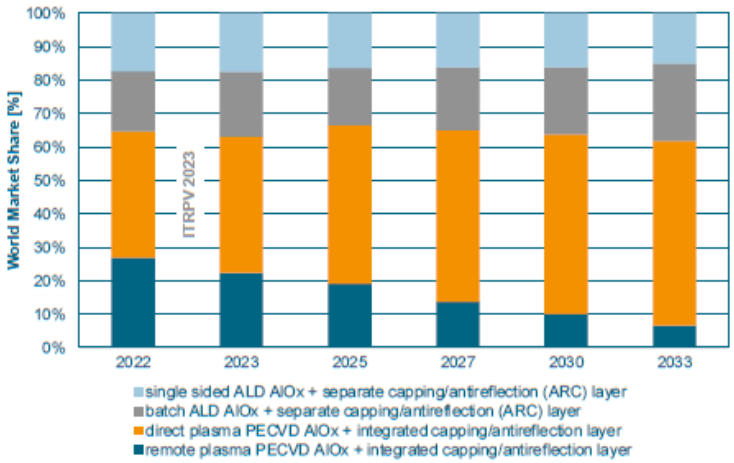

Figure 4-4: Front side passivation technologies for n-type TOPCon [26].

4.1.1 Passivation Qualities

Surface passivation can be achieved through a combination of chemical passivation and field-effect passivation, enabled by chemical bonding (Si-O, Si-H) at the interface and negative or positive charges situated near the semiconductor-oxide interface respectively (Figure 4-5) [67], [81]. AlO_x films provide weak passivation in their as-deposited state requiring annealing to activate the formation of i) a high density of negative or positive fixed charges which improves the field effect passivation and ii) the formation of a SiO_x interfacial layer for chemical passivation [67], [83]–[85]. The presence of a silicon oxide (SiO_x) interlayer at the Si/AlO_x interface is crucial for saturating dangling bonds and generating charges [86], [87]. Theoretical studies have identified point defects in the bulk of AlO_x as the source of negatively charged traps [88], [89]. Point defects, such as aluminum and oxygen vacancies (V_a and V_o), interstitials (Al_i and O_i), and dangling bonds (Al_{DB} and O_{DB}), introduce acceptor-like or donor-like defect levels that can either trap or transport charges depending on the density of defects, the position of the Fermi level, and the position of the defect levels relative to the band edges [89]. Defects that are preferentially located near the O-rich SiO_x/AlO_x interface, such as V_a, O_i, and O_{DB}, can trap electrons in deep acceptor-like levels near the AlO_x valence band, acting as fixed negative charge centers [89], [90]. Additionally, the negatively charged tetrahedral AlO_4, which is dominant near the SiO_x/AlO_x interface [86], is likely responsible for the fixed negative charge. Recent experimental studies have demonstrated that the charging of traps near the SiO_x/AlO_x interface is significant in generating

negative charge [91], [92]. Positive fixed charge in AlO_x achieved via illumination during annealing is a new phenomenon which has only been recently reported, adding to a large list of passivating processes [67].

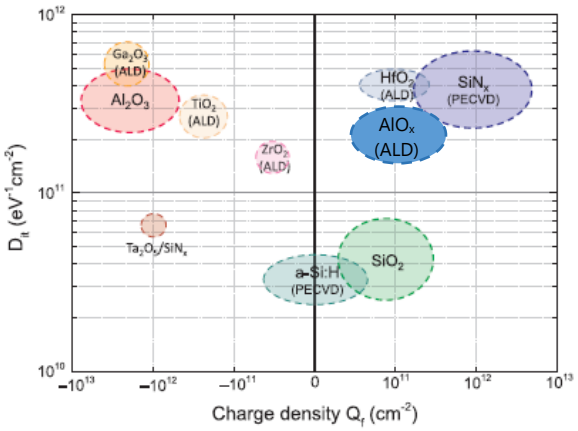

Figure 4-5: An overview of the fixed charge density and interface defect density of typical passivating materials for c-Si surfaces [93] with 'AlO_x (ALD)' added in based on where it is mentioned [67].

The samples which were used throughout the following sections consist of a FZ c-Si n-type wafers (280 µm, 1-5 Ω cm^{-1}, from TOPSIL) pre-treated with 30 s 5 % HF dip to remove native oxide layer, then coated with 90 cycles, unless stated otherwise, of AlO_x layer deposited via thermal Atomic Layer Deposition in the Picosun R200 Advanced system at 150°C using TMA and H_2O as precursors.

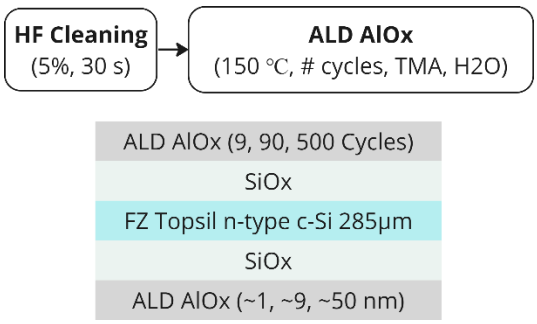

Figure 4-6: ALD AlO_x coated c-Si wafer stack sample schematic.

4.1.2 Atomic Layer Deposition

Atomic layer deposition (ALD) is a versatile method used to deposit high-quality thin films with exceptional control over thickness, composition, conformality and interface properties. The process of ALD involves self-

limiting surface reactions that are precisely controlled by alternating pulses of gaseous precursors, with a purge cycle between (Figure 4-7), as the precursor molecules react with the surface within a set deposition temperature window.

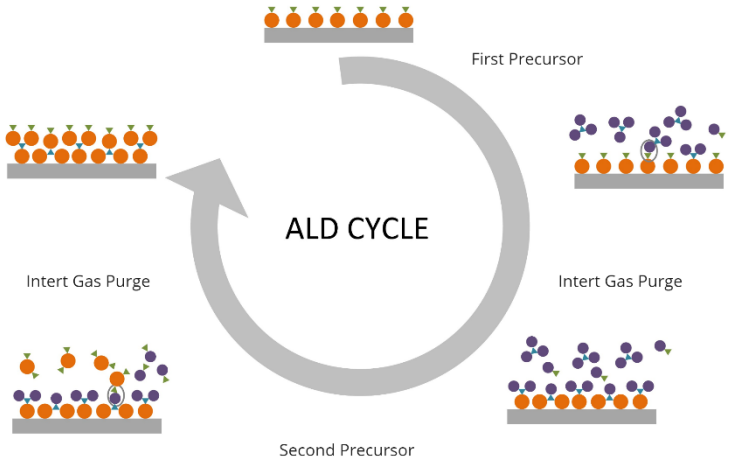

Figure 4-7: General ALD deposition process.

The benefits of the ALD process over other thin-film deposition techniques, such as chemical vapor deposition (CVD) and physical vapor deposition (PVD), are that the films produced by ALD are highly conformal and the process is highly controllable and repeatable. It is also widely used in the semiconductor industry.

4.2 Surface Passivation

Surface passivation is a crucial process which aims to reduce surface recombination velocity (SRV) and enhance the performance of electronic devices. Surface recombination occurs when electrons or holes recombine at the surface instead of contributing to the device's output, thereby limiting its efficiency. Passivation is performed through the formation of a thin layer on the surface. The layer can be formed by a variety of techniques, including thermal oxidation, chemical passivation, or deposition of thin films. The passivation layer can be composed of amorphous dielectric materials, such as silicon oxide (SiO_x), silicon nitride (SiN_x), or aluminum oxide (AlO_x), among others. Surface passivation can be achieved via two mechanisms as detailed below.

4.2.1 Chemical Passivation

Chemical passivation involves the use of chemical reactions to reduce the

density of surface states and eliminate surface dangling bonds. The passivating layer reduces the density of defects at the interface in turn reducing the number of recombination sites. ALD AlO_x chemical passivation results in the formation of a thin silicon oxide (SiO_x) layer at the AlO_x/c-Si interface during annealing, resulting in a notable reduction in the surface defect density (Figure 4-5). It is important to note that ALD - AlO_x contains a significant amount of hydrogen (also PECVD – ALD) in the bulk depending on its deposition temperature (Figure 4-8). Increasing the deposition temperature leads to the reduction of hydrogen concentration due to the improved reactivity between gas precursors and surface species. [94], [95]. Our films being deposited at 150 °C, we expect them to contain about 5-6% of hydrogen.

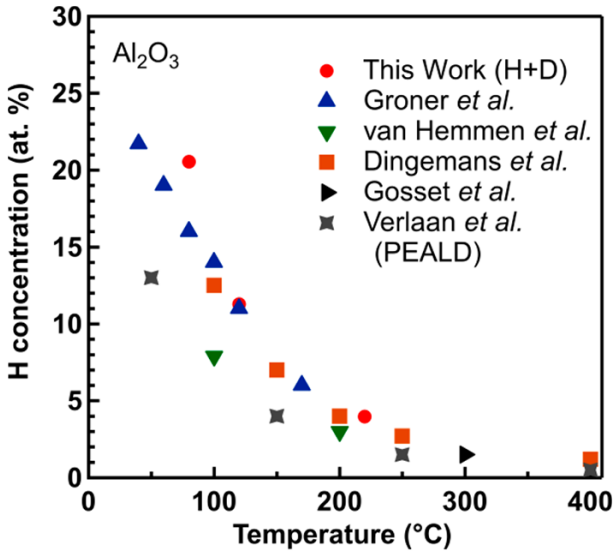

Figure 4-8: Hydrogen concentration in thermal and plasma enhanced ALD AlO_x films at different deposition temperatures [94].

4.2.2 Field Effect Passivation

A second method for reducing the surface recombination is using an electric field to selectively repel carriers and therefore limit recombination (Figure 4-9). Dielectric thin films result in field effect passivation which comes from fixed electrostatic charges at the interface which increases τ_{eff}.

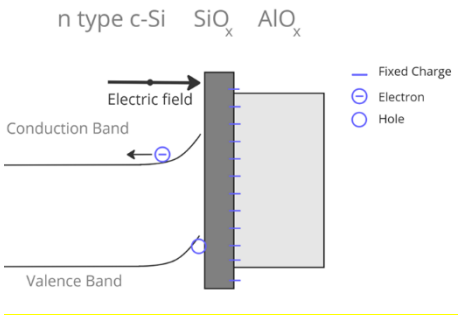

Figure 4-9: Cross sectional view showing where the negative interfacial trapped charges are and the electric field within a negative field effect passivation AlO_x layer.

The electrically active defects within such a system can be subcategorized as follows (Figure 4-10) [96], [97]:

- Interface trapped charges (Q_{it}), which are located at the interface between the insulator and the semiconductor. They can be positive or negative in nature, induced by oxidation processes, structural defects, or impurities. Furthermore, they can be caused by radiation or other bond-breaking processes.
- Fixed charges (Q_f), which are located near the oxide interface. They are negative (in the case of AlO_x) and related to the oxidation process, oxidation temperature and silicon orientation. They are not electrically connected with the Si substrate.
- Oxide trapped charge (Q_{ot}), which is a charge trapped in the oxide that can either be positive or negative (holes or electrons). It is caused by ionizing radiation, tunnelling, or other mechanisms.

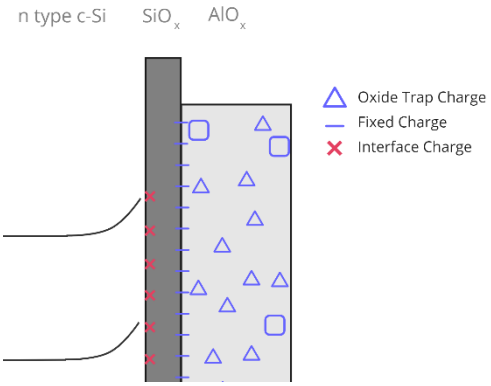

Figure 4-10: The 5 different types of traps and charges in an AlO_x/Si system.

4.3 ANNEALING PROCESS

The annealing profile, which displays the temperature changes during the time of the annealing process, is crucial to optimize for achieving the maximum τ_{eff}. By fine-tuning the annealing profile, the electrical and optical properties of silicon cells can be enhanced, leading to increased efficiency and overall performance. The annealing process can modify the microstructure (SiO_x interface, Q_{it}, Q_f) of passivation layers, thus affecting their properties. Finally, from an economic perspective, the thermal budget has a direct influence on the final production cost of the solar cells. Using in-situ τ_{eff} variations specifics of the traditional heating profiles can be readily examined. As the temperature rises, the band-gap energy of semiconductors tends to decrease because of thermal energy on the atomic structure of the material. It is impacted by electron phonon interactions and lattice expansion [93]. In addition, the number of charge carriers in a semiconductor increases as more carriers attain the energy needed to surpass the band-gap threshold, resulting in an increase in the conductivity of semiconductors with rising temperature. The reported variation of minority carrier lifetime in c-Si wafers as a function of temperature is believed to be due to changes in the thermal velocity of free carriers and variations in the capture cross-section for electrons and holes [91]. Polycrystalline cells exhibit an exponential increase in minority carrier lifetime with increasing temperature, which is thought to be attributed to the presence of recombination barriers on the surface [92].

4.3.1 Profile Variation 1

Although AlO_x has demonstrated exceptional surface passivation on silicon surfaces, the passivation mechanism of this layer and the impact of the post-deposition anneal on the AlO_x/Si interface properties are not yet fully comprehended. A significant improvement in surface passivation is observed following a post-deposition anneal which is mandatory to increase the ALD-AlO_x negative, or positive, fixed charge and reduce the interface defect density. The annealing process can be optimized by adjusting the process temperature, process time, and the type of gas, in which annealing is performed. Various methods can be used to perform thermal annealing, such as standard furnace annealing (the most common), rapid thermal processing (RTP) with infra-red (IR) lamps, flash lamps, laser scanning or sub µs laser, each requiring a lower duration due to higher temperatures being achieved faster [98]. As the annealing time decreases the thermal budget decreases, with increasing temperature, and selectivity increases making it desirable to

understand what is happening in such a short time span.

A typical heating profile, using furnace annealing, (Figure 4-11) reaches a specific temperature and remains constant for a period of time before cooling down after which a measurement can take place and the optimum annealing temperature is determined [99]. However, a key challenge associated with this is the inability to accurately determine the optimal annealing time required for a given temperature, as well as the physio-chemical processes and associated mechanisms which occur through a faster method.

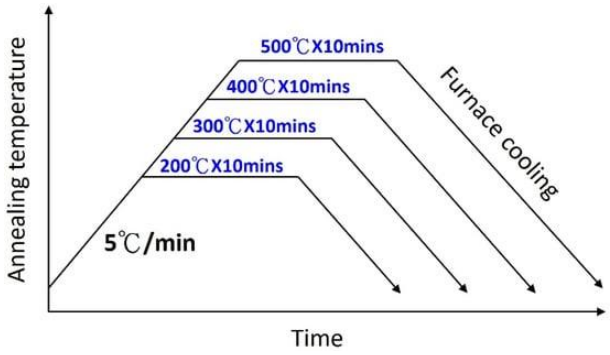

Figure 4-11: Example experiment showing heating curves of different annealing processes [99].

An investigation was conducted using a 9 nm ALD AlOx layer to determine the disparity in energy required to achieve equivalent τ_{eff} values under two different temperature profiles (Figure 4-12). While both the substrate holder and the RF electrode are always heated at the same temperature, only the substrate holder temperature is mentioned. Annealing was performed under a hydrogen flow rate of 50 sccm and a pressure of 1 Torr.

1. Heating to 225°C followed by maintaining a constant temperature until the τ_{eff} reached a plateau, and subsequently heating to 300°C to assess the possibility of τ_{eff} gains.
2. Heating to 300°C, followed by cooling to room temperature.

During both temperature ramps, at ~220°C, a clear change in the τ_{eff} gradient can be seen. This could be attributed to the continued formation of the SiO_x as the AlO_x deposition temperature was 150°C [67]. After maintaining a constant 225°C (Figure 4-12 left) or the τ_{eff} reached a plateau, a short pulse to 300°C was performed to check if a higher τ_{eff} could be reached; however only a small bump can be seen, indicating that most of the reactions for improvement had already occurred. In contrast, when performing heating to 300°C, followed by cooling (Figure 4-12 right) the same lifetime can be

reached in a much shorter period.

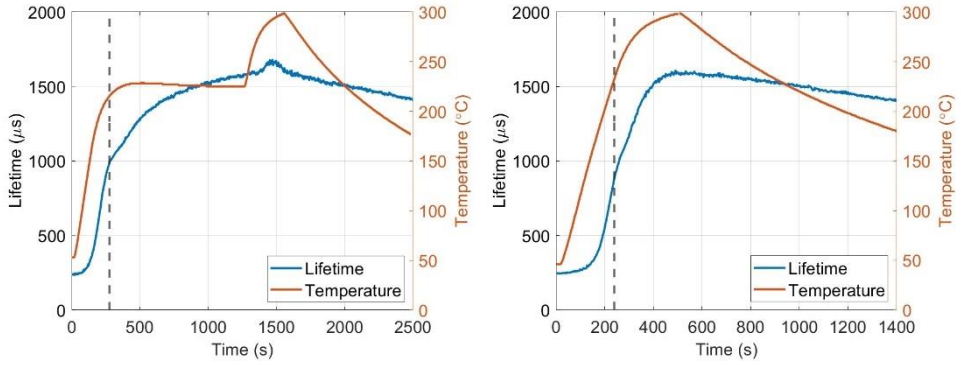

Figure 4-12: Left) Annealing profile one and τ_{eff}. Right) Annealing profile two and τ_{eff}.

Given that the enhancement in passivation efficiency resulting from heating is primarily attributed to further formation of the SiOx layer and fixed charge generation, it can be inferred that prolonged heating at 225°C can deliver an equivalent level of thermal energy as that achieved by heating to an instantaneous peak temperature of 300°C. Considering the thermal budget, the reduced time requirements for annealing make the peak temperature approach particularly appealing for industrial applications. Therefore, further investigation into the determination of the optimal lifetime measurement for a peak annealing temperature is suggested or a combination between the two annealing profiles depending on the layer stack as PV cells have multiple layers.

4.3.2 Profile Variation 2

Peak annealing profiles do not allow a system, such as the samples being used, to reach a steady state in comparison to a plateau profile. Given this a multipeak annealing profile should be useful to determine the optimum annealing temperature of a sample. Using a 1 nm and 9 nm ALD AlO_x coated samples repeated heating and partial cooling to multiple subsequent increasing temperatures (Figure 4-13) after which the 1 nm was compared to samples which were only heated to the last three temperatures.

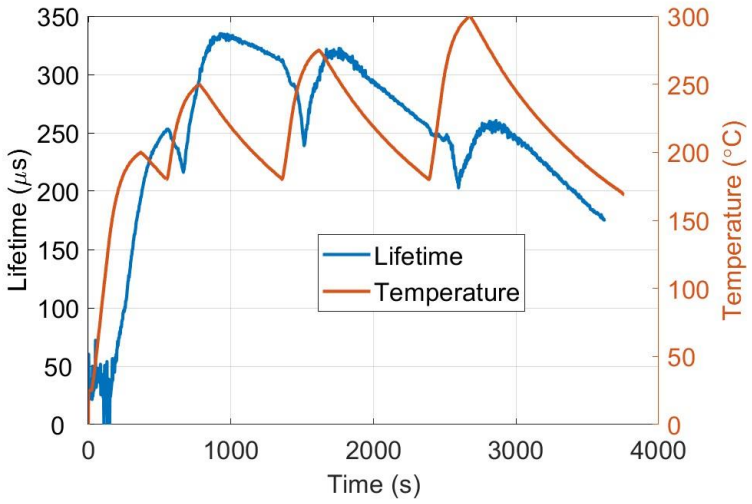

Figure 4-13: 1 nm ALD AlO_x heated to 200°C, 250°C, 275°C, and 300°C with partial cooling in between each temperature.

After heating to an initial temperature of 200°C and partially cooling the τ_{eff} continues to increase during the cooling phase. However, when heating to the next temperature an initial decrease in τ_{eff} occurs before increasing when closer to the temperature peak of the following peak annealing temperature. Afterwards, the τ_{eff} continues to improve for a short period of time before decreasing. This behaviour is seen for all peak temperatures which had another peak in temperature preceded them, with the maximum τ_{eff} occurring at 250°C which could potentially be slightly lower but not lower than 200°C. Comparing the multiple temperature peak sample with a single peak temperature samples (Figure 4-14, Figure 6-6) the important part to note is the similarity in the cooling τ_{eff} matching one another showing the same lifetime has been achieved (Figure 4-14 1000 s onwards). The τ_{eff} during the heating stage do not match, with there being an initial decrease in the lifetime value during heating, reason unknown, and a delay in the increase of lifetime of the multistep sample after there has been a previous annealing peak. This could be due to the lower temperatures having already provided the required thermal energy for the passivation effect to occur at the higher temperatures while the sample has also never reached a steady state. This process could allow for fundamental processes to be seen.

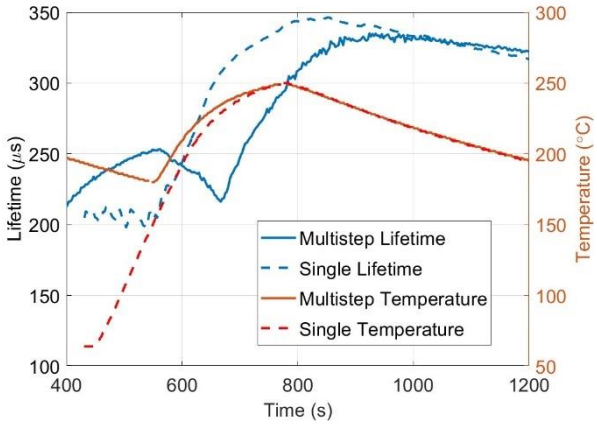

Figure 4-14: Comparison of the multistep sample with the single step sample at 250°C.

Comparing the 1 nm ((Figure 4-13) and 9 nm (Figure 4-15) a similar behaviour can be seen, with the optimum annealing temperature increasing with thickness. The cause of the two small bumps seen Figure 4-15 for 275°C and 300°C heating ramps is unknown.

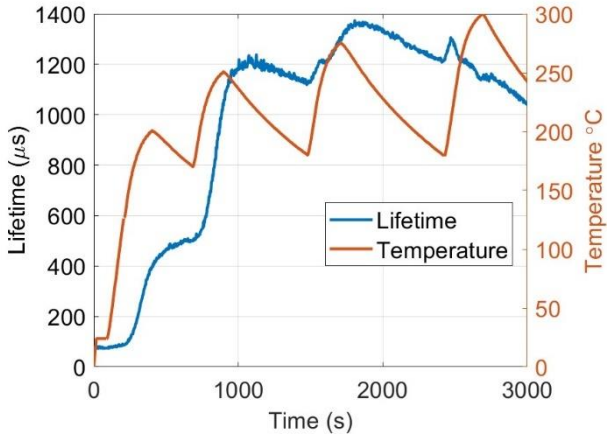

Figure 4-15: 9 nm ALD AlO_x heated to 200°C, 250°C, 275°C, and 300°C with partial cooling in between temperature peaks.

4.3.3 Lifetime Versus Photoluminescence

In-situ PL is a widely utilised technique being applied to a large range of materials for studying the influence of process parameters on surface passivation of crystalline Si wafers during any form of deposition or fabrication process [29], [31]–[33], [36], [100], [101]. In-situ τ_{eff} using MPL having only recently been developed, has shown promising results for determining processes occurring during annealing and plasma exposure

within a PECVD reactor [32], [34]. However, no direct comparison between in-situ MPL & PL has yet been performed. Thus, a peak annealing profile is chosen to compare the two techniques

The annealing profile peak temperature was 300°C (Figure 4-16 top), with both PL and τ_{eff} being measured concurrently (Figure 4-16 bottom). The total PL intensity was estimated by integrating the area under the obtained PL spectra obtained with a measurement period of 2 s.

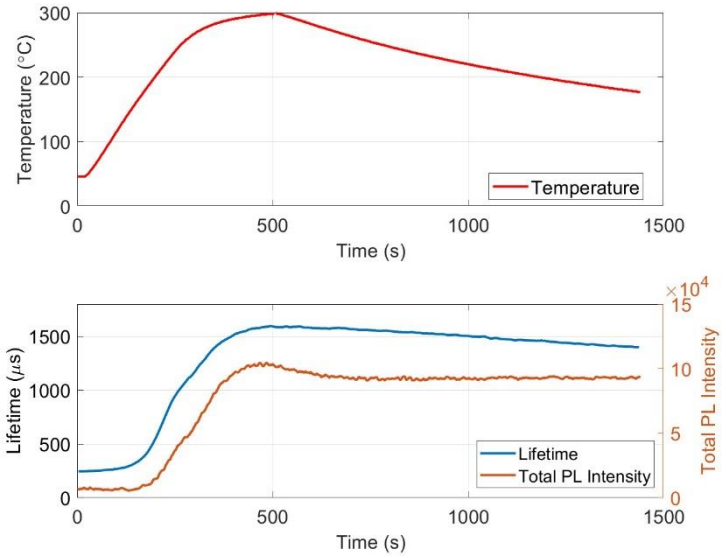

Figure 4-16: Annealing profile and the subsequent in-situ PL and in-situ τ_{eff} profiles measured.

When observing the initial increase in τ_{eff} we can see that the PL (Figure 4-16) also increases in a similar fashion, however before reaching the peak temperature the total PL intensity increases further deviating from the τ_{eff}, and after cooling it remains constant. This hypothesised to be attributed to the thermal radiation recorded by the spectrometer within the 900 – 1300 nm range in which the integration is performed, being received from part of the RF electrode. Once cooling begins, and the thermal radiation disappears, a mismatch begins to occur between the τ_{eff} and PL as one decreases and the other remains steady.

Viewing the PL spectrum of Figure 4-16 bottom at 3 temperature periods (Figure 4-17) i) the start ii) peak temperature iii) during cooling, the impact of the thermal radiation can be seen on the total PL calculations which was taken over the range of 900 – 1300 nm. At 190°C the thermal radiation begins to be visible at 1300 nm thus beginning to impact on the total PL calculated.

This is based on the sensitivity of the spectrometer and optics system being used.

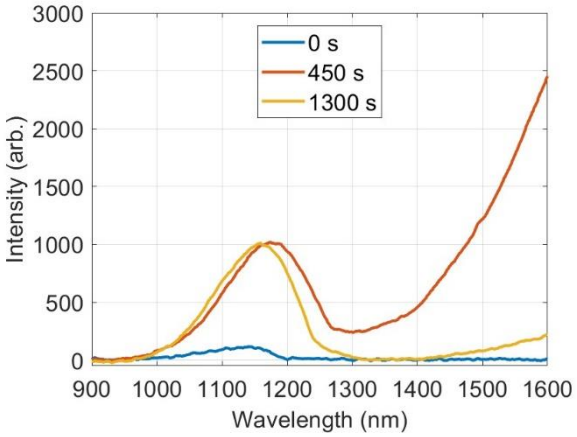

Figure 4-17: PL spectrum from Figure 4-16 at times 0 s (24°C), 450 s (300°C) and 1300 s (190°C).

The relationship between the electron lifetime and total photoluminescence intensity is not straightforward, as these properties are affected by different factors. τ_{eff} is a process measured via the radiative recombination of silicon while PL is primarily based on the band gap of the material, while both are inherently linked, an understanding of direct to indirect bandgap materials focusing on the addition of phonon interactions could be a possible place to start.

4.3.4 Temperature from thermal radiation

Thermal radiation is a fundamental physical phenomenon associated with the emission of energy by matter due to its temperature. The primary principle governing thermal radiation is the Planck's law of black-body radiation, which provides the spectral distribution of energy radiated by a black body in thermal equilibrium (Eq 4.1). A black body is a theoretical or model body which absorbs all incident electromagnetic radiation, regardless of frequency or angle of incidence. Planck's law describes the spectral radiance (amount of energy at each frequency) of electromagnetic radiation at all wavelengths from a black body at temperature T. In other words, the amount of spectral radiance at each frequency (or, equivalently, at each wavelength) emitted by a black body in thermal equilibrium (Figure 4-18).

$$B(\lambda, T) = \left(\frac{2hc^2}{\lambda^5} \frac{1}{e^{\frac{hc}{\lambda k_B T}} - 1} \right) * C + D \qquad \text{Eq.4.1}$$

$h = \ Planks\ constant$
$c = \ Speed\ of\ light\ \left(\frac{m}{s}\right)$
$\lambda = \ Wavelength\ (m)$
$T = Temperature\ (Kelvin)$
$C, D = Scaling\ factors\ for\ fitting$

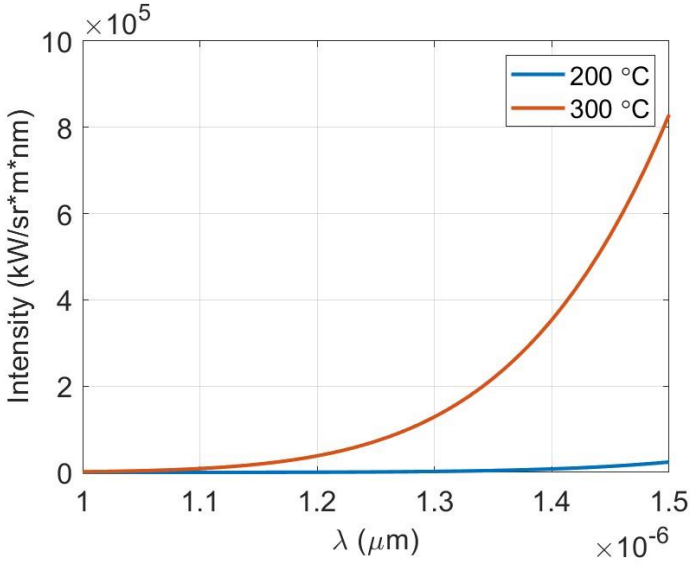

Figure 4-18: Plot of 200 °C and 300 °C between 1000 nm and 1500 nm wavelength using Eq 4.1.

The mismatch between the PL Peak and the maximum temperature achieved can be attributed to the unequal heating of the RF electrode and the substrate holder (Figure 4-19). Performing a standalone measurement it was shown the RF electrode will reach the set peak temperature faster than that of the substrate holder, hence in Figure 4-16 the PL bump due to thermal radiation can be attributed to the RF electrode reaching a higher temperature first.

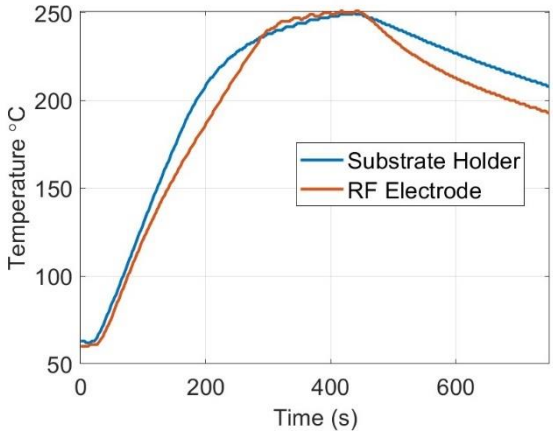

Figure 4-19: Measured temperature of a 250°C peak annealing profile of the substrate holder and RF electrode.

To ensure the thermal radiation contribution was from the RF electrode, the thermal radiation portion of a measured PL spectra of heating a sample to 250°C was fitted with Planks law (Eq.6) including a vertical scaling factor C (Figure 4-20) were applied.

$$B(\lambda, T) = \left(\frac{2hc^2}{\lambda^5} \frac{1}{e^{\frac{hc}{\lambda k_B T}} - 1} \right) * C \qquad \text{Eq.6}$$

Using a different set of data in which only the PL spectra and substrate holder temperature, with a sample placed on the stage, were measured (Figure 4-20) the calculated temperature does not match the substrate temperature. This experiment began at 150°C which means the initial temperature gradients will be different to that of Figure 4-19.

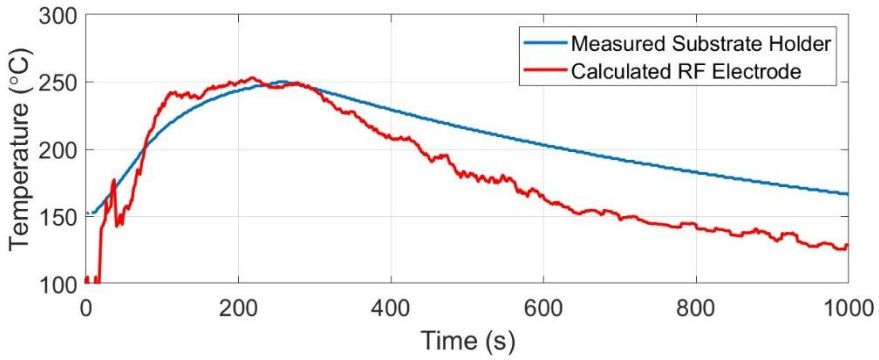

Figure 4-20: RF electrode temperature calculated from the thermal radiation

using the PL spectra and Eq.6.

Overlaying the data from the two figures (Figure 4-21), due to the initial heating temperatures being different until the peak is reached the profiles cannot be accurately compared. However, overlaying the cooling curves of the substrate holder it can be seen they are the same meaning this section of data is valid for comparison. As seen, the calculated temperature matches the peak and initial temperature decrease however it continues to decrease further after which it maintains a similar curve (600 s onwards). It is worth noting that in Figure 4-19 and Figure 4-20 RF electrode and calculated temperature both reach a higher temperature before the substrate holder, perhaps indicating this portion could be used.

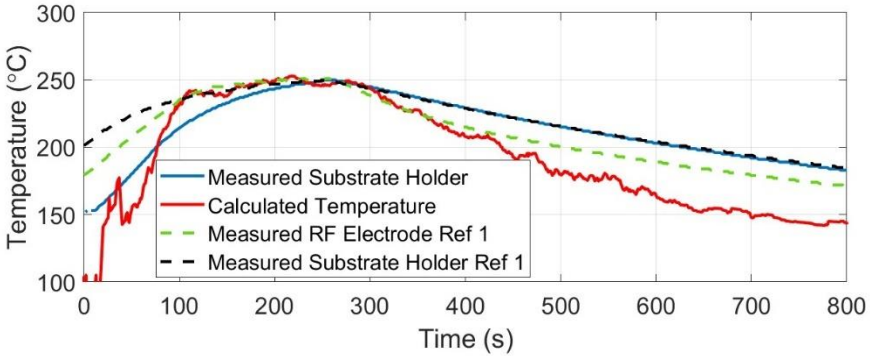

Figure 4-21: Data sets from Figure 4-19 and Figure 4-20 overlayed.

A previous experiment to determine 'silicon temperature measurement by infrared absorption' proves that at elevated temperatures (400-800 ℃) 1.3 and 1.55 µm light may pass through a silicon wafer [102]. Assuming AlO_x works similarly, the collection of thermal radiation within the PECVD reactor will look like Figure 4-22. Thus, the thermal radiation which becomes visible on the spectrometer will be a combination of the sample and RF electrode, more so the RF electrode due to the collection area available to it.

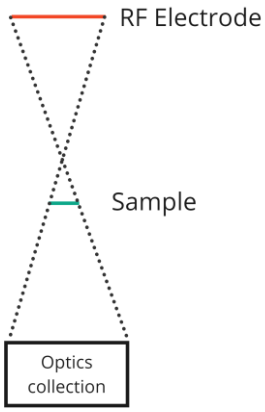

Figure 4-22: Depiction (not to scale) of the thermal radiation collection from within the reactor.

Comparing it to the measured temperatures is also difficult given the location of the thermocouples. As shown in Figure 2-3 the thermocouples for the substrate holder are located within the bulk not surface, similarly with the RF electrode. H_2 gas entering through the PECVD showerhead will also reduce its temperature and that of the substrate holder.

4.4 LIGHT ENHANCED FIELD EFFECT PASSIVATION

The effects of UV illumination of AlO_x on τ_{eff} were initially discovered in 1989 and subsequently in 2009 its potential for photovoltaics was realized [82], [103]. Light-induced field effect modification (LIFEM) is a technique that use light to modify the electrical properties of a material. In a LIFEM experiment, light is shone on a material and the resulting change in the material's passivation quality can be observed, in our case the light source is the laser used for the lifetime measurements with a photon energy of 1.58 eV (785 nm). By varying the intensity, duration, and wavelength of the light, researchers can study how the electrical properties of the material are affected by the light and understand the underlying physical processes that govern these effects (Figure 4-23).

The increase in the fixed charge in the AlO_x thin film during illumination can be attributed to the injection of electrons into interface or bulk states. This can occur through two pathways both requiring above 3.12 eV to enter into the AlO_x conduction band before trapping occurs [104]:

- Single photon absorption [104].
- Multiple photon excitation (second harmonic generation) via

injection of lower energy photons passing the required threshold at the interface of the silicon [105].

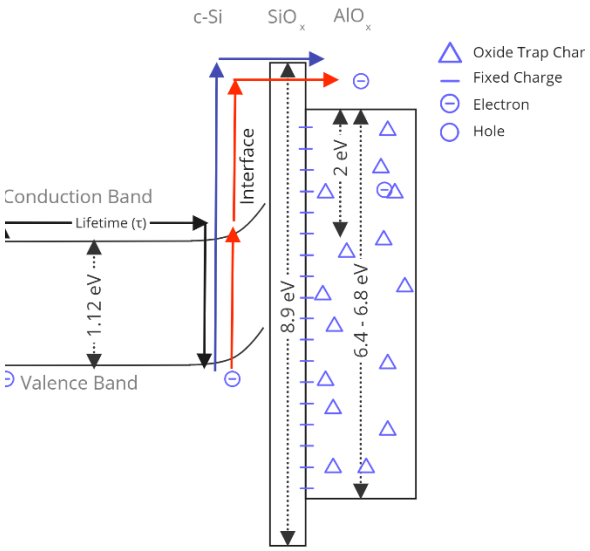

Figure 4-23: Photo-injection models from the c-Si valence band to the Al_2O_3 conduction band.

An as-deposited sample can exhibit these effects quickly over a short term period of 100 s (*Figure 4-24*) or over a much longer 1.5 hours (*Figure 3-28*). There is no difference between the samples other than exposure time and being from different wafers. This would indicate there are many traps within the layer. At higher temperatures, this phenomenon could be faster and stronger as shown below (*Figure 4-26*).

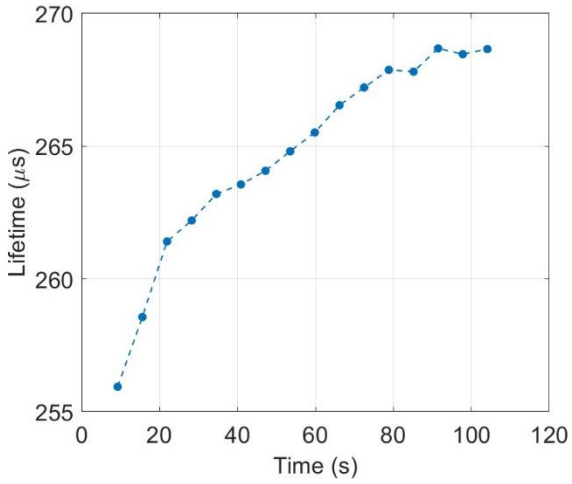

Figure 4-24: Lifetime measured during light-soaking of an as-deposited

sample at room temperature over a period of 100 seconds showing an increase of ~17 µs.

4.4.1 High temperature Illumination

While AlOx has been shown to retain the light-soaking effects received during high temperature annealing, it has never been reported on what the effect on the lifetime would be if illuminated after dark annealing while remaining at the given temperature. A sample was annealed at 200 °C in the dark for 20 mins at which point τ_{eff} was measured during 5 mins then cooled down in the dark to room temperature after which, another τ_{eff} measurement was performed again (Figure 4-25).

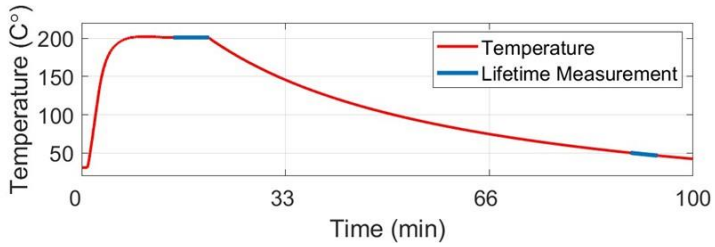

Figure 4-25: Annealing profile and illumination periods.

At 200 °C, the initial 40 s of light soaking (Figure 4-26 left) results in a τ_{eff} increase of 300 µs after which τ_{eff} plateaus. In contrast to room temperature (Figure 3-28) the resulting increase in τ_{eff} is much larger and requires less time. This could be due to a larger number of electrons being injected into the bulk AlO_x layer with the assistance of thermal energy being provided to the electrons via double photon excitation Figure 4-27 a).

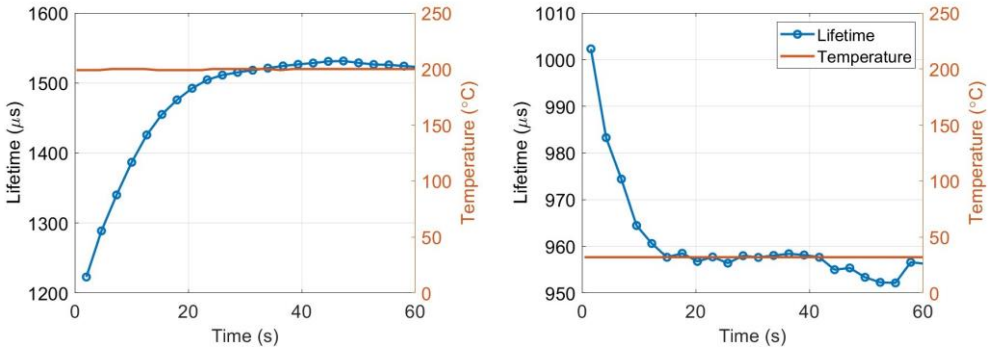

Figure 4-26: a) EL measurement after dark annealing the AlOx sample for 20 mins b) EL measurement after cooling the AlOx sample in the dark.

During the second illumination period, at room temperature, τ_{eff} initially decreases slightly by 40 µs then plateaus. This could be attributed to the τ_{eff} gain being retained during cooling due to electrons remaining in deep level defects within the AlO_x layer Figure 4-27 b). After illumination, an equilibrium state within the sample is attained, tunnelling of the 'deep electrons' to the generated holes resulting in recombination could do this. Note that the decrease is much smaller than the increase at 200℃ noting that there could be an irreversible portion. This could be checked only by performing illumination after annealing.

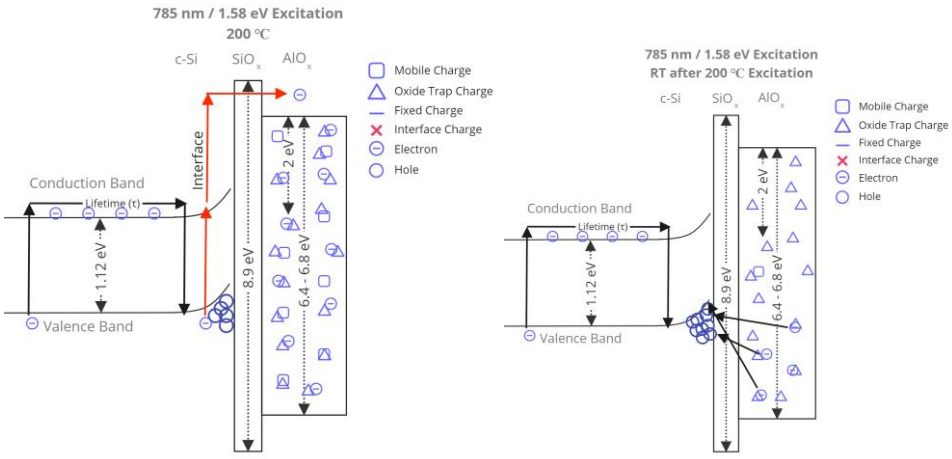

Figure 4-27: Resulting behaviour of Figure 4-26: a) EL measurement after dark annealing the AlOx sample for 20 mins b) EL measurement after cooling the AlOx sample in the dark.Figure 4-26 a) and b) respectively

4.5 HYDROGENATION

To date, it has been well shown that hydrogen can passivate various defects such as crystallographic defects in multi-crystalline silicon (mc-Si), metal impurities, laser-induced defects, and the surfaces of crystalline silicon. Atomic hydrogen is considered an effective element to reduce the surface recombination velocity due to the passivation of silicon interface dangling bonds, however this has mainly been applied to amorphous silicon layers. [106], [107]. Using a hydrogen plasma in the following section was intended to act as a hydrogenation source for the AlO_x however, a comparison with argon plasma and effusion measurements would be required to properly understand its implications [108].

4.5.1 Post-Annealing Plasma

Studies based on in-situ PL to understand the effects of exposing ALD-AlOx

to H_2 and Ar/H_2 plasmas concluded that degradation of c-Si surface passivation during plasma exposure occurs due to breaking of interfacial chemical bonds [33], [34]. VUV light emitted from the plasma can penetrate the AlO_x passivation layer, resulting in breakage of the bonds at the interface and increasing the SRH recombination of charge carriers. To recover the surface passivation, the degraded samples were annealed in a H_2 environment (1 Tor) showing the surface passivation starts to recover at around 220°C and continues to steady-state value. If exposed to a plasma at a high temperature the recovery was found to be much faster [34]. To compare the in-situ PL results from [34] with in-situ τ_{eff}, a similar temperature profile (Figure 4-28 Top) and matching plasma exposures were performed with a long hydrogenation process added at high temperature. A sample which has been pre-annealed at 250°C during 10 mins was initially exposed to a 4 W hydrogen plasma (indicated in purple) at room temperature for 1 min after which a recovery annealing was performed then another 4 W hydrogen plasma was performed for 30 mins.

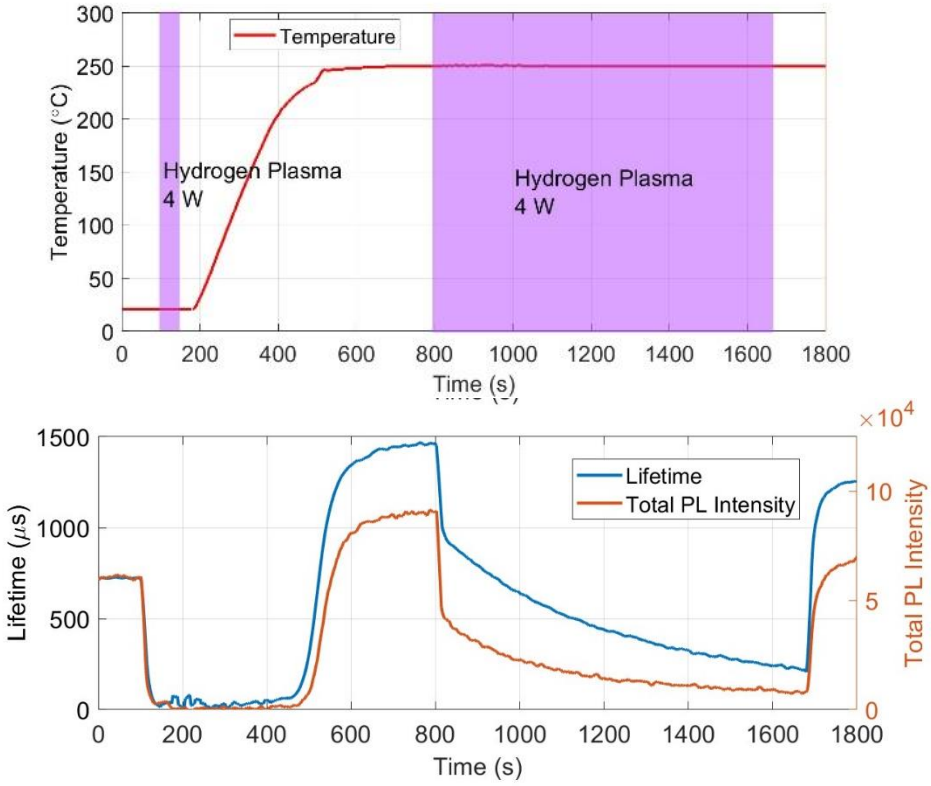

Figure 4-28: Top) Annealing profile and 4W hydrogen plasma regions highlighted in purple, indicating the exposure period. Bottom) in-situ PL and in-situ τ_{eff}.

Before the initial plasma exposure at room temperature (Figure 4-28 Bottom) the PL intensity and τ_{eff} can be scaled to have their initial intensities match, with the resulting decreasing values, due to the plasma, following the same evolution and showing there is no discrepancy between the two measurements, in agreement with what was previously published [34]. However, during heating at 250°C, to anneal defects created by the H_2 plasma (VUV bond breakage), while the shapes do match, the intensity does not. The requirement of a minimum temperature is likely due to a minimum thermal energy to enable atomic hydrogen diffusion to occur. Performing a plasma exposure at 250°C, a similar behaviour is observed for both, yet differences between the two techniques can be seen for all the parts of the curve, the exact origin is unknown. The initial fast decrease of τ_{eff} is considered to be due to breaking the interfacial Si-O bonds [34]. The slow curve decreasing could be associated with the diffusion of atomic hydrogen from the AlO_x into the silicon wafer or atmosphere. The fast recovery would therefore be the return of atomic hydrogen to the interface from the silicon at an increased rate, bond recovery, and possibly the surface charge being removed. The final τ_{eff} is lower than that before plasma exposure at 250°C.

A point of interest is the final individual measurement technique intensity values do not match each other. PL gives the indication that the τ_{eff} has increase a small proportion to its initial value while τ_{eff} measurement indicates a clear difference from room temperature to 250°C. This mismatch indicates as well that there is a difference in what τ_{eff} and PL results explain regarding the sample.

4.5.1.1 Increased Thickness

To determine if the slow decrease in τ_{eff} during the second H_2 plasma exposure in Figure 4-28 bottom is due to atomic hydrogen diffusion, a 50 nm AlO_x layer was used as to have a larger supply of hydrogen (Figure 4-29). After heating the sample to 300°C and annealing until a stable τ_{eff} was reached, H_2 plasma exposure was performed. As in previous experiments with thinner AlOx samples, we observe a strong decrease in lifetime upon turning the plasma ON. Notice that the initial lifetime increases with the AlOx layer thickness: 2500 µsec for 50 nm, 1500 µsec for 9 nm and only 300 µsec for 1 nm. Moreover the 50 nm AlOx sample shows a plateau appearing between the fast and slow decreasing τ_{eff} sections. This is being attributed to the 50 nm layer acting as an atomic hydrogen reservoir which maintains a constant lifetime during the diffusion process until there is no longer enough

bypassing through the interface to create momentary surface passivation bonds.

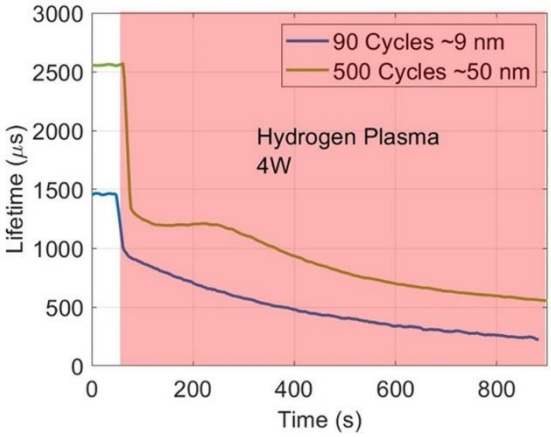

Figure 4-29: H_2 plasma exposure at 300°C using a 50 nm AlOx sample.

4.5.1.2 Secondary Plasma Exposure

Additional plasma exposures during fabrication for further layer depositions is a high possibility. When performed it is of importance to ensure the thermal budget for lifetime recovery can be maintained. After the recovery of τ_{eff} (Figure 4-30) a sample was exposed to both argon and hydrogen plasma separately with a τ_{eff} recovery in between. Notable there is no difference between the recovery values further indicating it is the UV light generated by the plasma creating the defects.

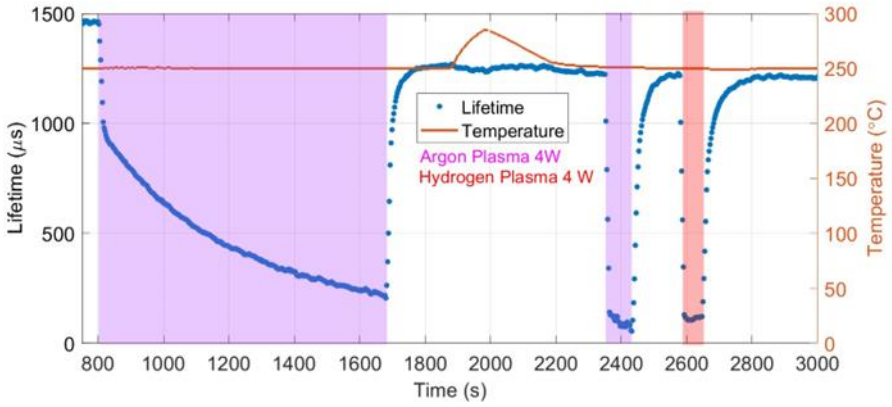

Figure 4-30: Secondary plasma exposure of Argon and Hydrogen plasma after an initial hydrogenation period

Repeating the hydrogenation process of *Figure 4-30* until a plateau at 300 ℃

,Figure 4-31 shows 3 temperature variations of the secondary plasma process. With each decreasing temperature the duration required for τ_{eff} recovery takes longer. This could be potentially due to the hydrogenation diffusion back to the interface taking a longer duration than previously required

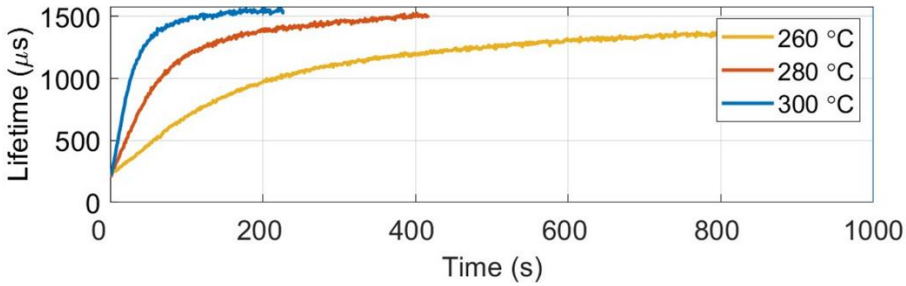

Figure 4-31: UV light exposure (generated by plasma) at 3 temperatures after hydrogenation

4.6 Chapter Review

In this chapter a focus on optimising and analysing the τ_{eff} based on various experiments which are possible to perform within a PECVD reactor using ALD-AlO_x (1, 9, 50 nm) silicon wafers.

- An example of how to perform optimum annealing treatments using in-situ τ_{eff} to compare a profile with peak temperature vs plateau profile showing that a peak temperature is more thermally efficient and that multiple subsequent peaks can be used for determining the optimal annealing temperature.
- In-situ PL and in-situ τ_{eff} were compared showing that while a total PL intensity profile similar to τ_{eff} can be achieved, due to the inherent differences from where the two phenomena originate, they will not be the same.
- Using thermal radiation of a PL spectra to determine the temperature most likely resulted in a combination of RF electrode temperature and sample temperature being mixed.
- Illumination at elevated temperatures then cooling in the dark can create a light enhanced field effect passivation which can be retained in the AlO_x layer.
- Hydrogen diffusion was found to occur during VUV light (generated by H_2 plasma) exposure with a thicker layer capable of acting as a hydrogen reservoir.
- It was shown to maintain a thermal budget, if performing another

plasma process you have to keep the same temperature.

5 CONCLUSIONS & PROSPECTIVES

The purpose of this chapter is to consolidate the principal findings that emerged from chapters 2-4, providing a summation of their significance in the broader academic and practical context. Moreover, in recognizing that every study, no matter how exhaustive, leaves some stones unturned, we will venture into a discussion on prospective directions—suggesting avenues for future research, potential applications of the findings, and their implications for the respective field of study.

5.1 HARDWARE

5.1.1 In-situ Optics Design

The initial aim was to create seamless compatibility with industry-standard componentry for simplicity of construction. Using Thorlabs componentry a device capable of fast reconstruction was made with the core component of the compound parabolic concentrator (CPC) being the only part requiring customization. The design shows the simplicity in which the collection of PL for a lifetime measurement can be performed and easy of installation without the need for complex custom componentry or lens systems.

Another design iteration is required for the design to be fully finalised before being acceptable for production for either one specific design or multiple designs (Figure 5-1). It primarily is concerned with the size of the Thorlabs cage system used, currently 30 mm, for mounting all the optical components within and either using a beam profiler which is capable of long distances, up to 3 m, or one with a short distance of up to 30 cm. The CPC would have to be modelled following specifications of the cage system sizing, desired illumination spot size, and type of photodiode used.

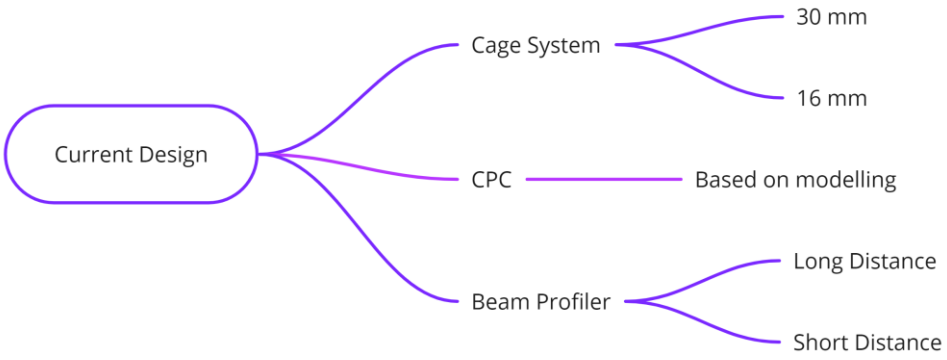

Figure 5-1: Decision tree for the next in-situ design iteration

5.1.2 PECVD Reactor retrofitting

The PECVD reactor was successfully retrofitted using an RS-485 I/O module. The high degree of flexibility allowed by such a device is in the separation of the control hardware and computing system. While not as compact as an embedded PC, the reduction in cost and separation of the PC from the various available modules allows for each system to be upgraded separately which is especially useful in the case of this PhD given the dual use of the PC for reactor control and lifetime measurements.

While using MATLAB for the user interface is not standard and certainly does have its own challenges, switching from requiring an active instance of MATLAB to a stand alone app would solve them. A more traditional software such as LabVIEW could also be used to create a stand alone app.

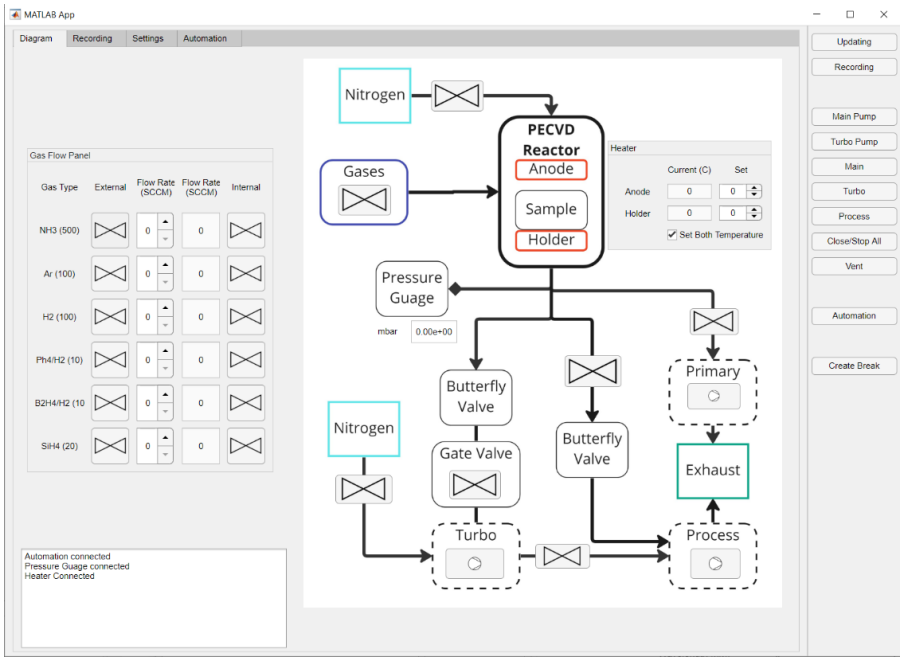

Figure 5-2: Image on the reactor control system designed for PLASMAT using MATLAB.

5.2 Minority Carrier Lifetime

5.2.1 Modulated Photoluminescence

The initial aim for MPL was to increase the speed at which it is performed. This was successfully achieved through the implementation of Dolphin's wave using a frequency sweep superimposed on a larger wave shafting through the excess carrier densities. It must be stated that the calculations developed for MPL did not account for the introduction of a phase shift within the base intensity thus it is essentially bending the theory somewhat which limits the speed.

To further increase the speed of phase shift extractions for MPL for either lifetime measurements or other applications, multiple frequency sweeps can be stacked with the drawback of the signal being split proportionally as the quasi steady state regime must be maintained.

5.2.2 Direct Lifetime Measurement

To reduce the complexity of measuring a lifetime value, a switch between

indirect and direct measurement of the initial τ required the shift concept of Figure 3-14 to be performed to result in a τ. Given time is immaterial the removal of needing excess information from doing something to the sample was a success (phase shift). More work certainly needs to be done on expanding the intensity range capable of being measured. If the system is not sensitive enough and the Gaussian pulse is too intense a focus on the convolution of an exponential decay and a Gaussian would be required.

To develop a machine which is capable of performing the concept of Figure 3-14 correctly, the following 3 experiments need to be performed to stress test the device to ensure a strong enough signal is achieved to allow for small enough measurements to be performed which do not perturb the sample. The utilization of an operational amplifier to amplify a dynamic photocurrent is known to introduce a phase lag, therefore each experiment will result in some form of lag which can be checked as it has been previously with using a reflective piece of material in the system.

1) Dirac approximation function: Similar to the Gaussian function used earlier, however, the exponential increase with a sharp peak will show a response in the system. It is essentially a more intense way to perform the same measurement as it does not allow for any form of relaxation before decreasing. The fineness of the resulting peak will be a main determining factor as to the sensitivity of the system.

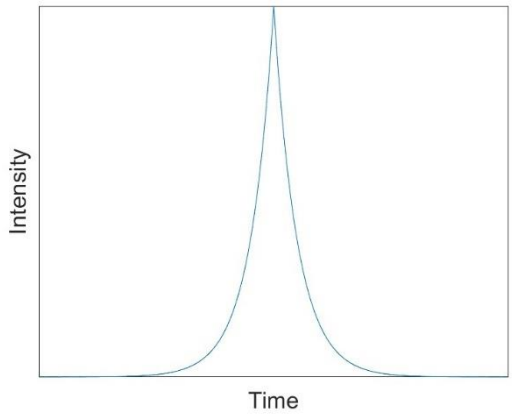

Figure 5-3: A generic Dirac function represented using an equation

2) A logistics curve to a step function: As lifetime can be measured from point to point, a the transition between excess carrier states can also be done. Initially starting with a logistics curve to account for system sensitivity, this will result in a hysterisis on the rise and plateau, while

using the central point in the vertical transition for the lifetime measurement. Reducing the step size should allow for the transition to a steeper step resulting in a step function from which the horizontal shift in the vertical step can be used. It can be considered as 'zooming in' similarly to what the Gaussian bump does in regards to focusing on 0 Hz.

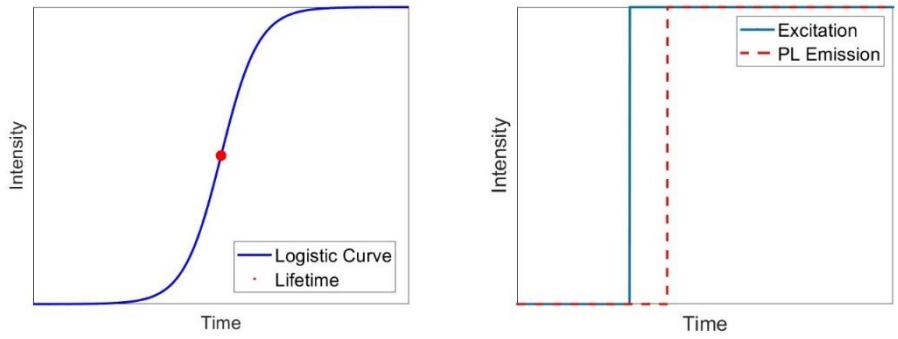

Figure 5-4: Left) A logistics curve Right) A step function

3) Transition from background noise to an applied noise: The transition between noise states allows for the lifetime to be seen. This should focuses on the removal of the system hysterisis given from the electrical components.

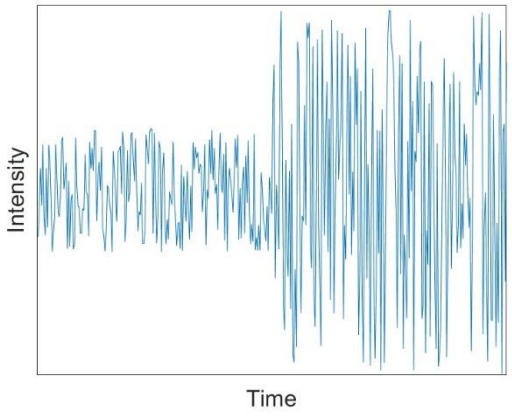

Figure 5-5: A signal switching between two noise intensities

5.2.3 Hardware Design

The changing of hardware from using a lock-in amplifier to a datalogger for performing all the calculations on a computer was a success. MATLAB allowed for the rapid implementation of wavelets while using various other

toolboxes for processing the data.

As the optics, the hardware design required for development to an acceptable level for sale requires the removal of the secondary loop created by the need to feedback the signal from the laser to the data logger (Figure 5-6). This can be solved by using a dualband Si/InGaAs photodiode which would also help with the S/N ratio.

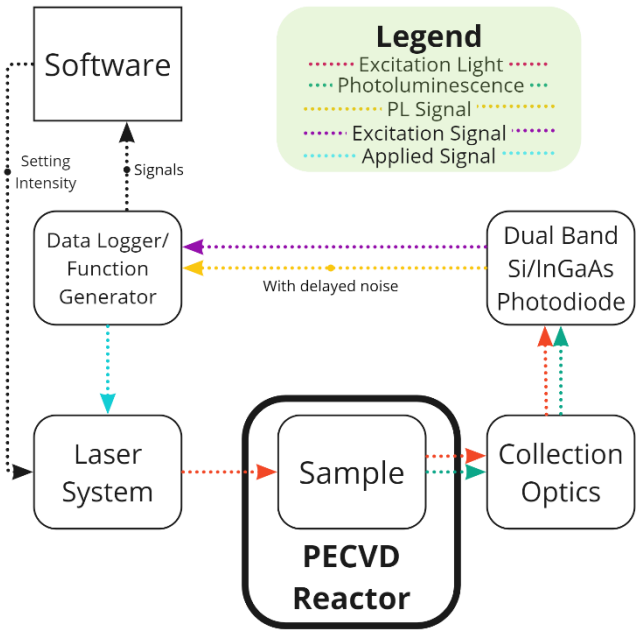

Figure 5-6: Required improvement of design required

Improving the computer system would also be required to perform the measurements and calculations at a faster rate and on materials, such as Perovskite or III-V, which have much lower lifetimes. This is due to the acquisition rate being directly related to the lifetime resolution, hence a PCI oscilloscope and function generator are key.

5.3 Aluminium Oxide

Given the proposed usefulness of AlO_x the use of in-situ τ_{eff} was successful in 3 areas:

1) The annealing profile was shown to be modifiable allowing the same τ_{eff} values to be reached with different thermal budgets using a peak and plateau method, while the optimal peak annealing temperature can be found with consecutive increasing heating/cooling curves

using the same sample.
Comparing τ_{eff} and total PL shows different values indicating one or the other has to be chosen for the base metric. This is because they originate from different phenomenon. In this case τ_{eff} was chosen as it was the topic.

2) It was shown that performing light enhanced field effect passivation at 250°C and cooling in the dark allows for electrons to remain trapped within the AlO_x layer and are able to be released by illumination at RT. This could potentially be useful for industrial application as it is a modification of the electrical state of the surface layer which could effect future depositions.
3) Hydrogenation has been a long known useful process for increasing the τ_{eff} within a sample when correctly optimised. Comparing τ_{eff} and PL measurements, during VUV light exposure resulting in breaking hydrogen bonds and resulting movement, it was seen there is a clear difference between the two measurements regarding potential efficiency at 250°C which further highlights the difference in where the measurements are coming from. As τ_{eff} is electrical, and PL is structural, the difference between the two should be useful for creating a model.
   Increasing the AlO_x layer thickness to 50 nm resulted in a reservoir type behaviour enabling the τ_{eff} to be maintained during the hydrogen movement for a period of time before following the previously observed behaviour with 9 nm. It was also observed that τ_{eff} increased with thickness indicated an optimal thickness for reservoir size for passivation could be determined.
   To determine if the surface charge generated on the surface of a sample can influence the τ_{eff} a piece of MgF_2 glass was placed on the surface to block the hydrogen plasma but create a strong electrostatic charge at the glass substrate interface at 250°C with the assumption it behaves similarly to Corning glass at 280°C. The resulting recovery τ_{eff} after turning the plasma off indicates that there could be a potential influence on the hydrogen movement indicated by lower recovered lifetime.

The speed at which experiments are performed is a high factor towards progression, building a cluster tool around the in-situ τ_{eff} device to increase the experimentation rate is required.

6 APPENDIX

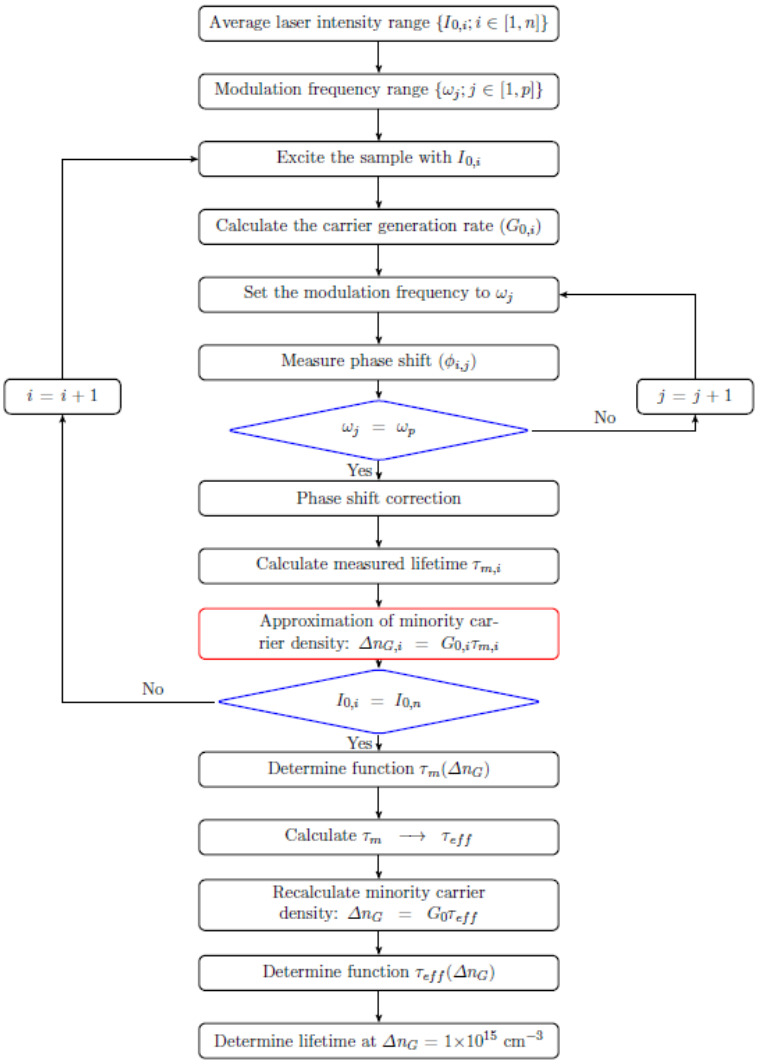

Figure 6-1: LiTe algorithm diagram from [73].

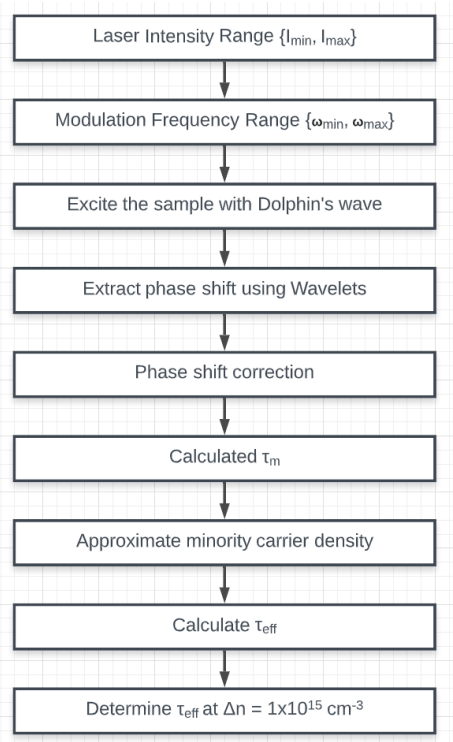

Figure 6-2: New process steps replacing the original LiTe signal generation and phase shift extraction steps for MPL.

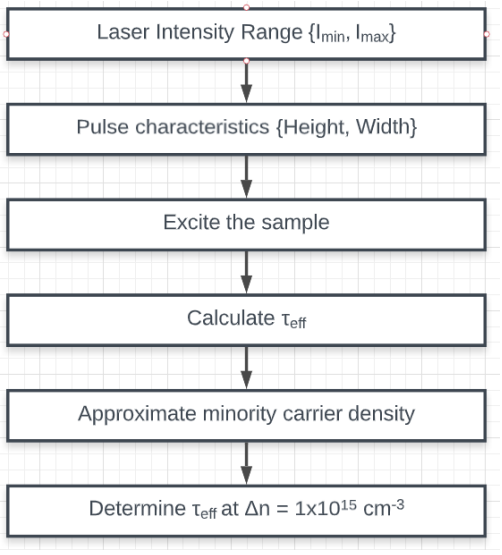

Figure 6-3: Simplified process diagram process diagram for determining a lifetime measurement via directly rather than indirectly.

Material inputs

Semiconductor	c-silicon		Temperature	T	300	K
Dopant species	Phosphorus		Excess carriers	Δn	1E+15	cm^{-3}
Dopant concentration	N_D	1E+16	cm^{-3}			
Equilibrium resistivity	ρ_b	0.529	Ω·cm			

Recombination models

Radiative	Fell2021					
Auger	Niewelt2022					
SRH	SRH equation	τ_{n0}	100	µs	τ_{p0}	100 µs
		E_t–E_i	0	eV		

Figure 6-4: PV lighthouse simulation settings.

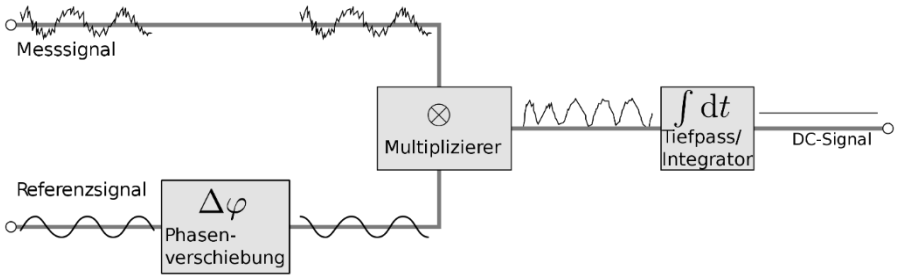

Figure 6-5: Schematic depicting the working principles of a lock-in amplifier.

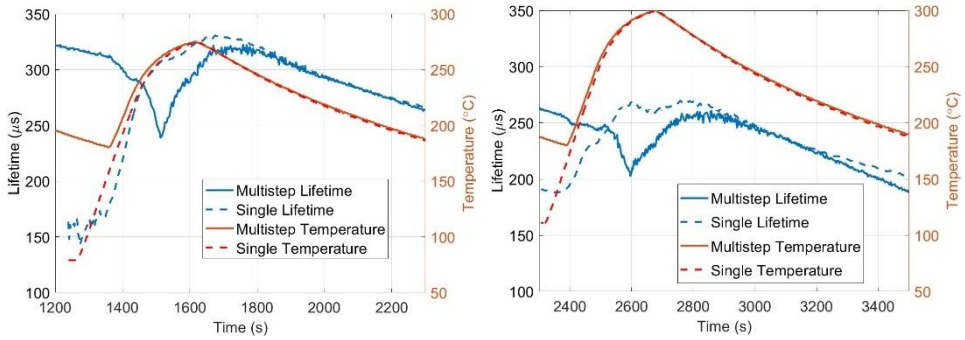

Figure 6-6: Comparison of the multistep sample with the single step sample at 275C° (Left) and 300°C (Right).

7 REFERENCES

[1] 'Greene's Groats-Worth of Wit | The British Library'. https://www.bl.uk/collection-items/greenes-groats-worth-of-wit (accessed Aug. 12, 2023).

[2] P. C. Jain, 'Greenhouse effect and climate change: scientific basis and overview', *Renewable Energy*, vol. 3, no. 4, pp. 403–420, Jun. 1993, doi: 10.1016/0960-1481(93)90108-S.

[3] 'A review of trends and drivers of greenhouse gas emissions by sector from 1990 to 2018 - IOPscience'. https://iopscience.iop.org/article/10.1088/1748-9326/abee4e (accessed Jun. 11, 2023).

[4] S. R. Weiskopf *et al.*, 'Climate change effects on biodiversity, ecosystems, ecosystem services, and natural resource management in the United States', *Science of The Total Environment*, vol. 733, p. 137782, Sep. 2020, doi: 10.1016/j.scitotenv.2020.137782.

[5] M. A. Hanjra and M. E. Qureshi, 'Global water crisis and future food security in an era of climate change', *Food Policy*, vol. 35, no. 5, pp. 365–377, Oct. 2010, doi: 10.1016/j.foodpol.2010.05.006.

[6] 'Renewable power on course to shatter more records as countries around the world speed up deployment - News', *IEA*. https://www.iea.org/news/renewable-power-on-course-to-shatter-more-records-as-countries-around-the-world-speed-up-deployment (accessed Jun. 11, 2023).

[7] Y. Guan *et al.*, 'Burden of the global energy price crisis on households', *Nat Energy*, vol. 8, no. 3, Art. no. 3, Mar. 2023, doi: 10.1038/s41560-023-01209-8.

[8] M. Mišík and A. Nosko, 'Post-pandemic lessons for EU energy and climate policy after the Russian invasion of Ukraine: Introduction to a special issue on EU green recovery in the post-Covid-19 period', *Energy Policy*, vol. 177, p. 113546, Jun. 2023, doi: 10.1016/j.enpol.2023.113546.

[9] 'Electricity Market Report 2023 – Analysis', *IEA*. https://www.iea.org/reports/electricity-market-report-2023/executive-summary (accessed Jun. 10, 2023).

[10] 'Changes in global electricity generation by source, 2021-2025', *IEA*. https://www.iea.org/reports/electricity-market-report-2023/executive-summary (accessed Jun. 11, 2023).

[11] 'ECIU', *Energy & Climate Intelligence Unit*. https://eciu.net/ (accessed Nov. 30, 2022).

[12] 'Photovoltaics at multi-terawatt scale: Waiting is not an option | Science',

Science, vol. 380, pp. 39–42, 2023, doi: 10.1126/science.adf6957.
[13] G. Lobaccaro, S. Chatzichristos, and V. A. Leon, 'Solar Optimization of Housing Development', *Energy Procedia*, vol. 91, pp. 868–875, Jun. 2016, doi: 10.1016/j.egypro.2016.06.253.
[14] J. Palm and E. Eriksson, 'Residential solar electricity adoption: how households in Sweden search for and use information', *Energy, Sustainability and Society*, vol. 8, no. 1, p. 14, May 2018, doi: 10.1186/s13705-018-0156-1.
[15] C. Toledo and A. Scognamiglio, 'Agrivoltaic Systems Design and Assessment: A Critical Review, and a Descriptive Model towards a Sustainable Landscape Vision (Three-Dimensional Agrivoltaic Patterns)', *Sustainability*, vol. 13, p. 6871, Jun. 2021, doi: 10.3390/su13126871.
[16] 'RES4Africa presents two new study on agrivoltaics and desalination in the MENA region - Res4Africa', Jun. 28, 2023. https://res4africa.org/news/2023/res4africa-presents-two-new-study-on-agrivoltaics-and-desalination-in-the-mena-region/ (accessed Jul. 18, 2023).
[17] A. Weselek, A. Bauerle, J. Hartung, S. Zikeli, I. Lewandowski, and P. Högy, 'Agrivoltaic system impacts on microclimate and yield of different crops within an organic crop rotation in a temperate climate', *Agron. Sustain. Dev.*, vol. 41, no. 5, p. 59, Aug. 2021, doi: 10.1007/s13593-021-00714-y.
[18] I. Guaita-Pradas, I. Marques-Perez, A. Gallego, and B. Segura, 'Analyzing territory for the sustainable development of solar photovoltaic power using GIS databases', *Environ Monit Assess*, vol. 191, no. 12, p. 764, Nov. 2019, doi: 10.1007/s10661-019-7871-8.
[19] P. Roddis, K. Roelich, K. Tran, S. Carver, M. Dallimer, and G. Ziv, 'What shapes community acceptance of large-scale solar farms? A case study of the UK's first "nationally significant" solar farm', *Solar Energy*, vol. 209, pp. 235–244, Oct. 2020, doi: 10.1016/j.solener.2020.08.065.
[20] 'A Review of Hybrid Solar PV and Wind Energy System'. https://www.tandfonline.com/doi/epdf/10.1080/23080477.2015.11665647?needAccess=true&role=button (accessed Jun. 10, 2023).
[21] D. Tong *et al.*, 'Geophysical constraints on the reliability of solar and wind power worldwide', *Nat Commun*, vol. 12, no. 1, Art. no. 1, Oct. 2021, doi: 10.1038/s41467-021-26355-z.
[22] S. A. Alves dos Santos, J. P. N. Torres, C. A. F. Fernandes, and R. A. Marques Lameirinhas, 'The impact of aging of solar cells on the performance of photovoltaic panels', *Energy Conversion and Management: X*, vol. 10, p. 100082, Jun. 2021, doi: 10.1016/j.ecmx.2021.100082.
[23] W. Shockley and H. J. Queisser, 'Detailed Balance Limit of Efficiency of p-n Junction Solar Cells', *Journal of Applied Physics*, vol. 32, no. 3, pp. 510–519, Mar. 1961, doi: 10.1063/1.1736034.

[24] 'Best Research-Cell Efficiency Chart'. https://www.nrel.gov/pv/cell-efficiency.html (accessed Nov. 29, 2022).
[25] B. Kafle, B. S. Goraya, S. Mack, F. Feldmann, S. Nold, and J. Rentsch, 'TOPCon – Technology options for cost efficient industrial manufacturing', *Solar Energy Materials and Solar Cells*, vol. 227, p. 111100, Aug. 2021, doi: 10.1016/j.solmat.2021.111100.
[26] 'International Technology Roadmap for Photovoltaic (ITRPV) - vdma.org - VDMA'. https://www.vdma.org/international-technology-roadmap-photovoltaic (accessed Jun. 19, 2023).
[27] F. Haase *et al.*, 'Laser contact openings for local poly-Si-metal contacts enabling 26.1%-efficient POLO-IBC solar cells', *Solar Energy Materials and Solar Cells*, vol. 186, pp. 184–193, Nov. 2018, doi: 10.1016/j.solmat.2018.06.020.
[28] M. Shanawani, D. Masotti, and A. Costanzo, *THz Rectennas: Rectification Prospects & Challenges*. 2017.
[29] S. M. Greil, J. Rappich, L. Korte, and S. Bastide, 'In Situ PL and SPV Monitored Charge Carrier Injection During Metal Assisted Etching of Intrinsic a-Si Layers on c-Si', *ACS Appl. Mater. Interfaces*, vol. 7, no. 21, pp. 11654–11659, Jun. 2015, doi: 10.1021/acsami.5b02922.
[30] A. M. Antoine, B. Drevillon, and P. Roca i Cabarrocas, 'In situ investigation of the growth of rf glow-discharge deposited amorphous germanium and silicon films', *Journal of Applied Physics*, vol. 61, no. 7, pp. 2501–2508, Apr. 1987, doi: 10.1063/1.337924.
[31] F. Lebreton, S. Abolmasov, F. Silva, and P. Cabarrocas, 'In situ photoluminescence study of plasma-induced damage at the a-Si:H/c-Si interface', *Applied Physics Letters*, vol. 108, p. 051603, Feb. 2016, doi: 10.1063/1.4941298.
[32] A. Desthieux, J. Posada, and P. Cabarrocas, 'In situ Modulated Photoluminescence Study of the Hydrogenation Processes of Tunnel Oxide Passivating Contacts During Plasma Processes', *Plasma Processes and Polymers*, vol. e2200064, p. 8, May 2022, doi: 10.1002/ppap.202200064.
[33] M. Sreng, F. Silva, and P. Roca i Cabarrocas, 'In situ Photoluminescence Study of Plasma Effects on Passivation of Crystalline Silicon Coated with Aluminum Oxide', *physica status solidi (a)*, vol. 216, no. 10, p. 1800612, 2019, doi: 10.1002/pssa.201800612.
[34] M. Sreng, 'Development of in-situ photoluminescence characterization tools for the study of semiconductors for photovoltaics application', phdthesis, Institut Polytechnique de Paris, 2019. Accessed: Nov. 03, 2022. [Online]. Available: https://tel.archives-ouvertes.fr/tel-02496035
[35] S. M. Greil *et al.*, 'Etching of a-Si:H on c-Si absorber monitored by in situ photoluminescence measurements', *Energy Procedia*, vol. 8, pp. 269–274,

Jan. 2011, doi: 10.1016/j.egypro.2011.06.135.
[36] T. Niewelt, S. Mägdefessel, and M. C. Schubert, 'Fast in-situ photoluminescence analysis for a recombination parameterization of the fast BO defect component in silicon', *Journal of Applied Physics*, vol. 120, no. 8, p. 085705, Aug. 2016, doi: 10.1063/1.4961423.
[37] J. Hensen, R. Loonen, M. Archontiki, and M. Kanellis, 'Using building simulation for moving innovations across the "Valley of Death"', *REHVA Journal*, vol. 52, pp. 58–62, May 2015.
[38] H. F. Sterling and R. C. G. Swann, 'Chemical vapour deposition promoted by r.f. discharge', *Solid-State Electronics*, vol. 8, no. 8, pp. 653–654, Aug. 1965, doi: 10.1016/0038-1101(65)90033-X.
[39] T. D. Märk and G. H. Dunn, *Electron Impact Ionization*. Springer Science & Business Media, 2013.
[40] G. Kökbudak, E. Orhan, F. Es, E. Semiz, and R. Turan, 'Optimization of Silicon Nitride (SiNX) Anti-Reflective Coating (ARC) and Passivation Layers Using Industrial Plasma Enhanced Chemical Vapor Deposition (PECVD) for PERC Type Solar Cells', in *2018 International Conference on Photovoltaic Science and Technologies (PVCon)*, Jul. 2018, pp. 1–5. doi: 10.1109/PVCon.2018.8523918.
[41] J. Schmidt *et al.*, 'Advances in the Surface Passivation of Silicon Solar Cells', *Energy Procedia*, vol. 15, pp. 30–39, Jan. 2012, doi: 10.1016/j.egypro.2012.02.004.
[42] 'Wireless, Handheld Power Meters'. https://www.thorlabs.com (accessed Jun. 24, 2023).
[43] M. Born and E. Wolf, *Principles of Optics: Electromagnetic Theory of Propagation, Interference and Diffraction of Light*, 7th ed. Cambridge: Cambridge University Press, 1999. doi: 10.1017/CBO9781139644181.
[44] M. S. Zubairy, 'A Very Brief History of Light', in *Optics in Our Time*, M. D. Al-Amri, M. El-Gomati, and M. S. Zubairy, Eds., Cham: Springer International Publishing, 2016, pp. 3–24. doi: 10.1007/978-3-319-31903-2_1.
[45] Josell7, *English: Optical reflection: critical angle and total internal reflection*. 2012. Accessed: Nov. 30, 2022. [Online]. Available: https://commons.wikimedia.org/wiki/File:RefractionReflextion.svg
[46] 'Optics technical overview', *STEMMER IMAGING*. https://www.stemmer-imaging.com/fr-fr/donnees/optics-technical-overview/ (accessed Nov. 30, 2022).
[47] 'Optical Lens Physics'. https://www.newport.com/n/optical-lens-physics (accessed Nov. 30, 2022).
[48] R. Winston, J. C. Miñano, and P. Benítez, '1 - NONIMAGING OPTICAL SYSTEMS AND THEIR USES', in *Nonimaging Optics*, R. Winston, J. C. Miñano, and P. Benítez, Eds., Burlington: Academic Press, 2005, pp. 1–6.

doi: 10.1016/B978-012759751-5/50001-4.
[49] Jiang, Y.-F. Luo, Y.-H. Shih, Wang, Lund, and Y.-X. Zhang, 'A Review of the Compound Parabolic Concentrator (CPC) with a Tubular Absorber', *Energies*, vol. 13, p. 695, Feb. 2020, doi: 10.3390/en13030695.
[50] 'Design Guide For Compound Parabolic Concentrators', *Optiforms, Inc.* https://www.optiforms.com/compound-parabolic-concentrator-essentials/ (accessed Nov. 29, 2022).
[51] S. Querchfeld, J. Rautenberg, and K. Kampert, 'Development of a highly efficient PMT Winston-cone system for fluorescence measurement of extensive air showers', 2015. Accessed: Jun. 25, 2023. [Online]. Available: https://www.semanticscholar.org/paper/Development-of-a-highly-efficient-PMT-Winston-cone-Querchfeld-Rautenberg/c113b4e6b12727f070d7c4bc40746bdeb7a972e0
[52] K. Tanaka *et al.*, 'Compound parabolic concentrator probe for efficient light collection in spectroscopy of biological tissue', *Appl. Opt., AO*, vol. 35, no. 4, pp. 758–763, Feb. 1996, doi: 10.1364/AO.35.000758.
[53] Y. Tian, J. W. Su, J. Ju, and Q. Liu, 'Efficiency enhancement of Raman spectroscopy at long working distance by parabolic reflector', *Biomed Opt Express*, vol. 8, no. 11, pp. 5243–5252, Nov. 2017, doi: 10.1364/BOE.8.005243.
[54] R. Winston, J. C. Miñano, and P. Benítez, '5 - DEVELOPMENTS AND MODIFICATIONS OF THE COMPOUND PARABOLIC CONCENTRATOR', in *Nonimaging Optics*, R. Winston, J. C. Miñano, and P. Benítez, Eds., Burlington: Academic Press, 2005, pp. 69–98. doi: 10.1016/B978-012759751-5/50005-1.
[55] admin, 'Ray Tracing with COMSOL – First Part | Fusion of Engineering, Control, Coding, Machine Learning, and Science'. https://aleksandarhaber.com/ray-tracing-with-comsol-first-part/ (accessed Nov. 29, 2022).
[56] S. Haxha, F. AbdelMalek, F. Ouerghi, M. D. B. Charlton, A. Aggoun, and X. Fang, 'Metamaterial Superlenses Operating at Visible Wavelength for Imaging Applications', *Sci Rep*, vol. 8, no. 1, Art. no. 1, Oct. 2018, doi: 10.1038/s41598-018-33572-y.
[57] T. Trupke and R. A. Bardos, 'Self-consistent determination of the generation rate from photoconductance measurements', *Appl. Phys. Lett.*, vol. 85, no. 16, pp. 3611–3613, Oct. 2004, doi: 10.1063/1.1807961.
[58] R. A. Sinton, A. Cuevas, and M. Stuckings, 'Quasi-steady-state photoconductance, a new method for solar cell material and device characterization', in *Conference Record of the Twenty Fifth IEEE Photovoltaic Specialists Conference - 1996*, May 1996, pp. 457–460. doi: 10.1109/PVSC.1996.564042.
[59] T. Trupke *et al.*, *Progress with luminescence imaging for the*

characterisation of silicon wafers and solar cells. 2007.
[60] 'Photoluminescence Imaging for Photovoltaic Applications - ScienceDirect'. https://www.sciencedirect.com/science/article/pii/S1876610212003529 (accessed Mar. 07, 2023).
[61] J. M. Lilly and S. C. Olhede, 'Generalized Morse Wavelets as a Superfamily of Analytic Wavelets', *IEEE Transactions on Signal Processing*, vol. 60, no. 11, pp. 6036–6041, Nov. 2012, doi: 10.1109/TSP.2012.2210890.
[62] J. M. Lilly, 'Element analysis: a wavelet-based method for analysing time-localized events in noisy time series', *Proceedings of the Royal Society A: Mathematical, Physical and Engineering Sciences*, vol. 473, no. 2200, p. 20160776, Apr. 2017, doi: 10.1098/rspa.2016.0776.
[63] M. T. Caccamo and S. magazù, 'Variable length pendulum analyzed by a comparative Fourier and wavelet approach', *Revista Mexicana de Fisica E*, vol. 64, pp. 81–86, Apr. 2018, doi: 10.31349/RevMexFisE.64.81.
[64] A. Grinsted, J. C. Moore, and S. Jevrejeva, 'Application of the cross wavelet transform and wavelet coherence to geophysical time series', *Nonlinear Processes in Geophysics*, vol. 11, no. 5/6, pp. 561–566, Nov. 2004.
[65] 'Phys. Rev. E 75, 016707 (2007) - Nonstationary Gaussian processes in wavelet domain: Synthesis, estimation, and significance testing'. https://journals.aps.org/pre/abstract/10.1103/PhysRevE.75.016707 (accessed Feb. 15, 2023).
[66] 'Wavelet coherence and cross-spectrum - MATLAB wcoherence - MathWorks United Kingdom'. https://uk.mathworks.com/help/wavelet/ref/wcoherence.html?s_tid=doc_ta (accessed Feb. 15, 2023).
[67] A. Desthieux *et al.*, 'Detection of stable positive fixed charges in AlOx activated during annealing with in situ modulated PhotoLuminescence', *Solar Energy Materials and Solar Cells*, vol. 230, p. 111172, Sep. 2021, doi: 10.1016/j.solmat.2021.111172.
[68] B. Bérenguier, N. Moron, W. Zhao, J. F. Guillemoles, J.-P. Kleider, and L. Lombez, 'High-Frequency Modulated Photoluminescence: a simulation study of cases describing the signature of carrier recombination and trap centers', in *2019 IEEE 46th Photovoltaic Specialists Conference (PVSC)*, Jun. 2019, pp. 0352–0358. doi: 10.1109/PVSC40753.2019.8980539.
[69] N. Moron, B. Bérenguier, J. Alvarez, and J.-P. Kleider, 'Analytical model of the modulated photoluminescence in semiconductor materials', *J. Phys. D: Appl. Phys.*, vol. 55, no. 10, p. 105103, Dec. 2021, doi: 10.1088/1361-6463/ac39c4.
[70] W. Zhao *et al.*, 'Coupled time resolved and high frequency modulated photoluminescence probing surface passivation of highly doped n-type InP samples', *Journal of Applied Physics*, vol. 129, no. 21, p. 215305, Jun.

2021, doi: 10.1063/5.0033122.
[71] R. Brüggemann and S. Reynolds, 'Modulated photoluminescence studies for lifetime determination in amorphous-silicon passivated crystalline-silicon wafers', *Journal of Non-Crystalline Solids*, vol. 352, no. 9, pp. 1888–1891, Jun. 2006, doi: 10.1016/j.jnoncrysol.2005.11.092.
[72] 'Quantitative Recombination and Transport Properties in Silicon from Dynamic Luminescence | SpringerLink'. https://link.springer.com/book/10.1007/978-3-319-06157-3 (accessed Feb. 16, 2023).
[73] A. Desthieux, 'Development and characterization of Fired Passivating Contacts for p-type silicon solar cells fabrication', These de doctorat, Institut polytechnique de Paris, 2021. Accessed: Feb. 15, 2023. [Online]. Available: https://www.theses.fr/2021IPPAX091
[74] R. Brendel, 'Note on the interpretation of injection-level-dependent surface recombination velocities', *Appl. Phys. A*, vol. 60, no. 5, pp. 523–524, May 1995, doi: 10.1007/BF01538780.
[75] J. Schmidt, 'Measurement of differential and actual recombination parameters on crystalline silicon wafers [solar cells]', *IEEE Transactions on Electron Devices*, vol. 46, no. 10, pp. 2018–2025, Oct. 1999, doi: 10.1109/16.791991.
[76] J. A. Giesecke, S. W. Glunz, and W. Warta, 'Determination of Actual Carrier Lifetime from Differential Measurements', *Energy Procedia*, vol. 38, pp. 59–65, Jan. 2013, doi: 10.1016/j.egypro.2013.07.249.
[77] 'Radio Frequency Modulation Made Easy', *springerprofessional.de*. https://www.springerprofessional.de/en/radio-frequency-modulation-made-easy/10531386 (accessed Feb. 15, 2023).
[78] W. Li *et al.*, 'A fast measurement of Warburg-like impedance spectra with Morlet wavelet transform for electrochemical energy devices', *Electrochimica Acta*, vol. 322, p. 134760, Nov. 2019, doi: 10.1016/j.electacta.2019.134760.
[79] 'Zero: The Biography of a Dangerous Idea'. https://www.goodreads.com/book/show/329336.Zero (accessed Feb. 27, 2023).
[80] 'Ultralow surface recombination of c-Si substrates passivated by plasma-assisted atomic layer deposited Al2O3: Applied Physics Letters: Vol 89, No 4'. https://aip.scitation.org/doi/10.1063/1.2240736 (accessed Feb. 20, 2023).
[81] Md. A. Hossain *et al.*, 'Atomic layer deposition enabling higher efficiency solar cells: A review', *Nano Materials Science*, vol. 2, no. 3, pp. 204–226, Sep. 2020, doi: 10.1016/j.nanoms.2019.10.001.
[82] R. Hezel and K. Jaeger, 'Low-Temperature Surface Passivation of Silicon for Solar Cells', *J. Electrochem. Soc.*, vol. 136, no. 2, p. 518, Feb. 1989, doi:

10.1149/1.2096673.
[83] D. Lei, X. Yu, L. Song, X. Gu, G. Li, and D. Yang, 'Modulation of atomic-layer-deposited Al2O3 film passivation of silicon surface by rapid thermal processing', *Appl. Phys. Lett.*, vol. 99, no. 5, p. 052103, Aug. 2011, doi: 10.1063/1.3616145.
[84] G. Dingemans, R. Seguin, P. Engelhart, M. C. M. van de Sanden, and W. M. M. Kessels, 'Silicon surface passivation by ultrathin Al2O3 films synthesized by thermal and plasma atomic layer deposition', *physica status solidi (RRL) – Rapid Research Letters*, vol. 4, no. 1–2, pp. 10–12, 2010, doi: 10.1002/pssr.200903334.
[85] F. Benner, P. Jordan, M. Knaut, I. Dirnstorfer, J. Bartha, and T. Mikolajick, *Investigation of the c-Si/Al2O3 Interface for Silicon Surface Passivation*. 2012. doi: 10.4229/27thEUPVSEC2012-2CV.5.57.
[86] 'Coordination and interface analysis of atomic-layer-deposition Al2O3 on Si(001) using energy-loss near-edge structures: Applied Physics Letters: Vol 83, No 21'. https://aip.scitation.org/doi/abs/10.1063/1.1629397 (accessed Feb. 27, 2023).
[87] B. Hoex, J. J. H. Gielis, M. C. M. van de Sanden, and W. M. M. Kessels, 'On the c-Si surface passivation mechanism by the negative-charge-dielectric Al2O3', *Journal of Applied Physics*, vol. 104, no. 11, p. 113703, Dec. 2008, doi: 10.1063/1.3021091.
[88] J. Robertson, 'Interfaces and defects of high-K oxides on silicon', *Solid-State Electronics*, vol. 49, no. 3, pp. 283–293, Mar. 2005, doi: 10.1016/j.sse.2004.11.011.
[89] M. Choi, A. Janotti, and C. G. Van de Walle, 'Native point defects and dangling bonds in α-Al2O3', *Journal of Applied Physics*, vol. 113, no. 4, p. 044501, Jan. 2013, doi: 10.1063/1.4784114.
[90] K. Matsunaga, T. Tanaka, T. Yamamoto, and Y. Ikuhara, 'First-principles calculations of intrinsic defects in ${\mathrm{Al}}_{2}{\mathrm{O}}_{3}$', *Phys. Rev. B*, vol. 68, no. 8, p. 085110, Aug. 2003, doi: 10.1103/PhysRevB.68.085110.
[91] J. J. H. Gielis, B. Hoex, M. C. M. van de Sanden, and W. M. M. Kessels, 'Negative charge and charging dynamics in Al2O3 films on Si characterized by second-harmonic generation', *Journal of Applied Physics*, vol. 104, no. 7, p. 073701, Oct. 2008, doi: 10.1063/1.2985906.
[92] D. Suh and W. S. Liang, 'Electrical properties of atomic layer deposited Al2O3 with anneal temperature for surface passivation', *Thin Solid Films*, vol. 539, pp. 309–316, Jul. 2013, doi: 10.1016/j.tsf.2013.05.082.
[93] A. Cuevas *et al.*, 'Carrier population control and surface passivation in solar cells', *Solar Energy Materials and Solar Cells*, vol. 184, pp. 38–47, Sep. 2018, doi: 10.1016/j.solmat.2018.04.026.
[94] C. Guerra-Nuñez, M. Döbeli, J. Michler, and I. Utke, 'Reaction and Growth

Mechanisms in Al2O3 deposited via Atomic Layer Deposition: Elucidating the Hydrogen Source', *Chem. Mater.*, vol. 29, no. 20, pp. 8690–8703, Oct. 2017, doi: 10.1021/acs.chemmater.7b02759.

[95] G. Dingemans, M. C. M. van de Sanden, and W. M. M. Kessels, 'Influence of the Deposition Temperature on the c-Si Surface Passivation by Al2O3 Films Synthesized by ALD and PECVD', *Electrochem. Solid-State Lett.*, vol. 13, no. 3, p. H76, Dec. 2009, doi: 10.1149/1.3276040.

[96] G. Dingemans and W. M. M. Kessels, 'Status and Prospects of Al2O3-Based Surface Passivation Schemes for Silicon Solar Cells', *Journal of Vacuum Science & Technology A: Vacuum, Surfaces, and Films*, vol. 30, pp. 040802–040802, Jul. 2012, doi: 10.1116/1.4728205.

[97] M. Pawlik *et al.*, 'Electrical and Chemical Studies on Al2O3 Passivation Activation Process', *Energy Procedia*, vol. 60, Dec. 2014, doi: 10.1016/j.egypro.2014.12.347.

[98] K. Huet, 'Chapter 4 - Laser annealing applications for semiconductor devices manufacturing', in *Laser Annealing Processes in Semiconductor Technology*, F. Cristiano and A. La Magna, Eds., in Woodhead Publishing Series in Electronic and Optical Materials. Woodhead Publishing, 2021, pp. 137–173. doi: 10.1016/B978-0-12-820255-5.00008-8.

[99] Y.-C. Huang and R. W. Chuang, 'Study on Annealing Process of Aluminum Oxide Passivation Layer for PERC Solar Cells', *Coatings*, vol. 11, no. 9, Art. no. 9, Sep. 2021, doi: 10.3390/coatings11091052.

[100] S. N. Abolmasov and P. R. i Cabarrocas, 'In situ photoluminescence system for studying surface passivation in silicon heterojunction solar cells', *Journal of Vacuum Science & Technology A*, vol. 33, no. 2, p. 021201, Mar. 2015, doi: 10.1116/1.4902014.

[101] 'In situ monitoring of Raman scattering and photoluminescence from silicon surfaces in HF aqueous solutions: Applied Physics Letters: Vol 72, No 8'. https://aip.scitation.org/doi/abs/10.1063/1.120877?casa_token=BDPoKkiXXK0AAAAA:Z7wKzM7QQwbKGeRJml4Gwh6TvSPPr3W5i8y81c4CFikDhfmQmzAfCKVLYsgsrqXyUw5Jwi4Jv_I (accessed Mar. 16, 2023).

[102] J. C. Sturm and C. M. Reaves, 'Silicon temperature measurement by infrared absorption. Fundamental processes and doping effects', *IEEE Transactions on Electron Devices*, vol. 39, no. 1, pp. 81–88, Jan. 1992, doi: 10.1109/16.108215.

[103] 'Stability of Al2O3 and Al2O3/a-SiNx:H stacks for surface passivation of crystalline silicon: Journal of Applied Physics: Vol 106, No 11'. https://aip.scitation.org/doi/10.1063/1.3264572 (accessed Mar. 01, 2023).

[104] J. J. H. Gielis, B. Hoex, M. C. M. van de Sanden, and W. M. M. Kessels, 'Negative charge and charging dynamics in Al2O3 films on Si

characterized by second-harmonic generation', *Journal of Applied Physics*, vol. 104, no. 7, p. 073701, Oct. 2008, doi: 10.1063/1.2985906.
[105] W. Wang *et al.*, 'Coupled Electron-Hole Dynamics at the Si / SiO 2 Interface', *Physical Review Letters*, vol. 81, Nov. 1998, doi: 10.1103/PhysRevLett.81.4224.
[106] A. Descoeudres *et al.*, 'Improved amorphous/crystalline silicon interface passivation by hydrogen plasma treatment', *Appl. Phys. Lett.*, vol. 99, no. 12, p. 123506, Sep. 2011, doi: 10.1063/1.3641899.
[107] I. Martín *et al.*, 'Improvement of crystalline silicon surface passivation by hydrogen plasma treatment', *Appl. Phys. Lett.*, vol. 84, no. 9, pp. 1474–1476, Mar. 2004, doi: 10.1063/1.1647702.
[108] G. Dingemans, F. Einsele, W. Beyer, M. C. M. van de Sanden, and W. M. M. Kessels, 'Influence of annealing and Al2O3 properties on the hydrogen-induced passivation of the Si/SiO2 interface', *Journal of Applied Physics*, vol. 111, no. 9, p. 093713, May 2012, doi: 10.1063/1.4709729.
[109] A. Howling *et al.*, Eds., 'Mechanism of substrate charging after plasma processing', *Proc. 15th International Symposium on Plasma Chemistry*, 2001.
[110] C. Herring, N. M. Johnson, and C. G. Van de Walle, 'Energy levels of isolated interstitial hydrogen in silicon', *Phys. Rev. B*, vol. 64, no. 12, p. 125209, Sep. 2001, doi: 10.1103/PhysRevB.64.125209.
[111] S. Estreicher, 'Equilibrium sites and electronic structure of interstitial hydrogen in Si', *Phys. Rev. B*, vol. 36, no. 17, pp. 9122–9128, Dec. 1987, doi: 10.1103/PhysRevB.36.9122.

Titre : Développement d'un dispositif de mesure in-situ de la durée de vie effective des électrons

Mots clés : Lifetime, Electron, Photon, Silicon, AlOx

Résumé :

Au fur et à mesure que la technologie progresse à travers les niveaux de maturité technologique (TRL), elle passe des concepts théoriques et de la recherche fondamentale à des applications pratiques et à des prototypes raffinés. Les mesures in situ de la durée de vie fournissent des informations précieuses sur la qualité du processus de fabrication des semi-conducteurs, permettant une surveillance et une analyse en temps réel des processus dynamiques. En analysant les durées de vie des porteurs minoritaires, les chercheurs peuvent évaluer l'efficacité de diverses techniques de passivation et de traitements de surface visant à réduire les pertes par recombinaison et à améliorer l'efficacité des dispositifs de cellules solaires. Cette thèse porte sur le développement du matériel, de la théorie et l'application expérimentale d'un dispositif de mesure in-situ de la durée de vie des porteurs minoritaires (durée de vie in-situ). Cela a impliqué l'inclusion d'optiques sans imagerie et la mise en forme du faisceau facilitant l'installation du dispositif. En outre, la diminution du temps de mesure facilite la détection des changements rapides qui peuvent être essentiels à la compréhension des systèmes complexes, tandis que le passage d'une technique de mesure indirecte à une technique de mesure directe pour la mesure de la durée de vie à l'aide d'une gaussienne pourrait ouvrir de nouvelles voies.

Ces dernières années, l'oxyde d'aluminium amorphe (AlO_x) a fait l'objet d'une attention particulière en tant que matériau important pour la passivation des surfaces des cellules solaires au silicium cristallin. En utilisant le dispositif mis au point, les possibilités d'utilisation d'un réacteur PECVD ont été mises en évidence, notamment l'optimisation du processus de fabrication par des procédures de recuit et l'analyse des propriétés du matériau de base.

Title : Development and application of an in-situ effective electron lifetime measurement device

Keywords : Lifetime, Electron, Photon, Silicon, AlO_x

Abstract :

As technology progresses through Technology Readiness Levels (TRLs), it moves from theoretical concepts and basic research, towards practical applications and refined prototypes. In-situ lifetime measurements, provide valuable insights into the quality of the semiconductor fabrication process, enabling real-time monitoring and analysis of dynamic processes. By analysing minority carrier lifetimes, researchers can assess the effectiveness of various passivation techniques and surface treatments aimed at reducing recombination losses and enhancing the efficiencies of solar cell devices. This thesis focuses on the development of hardware, theory, and experimental application of an in-situ minority carrier lifetime measurement (in-situ lifetime) device. This involved the inclusion of non-imaging optics and beam shaping for a design which has an ease of installation. Moreover, decreasing measurement time facilitates the detection of rapid changes that may be critical to understanding complex systems while switching from indirect to direct measurement technique for a lifetime measurement using a Gaussian could open new avenues

Amorphous Aluminium oxide (AlO_x) has gained significant attention as an important material in surface passivation for crystalline silicon solar cells in recent years. Utilizing the developed device, potential avenues using a PECVD reactor were highlighted such as optimizing the fabrication process through annealing procedures, and analysis base material properties.